1972

Deformation and fracture of concrete under uniaxial impact loading

Esteban Eulogio Miranda

DEFORMATION AND FRACTURE OF CONCRETE UNDER UNIAXIAL IMPACT LOADING

by

ESTEBAN EULOGIO MIRANDA, 1939-

A DISSERTATION

Presented to the Faculty of the Graduate School of the

UNIVERSITY OF MISSOURI-ROLLA

In Partial Fulfillment of the Requirements for the Degree

DOCTOR OF PHILOSOPHY

in

MINING ENGINEERING

1972

Charles J. Haas
Advisor

Ronald R. Bellinis

Leroy B. Clark

J. Earl Foster

H. P. Pyron

Everett M. Shoham

ABSTRACT

Stress wave propagation and interaction in plain concrete leading up to spall fracture was investigated experimentally with a computer numerical analysis of the bar-geometry axial-impact loading. The critical normal fracture strain energy U and mechanical energy W criteria are proposed for the spatial and time dependence explanation of spallation in concrete. The energy criteria are special cases of a more generalized cumulative damage model of the form:

$$\int_0^{Z_F} f[\sigma(Z)]dZ = 1$$

where Z is the space or time coordinate, Z_F is the value of Z at fracture initiation, and $f[\sigma(Z)]$ is a second order stress damage function in terms of the physical material properties (E and c), cross-sectional area A, and the constant energy transferred or stored (W or U).

Finite-difference analyses of the wave propagation and interactions in the split Hopkinson bar showed that early failure in brittle materials limits the application of the conventional method of analysis because equilibrium in the specimen is not reached before failure. The dynamic stress-strain-strain rate curves indicate that the failure strain is more a function of strain rate than is the ultimate stress, the latter case being observed by other investigators. Dynamic unloading stress-strain curves in the post-failure region are shown to be generally similar to those obtained by servo-controlled testing machines at lower strain rates.

ACKNOWLEDGMENTS

The author wishes to express his thanks to Dr. Charles J. Haas for his valued advice and continued encouragement in the work leading to this dissertation, and also for his assistance in the final wording of the text.

Sincere appreciation and gratitude is extended to Dr. George B. Clark, Director of the Rock Mechanics and Explosives Research Center, for his wisdom, partial financial support through research appointments, and for providing the equipment and the facilities for the investigation. Partial financial support was provided by the U. S. Department of Defense, THEMIS Contract No. DACA-45-69-C-0087.

He is also grateful to Mr. Robert Allen, student assistant, who helped with the experimental work and to Mrs. Brenda Watson and Mrs. Kathie Prewitt for their efforts typing the manuscript.

He is much indebted to the State Technical University of Chile for the invaluable training and financial support received.

Finally, great appreciation is extended to the author's wife, Nancy, whose, love, partnership, patience, tolerance, and spiritual strength always overwhelmed the difficulties associated with four years of graduate study. To his sweet children, Veronica, Fernando, and Eduardo, who gave many happy and enjoyable hours, the author is gratefully indebted.

TABLE OF CONTENTS

LIST OF FIGURES

Figure Page

Figure

Page

Figure Page

LIST OF TABLES

LIST OF SYMBOLS

Symbols commonly used throughout text are:

A cross-sectional area of long bar

A_I, A_s, A_T cross-sectional areas of incident bar, specimen, and transmission bar, respectively

c propagation velocity of longitudinal waves in a bar ($c = \sqrt{E/\rho}$)

c_I, c_s, c_T propagation velocities of bar wave in incident bar, specimen, and transmission bar, respectively

d_L, d_T distances from incident and transmission bar gages to specimen-bar interfaces, respectively

E Young's modulus

E_I, E_s, E_T Young's moduli for incident bar, specimen, and transmission bar, respectively

E_d dynamic compressive Young's modulus of long bars

$f[\sigma(Z)]$ stress damage function in cumulative damage model

i integer denoting space columns in finite-difference rectangular grid

j integer denoting time rows in finite-difference rectangular grid

K_u constant in long bar experiments ($K_u = \frac{2EU}{A}$)

K_w constant in long bar experiments ($K_w = \frac{EW}{Ac}$)

L_s specimen length

P_c peak compressive stress

S_c dynamic compressive strength in concrete bars

S_T dynamic tensile strength

t time

t_0 time at which spall plane first experiences a tensile stress

t_s time at which spall fracture initiates

$t_s - t_0$ tensile rise time to fracture initiation ($t_s - t_0 = \Delta t$)

U strain energy stored in tensile-stressed portion of long bar between impact end and spall at the time of fracture initiation

u axial particle displacement

v longitudinal particle velocity

V_{spall} instantaneous net particle velocity at spall plane

W mechanical energy passing through spall plane up to time of fracture initiation

x axial coordinate

x_0 location of zero tensile stress in the stress distribution along bar

x_s location of spall plane

$x_s - x_0$ tensile-stressed region near impact end of long bar

Z space or time coordinate in cumulative damage model

Z_F value of Z at fracture initiation

α wave interaction factor (ratio of apparent time to true time)

β_u nonlinearity factor [$\beta_u = K_u/(\sigma_s{}^2 \Delta x/3)$]

β_w nonlinearity factor [$\beta_w = K_w/(\sigma_s{}^2 \Delta t/3)$]

Δt true duration of tensile stress at spall plane ($\Delta t = t_s - t_0$)

Δx $x_s - x_0$

Δx_I mesh size for incident and transmission bars

Δx_s mesh size for split-bar specimen

$\Delta\sigma$ stress difference

$\frac{\Delta\sigma}{\Delta x}$ derived tensile stress gradient ($\frac{\Delta\sigma}{\Delta x} = \sigma_s/\Delta x$)

$\Delta\tau$ apparent duration of tensile stress at spall plane ($\Delta\tau = \Delta x/c$)

ε axial strain

ε_{avg} average strain in the split-bar specimen

$\varepsilon_I, \varepsilon_R, \varepsilon_T$ incident, reflected, and transmitted strains, respectively

ε_s spall strain at fracture initiation

$\dot{\varepsilon}$ strain rate

$\dot{\varepsilon}_a$ apparent strain rate ($\dot{\varepsilon}_a=\varepsilon_s/\Delta x/c$)

$\dot{\varepsilon}_{avg}$ average strain rate in the split-bar specimen

$\dot{\varepsilon}_s$ instantaneous strain rate at fracture initiation

$\dot{\varepsilon}_{sd}$ derived strain rate ($\dot{\varepsilon}_{sd}=\varepsilon_s/\Delta t$)

ρ mass density

ρ_I,ρ_s,ρ_T mass densities of incident bar, specimen, and transmission bar, respectively

σ axial stress

σ_{avg} average stress in split-bar specimen

$\sigma_{bar}(x)$ net tensile stress distribution along bar at time of fracture initiation

$\sigma_I,\sigma_R,\sigma_T$ incident, reflected, and transmitted stresses, respectively

$\sigma_{i,j}$ stress at the (i,j)th mesh point

σ_s instantaneous critical spall stress [$\sigma_s=\sigma_{bar}(x_s)=\sigma_{spall}(t_s)$]

$\sigma_{spall}(t)$ instantaneous net tensile stress at spall plane

$\dot{\sigma}_a$ apparent stress rate ($\dot{\sigma}_a=E\dot{\varepsilon}_a$)

τ,τ' wave travel times in the split-bar specimen

Compression stresses and strains are reckoned positive.

I. INTRODUCTION AND LITERATURE REVIEW

A. INTRODUCTION

Dynamic stresses of high magnitude arise in a number of mining, construction and military activities. The propagation of such stress waves through rock masses and their interactions with surface and underground structures are complex phenomena for which present predictive capabilities are generally only first approximations. Such situations also arise in connection with explosive blasting, rockbursts, percussive drilling in mining, earthquakes, comminution, hypervelocity impact, and explosions. Wave effects must be considered in many stages of the design when rock structures are located in seismically active areas. In the understanding and prediction of the response of rock to dynamic loading, the deformation behavior and fracture are of the most interest to the practicing engineers.

Fracture in rock under high rate tensile and compressive loading conditions is more complex and considerably less well understood than fracture under quasi-static conditions. At present there is no accurate theoretical basis for predicting dynamic failure although the usefulness of such a basis would be great.

Spalling, or scabbing, is the dynamic fracture of a material that is subjected to a tensile wave loading. It is also referred to as Hopkinson fracture in honor of the pioneer in this field, Hopkinson (1912). The section of the material that separates from the main body is referred to as spall or scab. Spalling may occur whenever an impact or force of an explosion acts on a solid having a free surface at which reflection can occur.

The hazard of spalling is an important consideration when rock faces are subjected to dynamic loading. In particular, spalling can be a controlling factor in the design of underground and surface excavations. In fortifications, for instance, a bomb may impinge on one surface of a wall and without penetrating produce a spall at the opposite surface. This spall may fly off with considerable velocity and endanger personnel inside. Similar loadings may be produced by blasting or rockbursts too near a permanent mine opening. On the other hand spalling is a desirable phenomenon as in the breaking of rock by explosives in the mining industry.

The deformation, failure, and post-failure behavior of rock under high rate compression loading conditions are of concern to engineers in the design of structure on or within a rock mass where safety, usability and economy are design parameters. If the nature of the dynamic loads on the structure are known and if the material characteristic of the component materials are known then the questions relating to its safety and usability can be answered, that is, providing the necessary computational techniques are available.

The deformation behavior and strength of many materials depend on the dynamic-wave propagation properties of the material and they may be influenced significantly by the rate of loading or straining. Therefore, the application of static properties to dynamic phenomena may give grossly inaccurate predictions of the response, particularly for those materials exhibiting strong rate effects.

A study of the post-failure process in rock may help in the investigations of rockbursts in deep underground mines. Field investigations have shown that destressing by partially fracturing the rock by blasting can be used to prevent the explosive failure of rock structures.

B. REVIEW OF LITERATURE

Since the first reported observations of spallation by Hopkinson (1912), the contributions to the field have consisted, for the most part, of the measurement of the stress necessary to produce spalls in metals. These measurements are generally not in agreement because of appreciable variation in the analyses used to determine the stress as well as in the experimental procedures employed. It must be realized that, even though a spall occurs in but a few microseconds, the sequence of events leading to spall is orderly. The sequence is initiated by subjecting the material to a compressive stress wave usually induced by explosive loading or by projectile impact. The stress waves and their subsequent interactions with material boundaries and with one another ultimately, under proper conditions, produce a tension wave. The stress waves influence the microstructure of the material and thereby condition the material. It follows that if a complete description of spall fracture is to be compiled each event in the sequence and the response of the material to these events must be considered. The description of spallation in rock and metals is far from complete. However advances made in the disciplines which parallel the study of spall fracture, such as dislocation theory, crack propagation, and stress wave analysis, have permitted some insight into the mechanism of spallation.

In a recent research Shockey, et al., (1972), based on fractographic observations of novaculite rock specimens, proposed for the fracture of rock under high rate tensile loading the following fracture spall mechanism. A number of pre-existing flaws in the rock sample are activated when a high rate tensile load is applied. The activated flaws

propagate rapidly as radially expanding brittle cracks during the loading phases and soon begin to join up with and run into one another. In advanced stages of crack coalescence a myriad of continuous fracture surfaces will be produced throughout the rock sample, isolating segments of unfractured rock. The individual segments no longer held in the aggregate of the rock sample separate from each other, reducing the sample to fragments.

The failure of rock is therefore a function of the number of flaws that become running cracks, the distance that each crack propagates, the degree to which coalescence and branching occurs, the initial defect structure in the rock, the inherent fracture resistance of crack-free material, and the applied stress history. Eventually it is hoped that the above quantities will be related to each other in a dynamic fracture computational model. Ideally, the model would give a complete description of the dynamic response of rocks and rock-like materials to a stress pulse in various structural and stratigraphic configurations.

Sophisticated computer codes to predict resultant fragment size distributions in material undergoing dynamic fracture will be needed. Crack acceleration, crack opening, stress histories, and spall criteria are among the features to be included in such codes.

The literature on dynamic rock fracture is generally not concerned with the microscopic mechanism of deformation and fracture but rather with empirical criteria obtained from experimental observations. Hino (1966) pointed out that in the mechanics of spallation the tensile strength of the material will control the length of the spalls. Certainly, as slabbing in rock is a tensile failure information on the dynamic

tensile strength would be useful for the design of blasting geometries.

Rinehart (1960) introduced the critical normal fracture stress as the minimum dynamic net tensional stress required to rupture the material. It has usually been assumed to be a constant value for a given material. While this assumption is convenient to apply, there is evidence which indicates that this critical strength value is not constant but instead is some function of the state of stress (static and dynamic) and strain rate that exist in the region of the fracture up to and at the time of its formation.

Bacon (1962), Rinehart (1964), (1965), and Millinger and Birkimer (1966) have published data on the comparative static and dynamic strengths of rock and concretes. These data indicate that the dynamic tensile strengths of certain rocks and concrete are substantially higher than their corresponding static strengths. Therefore, static tensile strengths may be poor approximations for dynamic applications.

Saluja (1967) demonstrated that in one-dimensional bars the first spall was the thickest, and the thickness of subsequent spalls was smaller. He further pointed out that the size of the different spalls depended on the dynamic tensile strength of the rock and the stress history.

Birkimer (1970) presented the critical normal tensile fracture strain energy theory and suggested its potential for some rocks. He also stated that the dynamic tensile strength of a rock and concrete is not constant and varies with apparent straining rate.

A number of investigators (Kumar, 1968; Stowe and Ainsworth, 1968; Green and Perkins, 1968; Wuerker, 1959; Atchley and Furr, 1967; Watstein, 1953; among others) have reported that compressive strength and modulus

of elasticity of rock and rock-like materials increases with increasing rates of loading. They have used different techniques for studying the dynamic response of rock. Some are based on rigid mechanical considerations and do not consider wave propagation and interaction aspects at high loading rates.

Data on the effect of high strain rates on the deformation behavior and compressive strength of rock and rock-like materials is relatively sparse and incomplete. The main reason is that difficulties are encountered in both instrumentation and analysis when stress wave propagation experiments are used for brittle materials. This is also complicated by the statistical nature of rock properties.

Watstein (1953) has investigated the effect of the rate of application of load on the compressive strength and modulus of elasticity of two concretes having compressive strengths of approximately 2500 and 6500 psi. The concrete was tested at strain rates ranging from 10^{-6} to about 10 per second. The higher rates of loading were obtained by impacting the concrete specimens with a drop hammer. He found that the compressive strength of each concrete increased with the rate of loading with the maximum ratio of dynamic to static compressive strengths being about 1.8 for the highest strain rate, 10 per second. The values of the secant moduli of elasticity increased significantly with the rate of application of load; the maximum ratio of dynamic to static modulus was 1.47 and 1.33 for weak and strong concrete, respectively. He also pointed out that values of strain at failure for the highest rates of loading were materially greater than the corresponding values in the static tests. The work by Atchley and Furr (1967) showed that when

moderate strength concrete is stressed with increased loading rates, the longitudinal strain at fracture is increased.

Attewell (1962), Kumar (1968), Green and Perkins (1968), Hakalehto (1969) and, Wu and Hustrulid (1971) have reported very high strain rate experiments on rocks by using the split Hopkinson pressure bar technique.

C. SUBJECT OF THESIS

This dissertation considers wave propagation and spall fragmentation in terms of the governing factors: material compressive and tensile strength, dynamic stress-strain relationship, shape of incident pulse, and resultant stress history. Thus, the objective of this research is to increase the understanding of dynamic rock failure towards the development of a criterion for spallation in rock and rock-like materials. This is accomplished with experiments and analysis involving simple bar-geometry axial-impact loading and computer numerical analysis. This information is necessary for a computational model to predict failure under high rate tensile loading.

The theoretical analyses in the tests described above are quite different because the properties of the materials were unknown at very high rates of loading and also, because rigorous mathematical solutions for most pulse shapes were not available.

To complement the spallation study an attempt is made to analyze the compressional split Hopkinson bar high strain rate technique for brittle rock testing. Both conventional and wave propagation methods are analyzed and data on the dynamic compressive deformation and post failure of the concrete is presented.

II. LONG BAR IMPACT EXPERIMENTS

A. INTRODUCTION

A one dimensional finite difference computer code to simulate plane, longitudinal stress wave propagation, and interaction in the spallation of long bars was written for elastic materials (See Appendix A). This approach was attempted as a first step in studying the structural response of rock and rock-like materials; and could be modified to incorporate strain-rate dependence if it were found to be a significant factor in the real material constitutive equation.

With the elastic constitutive equation of state governing the dynamic loading and unloading, the complete stress history at the spall plane and the stress state at the time of fracture were determined. This information was necessary to determine the criteria for fracture. Thus, a phenomenological approach was developed to obtain information on the wave propagation and interaction, and on improving spallation criteria. The method involves theoretical fitting of experimental results to determine the governing parameters.

B. SPECIMEN FABRICATION

To conduct the wave propagation and dynamic fracture studies, it was necessary to develop a fabrication capability for long bar concrete specimens. Cylindrical bar specimens were cast having a diameter of approximately 1.5 inches and a length of approximately 28 inches. The mix was a plain Portland cement concrete with proportions shown in Table I.

TABLE I - MIX PROPORTIONS

Material	% by Weight
Type III Portland Cement, C	24.26
Fine sand - dry , S	60.02
Water , W	15.72
TOTAL	100.00

W/C (by weight) = 0.6479

S/C (by weight) = 2.4744

Atlas, high-early strength, Type III Portland Cement was used as the cementing agent. The high-early strength variety was chosen so that long curing time would not be required. Type III attains a strength in 8 days roughly equivalent to the 28 day strength of standard cement (Type I). The fine aggregate was a screened product from the St. Peters sandstone at Pacific, Missouri and produced by Pioneer Silica Products Company. The sand is designated as fine grade and is classed as sub-angular.

A batch of concrete was mixed in sufficient quantity to manufacture four bar specimens. The concrete specimens were cast in Plexiglas cylindrical casting tubes (1.5 in. I.D. by 28 in. long and slit along one side) by means of an extended funnel. The funnel tube extended to the bottom of the casting tubes and was attached at its upper end to a heavy vibrator to minimize air entrapment and surface honeycombs in the specimens. The cylindrical casting tubes were moved vertically downward by a hand hoist during the casting process so that the previously cast mix was not vibrated excessively. The insides of the molds were

coated with oil to prevent the concrete from sticking. After casting, the cylinders were held in vertical position for one day. The bars were then removed from the molds and immersed in limed water for six days in a horizontal position. The rods were then removed from the water and cured at room temperature conditions for eight days until testing on the fifteenth day. Before testing, the ends were cut and ground plane and perpendicular to the axis of the rod so that the actual test specimens measured 1.5 in. x 24 in.

Every possible effort was made to obtain identical compositions, uniformity of fabrication and processing of the specimens in order to secure maximum reproducibility of the test results. A summary of the average mechanical properties of the concrete specimens at room temperature, are given in Table II.

TABLE II - AVERAGE MECHANICAL PROPERTIES OF PORTLAND CEMENT CONCRETE

Curing conditions -

In casting tubes	1 day
Submersed in water	6 days
Room temperature drying	8 days
Total curing	15 days

Average Physical properties of test specimens* -

Static uniaxial compressive strength, psi	(22)	4805 ± 500
Static uniaxial direct tensile strength**, psi	(2)	388 ± 18
Static compressive Young's modulus, psi x 10^6	(6)	2.37 ± 0.03
Static tensile Young's modulus, psi x 10^6	(1)	2.72
Poisson's ratio in compression	(5)	0.14 ± 0.03
Poisson's ratio in tension	(1)	0.15

TABLE II - AVERAGE MECHANICAL PROPERTIES OF PORTLAND CEMENT CONCRETE

CONTINUED

Specific weight, lb./in.^{3} x 10^{-4}	(21)	723 ± 15
Mass density, lb.-sec.^{2}/in.^{4} x 10^{-5}	(21)	18.71 ± 0.38
Ultrasonic pulse velocity, in./sec. x 10^5	(5)	1.30 ± 0.03
Bar wave velocity†, in./sec. x 10^5	(10)	1.31 ± 0.02
Bar velocity††, in./sec. x 10^5	(1)	1.31
Fundamental frequency (24 in. bar length) H_z	(1)	2730
Dynamic Young's modulus†, psi x 10^6	(10)	3.21 ± 0.10

* The number appearing in parenthesis denotes the number of specimens tested

** Fracture is near a glued specimen end

† Values calculated from long bar spallation data

†† Value determined from resonant frequency test

C. EQUIPMENT, INSTRUMENTATION, AND EXPERIMENTAL PROCEDURE

The long bar specimens were instrumented using Micro-Measurements ED-DY-250-BG -350 foil-type resistance strain gages attached with Baldwin Lima Hamilton EPY-150 epoxy cement. The 0.250 in. gage length insured that strain gradients and statistical material variation would not present difficulties in interpreting the gage readings.

The gages were mounted in pairs diametrically opposed at two gaging stations and positioned along the same two generators of the bar. At each station the strain gages were connected into opposite arms of a Wheastone-bridge circuit so that any bending strains would be cancelled out. The current through the gages was limited to 15 milliamps in order to minimize heating in the vicinity of the gage. The Wheastone-bridge circuit was connected to a strain gage conditioning unit which provided the desired DC supply voltage, balancing circuit, and shunt calibration network.

The strain signals from the gages were displayed versus time on the screen of a Tektronix Type 549 storage oscilloscope with a Type 1A1 dual trace plug in unit. The stored displays were then photographed with a Polaroid oscilloscope camera. A trigger pulse was provided to the oscilloscopes when the projectile made electrical contact with a small wire attached to the input end of the specimen. The delayed trigger feature on the oscilloscope was used so that optimum time resolution of the strain gage signal could be achieved.

Stress waves were initiated in the rods by impact with spherical-nosed (3/4 in. radius) cylindrical aluminum striker bars of various lengths (4, 6, and 8 in.) and 1.497 inches in diameter propelled by the air gun shown in Figure 2.1. The experimental setup is similar to the

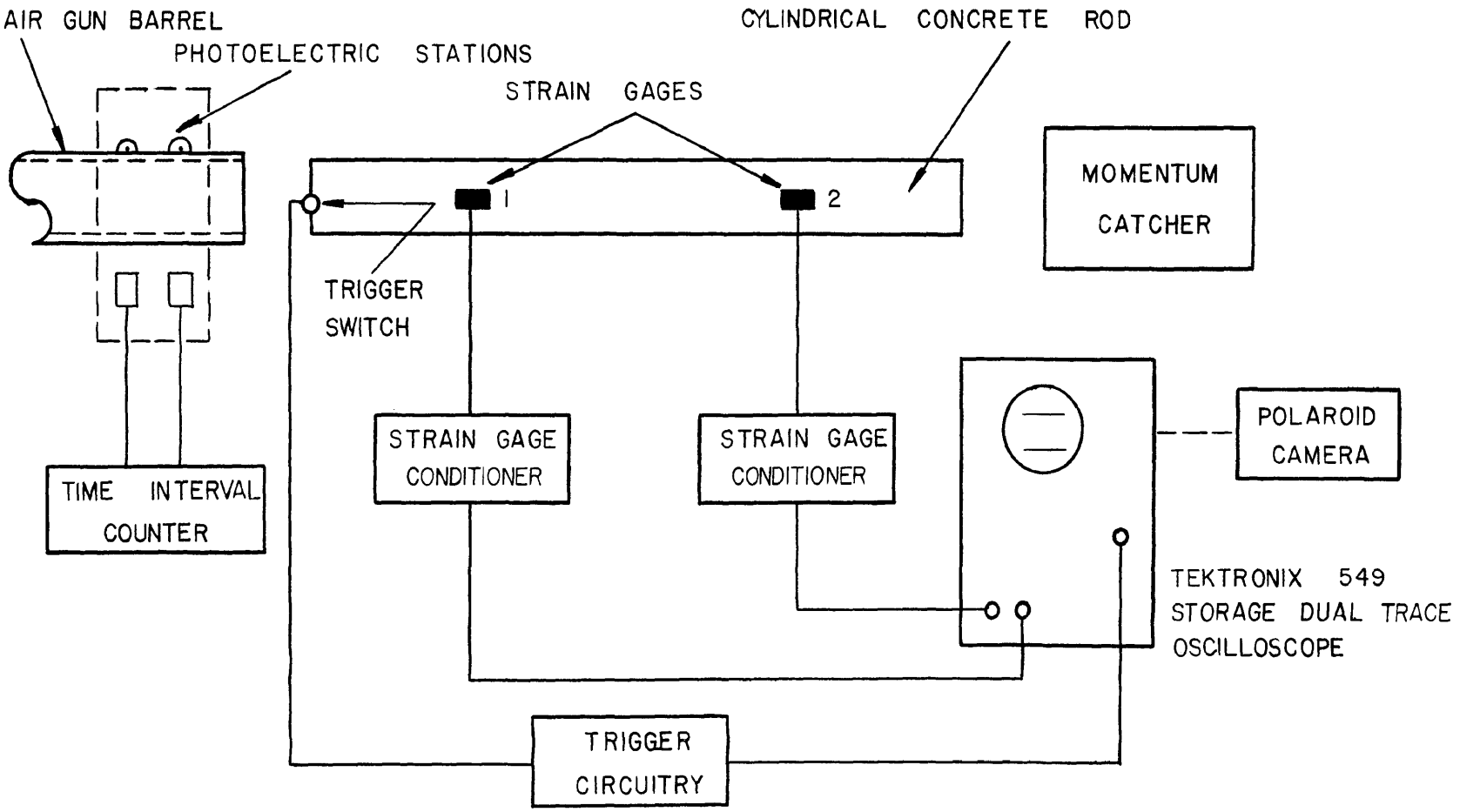

Figure 2.1 - Schematic of instrumentation for wave propagation and spallation experiments

Hopkinson-bar setup used by Davies (1948), Kolsky (1949), and described in a M.S. Thesis by Bai (1970). The instrumented bars, 24 inches long and 1.5 inches in diameter, were carefully aligned with the bore of the air gun. Spherical-nosed projectiles were used to improve the axial nature of the impact and thereby insure that misalignment would not significantly influence test results. The wave amplitude (strain) was governed by the nozzle velocity of the projectiles. The round nose also gives rise to longer rise times than if square-ended bars are used. The resulting lower stress gradients are desirable in the analysis.

The velocity of the projectile immediately prior to impact was measured with two photoelectric sensors in the vented section of the barrel and a time-interval counter, Bai (1970). The velocity was determined from the counter readings and photocell spacing. For the present tests, the striker bars were propelled at velocities on the order of 700 to 1350 in./sec. and strain amplitudes on the order of 800 to 1200 μ in./in. were produced. The test assembly is shown schematically in Figure 2.1 with typical oscilloscope records of strain vs. time at two gage locations shown in Figure 2.2.

The mechanical properties and dynamic tests of specimens were run at approximately the same time so that aging effects in the concrete were minimized.

D. ANALYSIS AND TEST RESULTS

The impact apparatus (Section C) and the simple wave propagation numerical analysis (Appendix A) were used to obtain data on wave propagation and interaction including the stress, strain, and strain-rate histories at the spall plane and the dynamic fracture strength. This information was then used in determining a spall tensile fracture criteria.

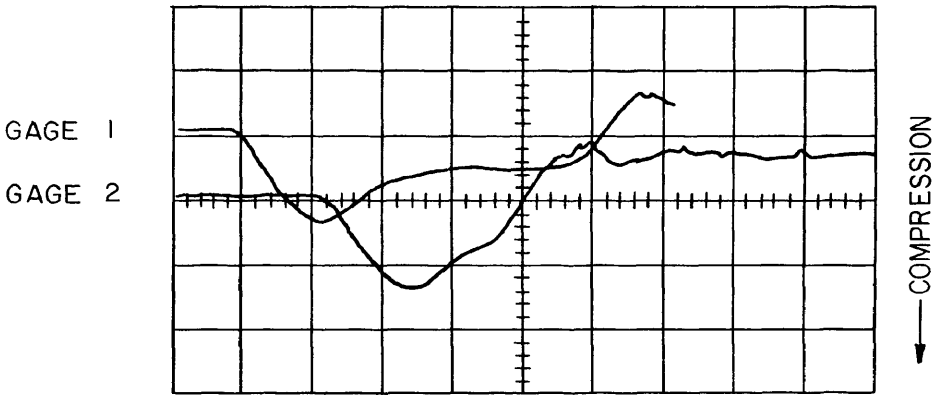

HORIZONTAL SCALE : 50 μSEC. PER MAJOR DIVISION

VERTICAL SCALE : 628.92 μIN./IN. PER MAJOR DIVISION

Figure 2.2 - Typical oscilloscope traces of longitudinal strain vs. time at 8 in. (gage 2) and 16 in. (gage 1) from free end. Traces are for specimen CC-H-2-1

A total of 10 instrumented long concrete specimens were subjected to dynamic loading. The strain waveforms at two gage stations were recorded as oscilloscope traces and later projected onto graph paper and digitized. The data were fed into a digital computer (IBM 360, Model 50) using a finite-difference code to compute stress (strain) at different locations x along the bar and at different times t. The density and bar velocity of the concrete bars and the incident waveform at the first gage location were inputs into the code. Note that the space and time distributions of stress differ from those of strain only by the constant E. The finite-difference values were input to a plotting code which graphically shows the strain(stress)-time, strain rate-time, and strain (stress)-distance relationships.

A technique for digitizing the enlarged oscilloscope records with an X-Y recorder, a small digital computer, and a paper tape punch was developed and used. This device decreased greatly the amount of physical work and the possibility of human error in manually transcribing the data.

The measured strains at the second strain gage were compared directly with those calculated with the computer code using the measured strain pulse at the first gage station as input and computed waveforms were compared by plots made with a Calcomp Model 750 magnetic tape plotter.

Details of the computational techniques were outlined in Appendix A. Both time and space origins (x=t=0) were arbitrarily established at the position of gages station 1 at the time when the loading wave first reached station 1. The mesh size was 0.05 inches.

1. Wave Propagation and Interaction

a. Bar Wave Velocity and Dynamic Modulus

The bar wave velocities were determined directly from the long bar spallation tests from measurements of the travel time of the incident compression pulse between station 1 and station 2. The velocities so obtained were those of high amplitude (up to 3900 psi) one-dimensional stress waves propagating longitudinally in cylindrical concrete rods.

The bar compressive wave velocities are shown in Table III along with other relevant properties for the concrete bars. An examination of the data indicates that the wave velocities did not vary much between batches of concrete used.

The measured rod velocities and the density of the concrete were used to calculate the dynamic compressive Young's modulus from the relation $E_d = \rho c^2$. The resulting values of E_d listed in Table III were inputs into the computer code for the numerical analysis.

As the static modulus of elasticity in compression and tension were found to be approximately the same (Table II) the corresponding dynamic values were likewise assumed to be nearly equal. This assumption was verified as is discussed later.

b. Comparison of Experimental and Theoretical Strains

In order to compare the theoretically predicted strains with the experimental strains for each specimen, the governing equations for the wave problem were solved by the method of finite difference as presented in Appendix A. The longitudinal strain comparisons (typical Figure 2.3a, and Figures B.1a to B.9a in Appendix B) of the "elastic" and experimental results, with a common time origin, for the concrete specimens indicate

TABLE III - SUMMARY OF RESULTS FOR THE CONCRETE BARS*

Bar No.	Striker Velocity, ips	Striker Length, in.	Bar Wave Velocity, c** 10^5, ips	Dynamic Modulus, E_d 10^6,psi	Fracture Locations*** in.	Crushed Length† in.	Maximum Experimental Strains, μ in./in. Sta.1	Sta.2
CC-H-1-1	702	4	1.297(8,16)	3.129	4-1/2, 7-3/4	3	790	770
CC-H-2-1	897	6	1.297(8,16)	3.151	4-1/2, 7-3/4	3	912	918
CC-J-2-1	1299	6	1.280(8,16)	3.106	5-5/8, 7-3/16	6	1195	1161
CC-J-3-1	1316	6	1.297(8,16)	3.191	4-3/8, 8	3	1105	1080
CC-J-4-1	1325	6	1.297(8,16)	3.188	3-3/4, 6-7/8	5	1140	1090
CC-K-1	866	8	1.333(6,16)	3.329	4-7/8, 7-1/8	4	1151	1042
CC-K-2	1351	6	1.304(6,16)	3.186	5-3/16, 8-5/8	4	1209	998
CC-L-1	840	4	1.333(6,16)	3.329	5-1/4, 6-9/16	2.5	828	836
CC-L-2	1250	4	1.304(6,16)	3.183	6 , 10-5/8	4.5	1021	914
CC-L-3	1220	8	1.333(6,16)	3.329	4-5/8, 8-3/4	4.5	948	1002††

* The bar length was 24 inches and the bar diameter was 1.47 inches.

** The numbers in parenthesis after the bar velocity indicate the gage station locations, in inches, from the free end of the bar between which the velocity was obtained. Station 2 is near free end of the bar.

*** Distances from the free end of the bar for the first two spalls.

† Length of crushed zone in the vicinity of the impact end.

†† Strain Gage 2 of specimen CC-L-3 was out of balance after test.

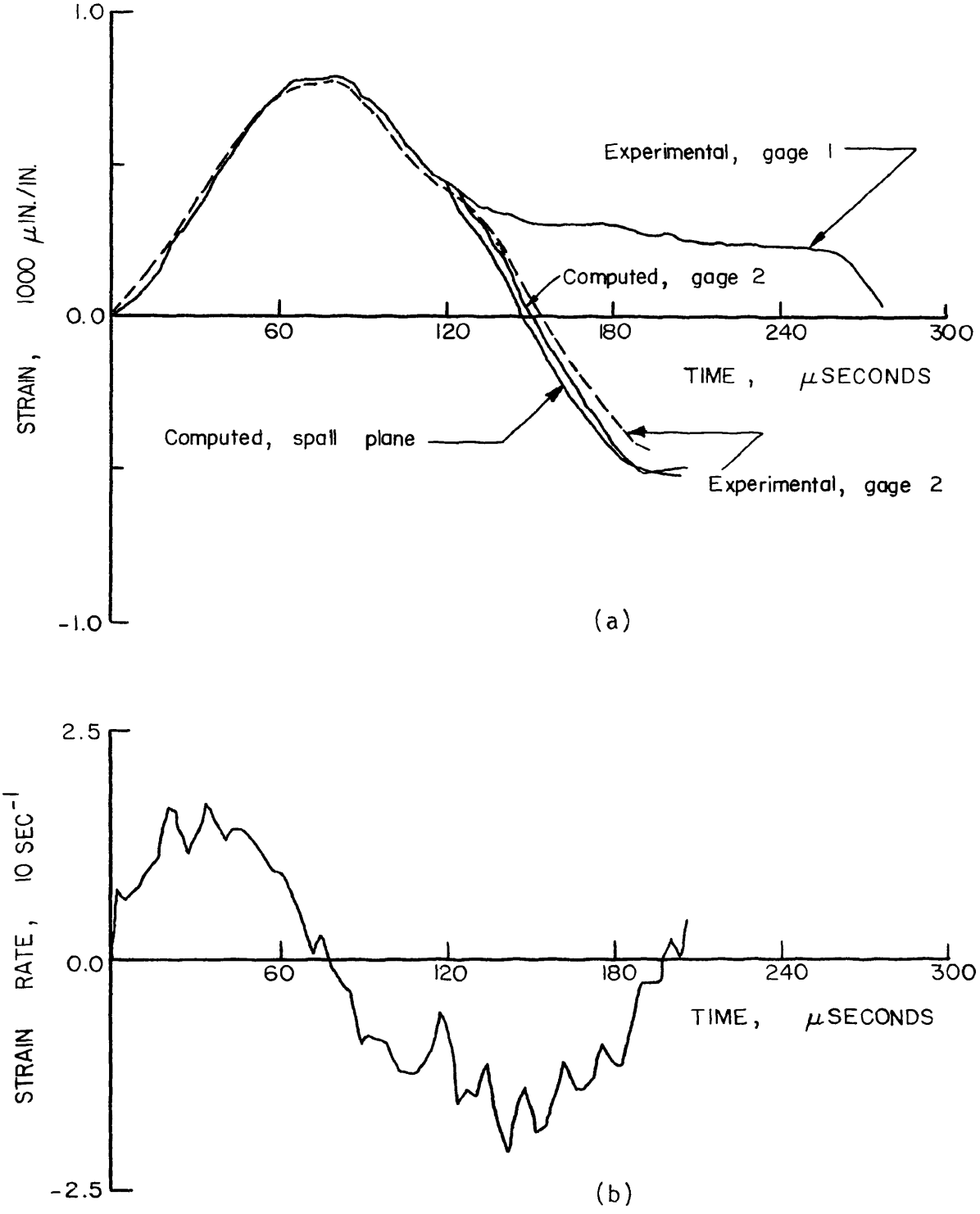

Figure 2.3 (a) - Comparison of experimental and theoretical strains for specimen CC-H-1-1 (compression positive)
(b) - Strain rate history at spall plane for specimen CC-H-1-1

that the "elastic" simple theory adequately predicts the magnitude and shape of the measured longitudinal pulses, except for the slight lag of the peak experimental strains for some tests. Also, the slight attenuation increases for an increasing pulse amplitude.

Geometric dispersion is believed to be a negligible source of error in these measurements since the ratio of the radius of the specimen to the average wave-length is quite small (0.023). The high frequency oscillations ordinarily superposed on the main pulse usually present whenever geometric dispersion is active, were not found in the data. Therefore the dispersion and attenuation of the wave in its travel over the 6-8 in. distance from station 1 to station 2 was negligible.

The results in Figures 2.3a and B.1a to B.9a indicate that the theoretically calculated tensile strains at station 2 were slightly higher than the experimentally measured ones. It is also particularly noteworthy that the wave arrival time and pulse shape resulting from wave interactions matched up very well with the experimentally observed wave after free end reflections. This is shown by the close agreement between the computed waves for gage 2 and the experimental values for gage 2 for times after the departure of the experimental curve for gage 1 from the correponding curve for gage 2. This agreement also verifies the assumption that the compressive and tensile wave speeds are nearly the same.

The theoretical calculated strains (stresses) are point values derived from average strains over a finite length. Such an average value will correspond more closely with the average strain measured by a strain gage. As an extrapolation of this reasoning, it is possible

to compare the experiment and analysis in terms of average strains over extremely large portions of the specimen in which widely different strain states exist within each portion. In these tests the gage length was small (0.25 in.) compared to the pulse length (30 in. to 35 in.) so that point and average values were essentially the same.

The gage records for a specimen in which a spall fracture has occurred shows the entire strain history including the peak strain and reloading which occurs when the spall cracks form and gives an indication of the time and rate of fracture. The experimental strain profiles have a more complicated tensile structure than the computed profiles, probably because of a number of spall cracks are activated until complete spall fracture occurs. These ideas are discussed further in the section on dynamic tensile fracture.

c. Stress, Strain, and Strain Rate History at Spall Plane

The one-dimensional finite-difference code to solve the stress-wave propagation and interaction problem, and the plotting code used for the analysis of the computer simulation results allowed the direct display of the theoretically predicted curves of stress (or strain) and strain rate at the spall plane vs. time (Figures 2.3 and B.1 to B.9). The spall occurred at the location of strain gage 2 for the specimen CC-J-3-1 and CC-L-2 so that the computed values at the spall plane are the same as those computed for gage 2 (see Figures B.3a and B.8a). The experimental values of strain rate at the spall plane were determined by numerically differentianting the strain-time curves for these same two specimens and are plotted in Figures B.3b and B.8b for comparison with the finite difference solution.

The complete description of the loading history at the spall plane and the state of stress along the bar at the time of fracture will be used later for determining a spall criteria.

2. Dynamic Fracture and Spall Tensile Fracture Criteria

a. Dynamic Compressive Strength

When a strong compression pulse is introduced at the impact end of the bar a section may be crushed if the compressive stresses are higher than the dynamic compressive strength S_c of the material. As the pulse progresses along the specimen, it crushes more material until the peak stress falls to some value S_c (Figure 2.4) which is probably a function of the impact velocity and the shape of the projectile nose.

As noted in the previous section, the wave propagation process is nearly linear after the pulse progresses beyond the crushing zone, and relatively little further losses occur. Hence it may be assumed without much error that the peak compressive stress in the pulse in the remainder of the bar remains equal to S_c.

Table IV and the graphs in Figures 2.5 to 2.7 show that the input to the intact bar zone is fairly linearly dependent on striker velocity; but apparently the mechanism of comminution of the vicinity of the impact end is not. That is, the extent of the crushed region varies greatly, even for approximately the same nozzle energy of the projectile. The momentum and kinetic energy of the projectile correlate with the dynamic compressive strength and crushed length in the same manner as the striker velocity thus with the strength and length. Slight differences in the dynamic compressive strength may produce big differences in the fragmentation process (crushing length) when the bar specimen is dynamically loaded with spherical-nosed cylindrical strikers. The dynamic compressive

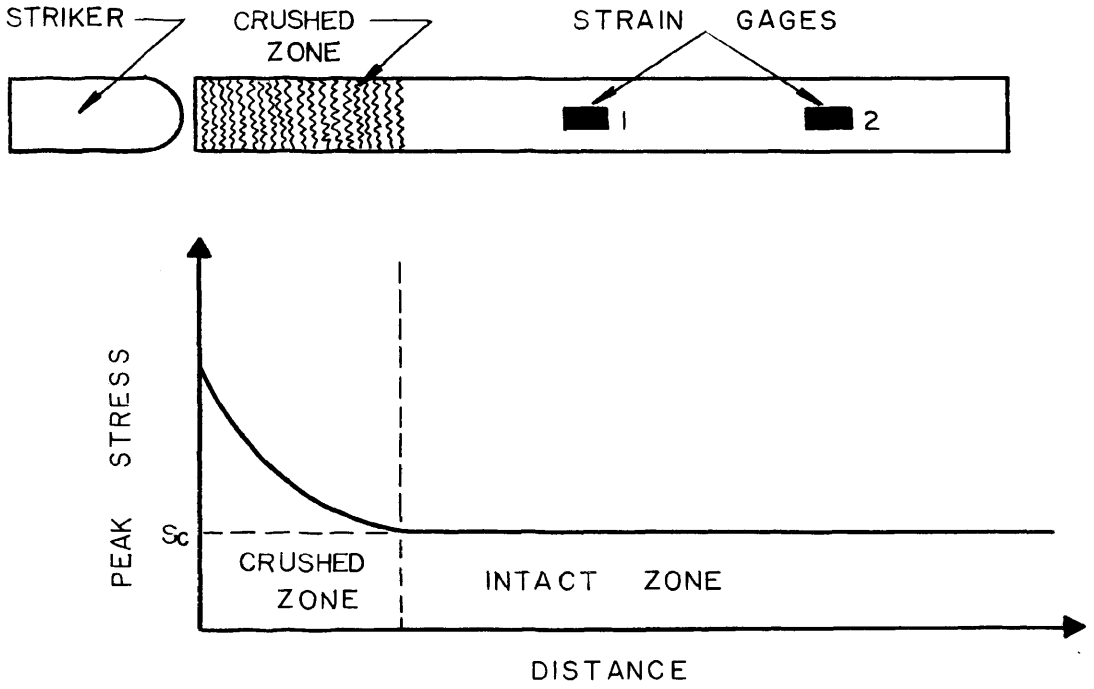

Figure 2.4 - Fracture by dynamic compression

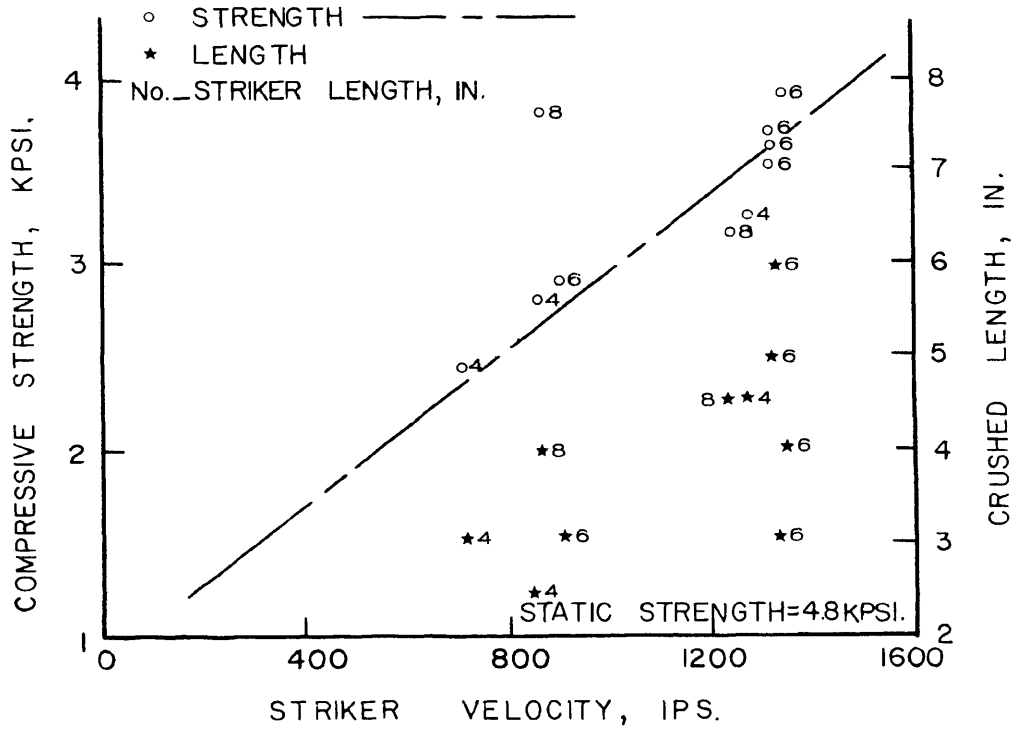

Figure 2.5 - Compressive strength and crushed length vs. striker velocity

TABLE IV - SUMMARY OF RESULTS FOR THE DYNAMIC COMPRESSIVE STRENGTH

Striker					
Velocity ips	Weight* Grs	Momentum Slug - ft/sec	Kinetic Energy Slug - ft^2/sec^2	Crushed Length, in.	Compressive Strength, kpsi
702	305.10(4)	1.22	35.74	3.0	2.474
840	305.10(4)	1.46	51.17	2.5	2.757
1250	305.10(4)	2.18	113.30	4.5	3.251
897	464.40(6)	2.38	88.82	3.0	2.874
1299	464.40(6)	3.44	186.20	6.0	3,712
1316	464.40(6)	3.49	191.10	3.0	3.525
1325	464.40(6)	3.51	193.80	5.0	3.637
1351	464.40(6)	3.58	201.40	4.0	3.854
866	627.00(8)	3.10	111.70	4.0	3.832
1220	627.00(8)	4.36	221.80	4.5	3.155

* The number appearing in parenthesis after striker weight denotes its length in inches.

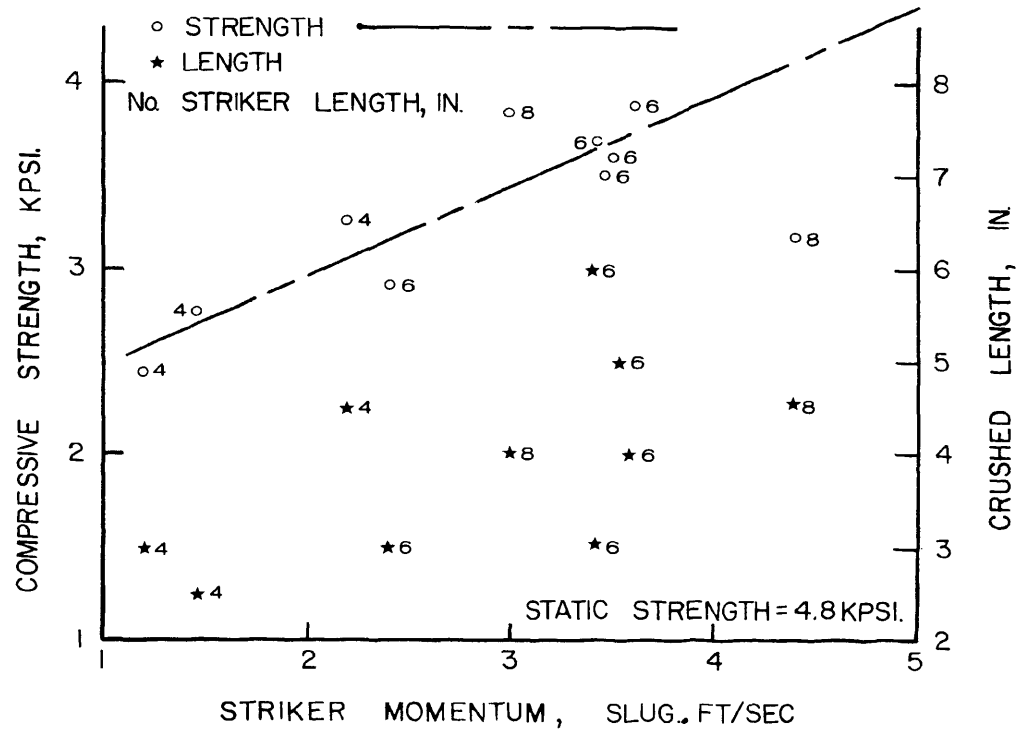

Figure 2.6 - Compressive strength and crushed length vs. striker momentum

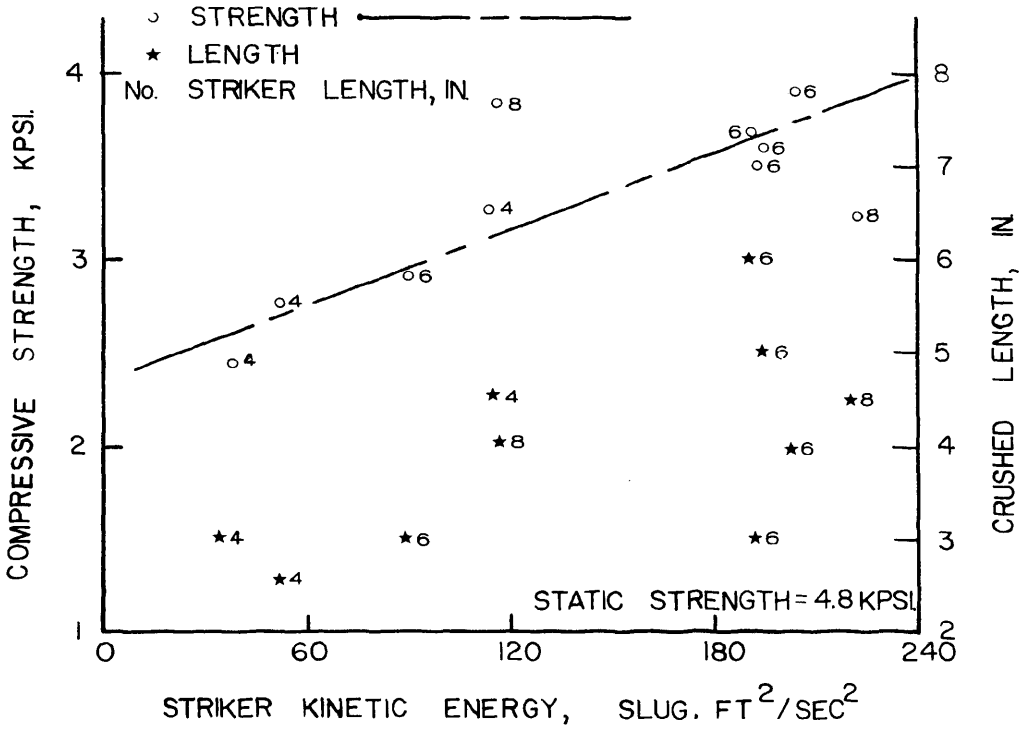

Figure 2.7 - Compressive strength and crushed length vs. striker kinetic energy

strength varied from 2474 to 3854 psi for the striker velocities range used. Stresses significantly higher than these could not be induced into the intact region by increasing the impact velocity. The higher energy of the striker would go mostly into additional comminution rather than stress wave energy into the intact portion of the bar.

b. Spallation and Dynamic Tensile Fracture Strength

On reaching the free end of the bar, the plane compressive elastic pulse is reflected to eventually become a tensile pulse of the same shape traveling in the reverse direction. The incident compressive wave and its reflected tensile counterpart interfere with each other (Figure 2.8) until at some time and distance from the free surface the resulting stress becomes tensile and reaches the value S_T, the dynamic tensile strength of the material. A piece then flies off from the main body of the bar, trapping part of the momentum of the wave. This phenomenon is referred to as spalling and the segment which breaks free is called a spall. If the pulse is sufficiently long, its tailing end will now suffer reflection at this newly fractured surface. A second spall will form in the same manner if the peak stress in the tail still exceeds S_T. This process continues until the intensity of the reflected pulse drops below S_T.

The main factors governing the spallation process (number and size of the spalls) are:

i. The dynamic compressive strength of the material, S_C, which determines the maximum compressive stress that can be transmitted.

ii. The dynamic tensile fracture strength of the crack free material.

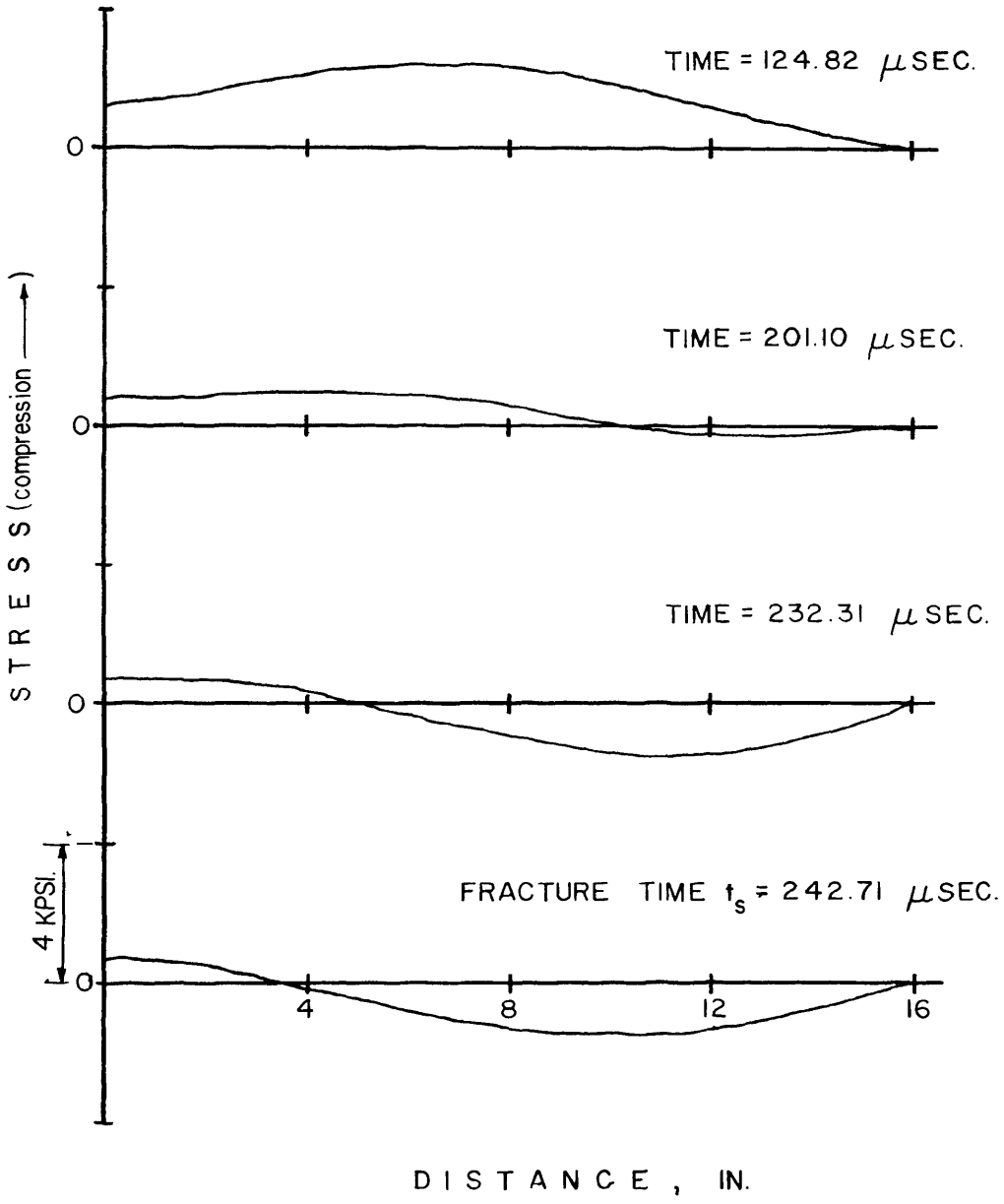

Figure 2.8 - Stress distribution along bar as compression pulse reflects from free end for specimen CC-H-1-1

iii. The initial defect structure in the rock.

iv. The shape of the incident pulse and applied stress history.

For spalls to form it is of course necessary that the initial peak stress in the input pulse be greater than the dynamic tensile strength, S_T, and, that S_c should be larger than S_T. $\frac{S_c}{S_T} > 1$ is the case for most materials, including rocks and concretes.

Before estimating the dynamic tensile fracture time and strength of concrete specimens, it is convenient to assume, as did Shockey, et al. (1972), that the tensile failure of rock and rock-like material occurs in four stages:

i. Activation of a number of pre-existing structural or cracklike defects,

ii. Propagation of activated cracks radially outward,

iii. Coalescence and branching of propagation cracks, and

iv. Isolation of individual rock fragments from one another (spall fragmentation).

The gage record for a specimen in which the spall fracture occurred on the gage location (Figures B.3 and B.8) yields information on the spallation process in addition to the spall strain history. Micro-seismic waves emitted as spall cracks form impinge on the gage and may result in a measured signal being superimposed on the main pulse. Also, the initiation and gradual extension of microcracks interferes with the normal wave propagation in the region which again may show up on the gage record just prior to complete spall separation. Furthermore, the changes in the slope of the resulting tensile pulse are an indication of the time and rate of fracture.

Figures 2.3 and B.1 to B.9 show the theoretical elastic wave profile predicted by the computer for the case where spall occurred at or near gage 2 located near the free end. The plots from gage 2 show the agreement between predicted and experimental measured strains the difference in the strain profiles as the spall forms. The experimental profiles have a different tensile structure than the computed profiles, probably because a number of spall cracks were activated before complete fragmentation and separation of spall segments.

The dynamic tensile fracture time can be obtained from the plots of strain and strain rates vs. time at gage 2 and the spall location. The experimental values at gage 2 depart abruptly from the computed values at gage 2 because of the commencement of unstable fracture propagation. The wave travel time from the spall location to gage 2 must be subtracted from the above departure time to give the fracture time. The time of spall and the spall location were used with the printed computer output to obtain the stress, strain and strain rate-time history up to fracture at the spall plane. This information was necessary for determining the spallation tensile fracture mechanical energy criteria.

The instantaneous critical spall stress σ_s, fracture spall strain ε_s, and fracture spall strain rate $\dot{\varepsilon}_s$ at the time of spall fracture initiation t_s are presented in Table V. It is noted that the fracture stress, or strain, increases with increasing instantaneous strain rate and decreases with increasing tensile rise time to fracture $(t_s - t_0)$. This was an indication of a time dependence of the spall strength in the bar impact experiments for concrete. A similar result was observed in plate impact experiments on metals, Butcher, et al., (1964).

TABLE V - SUMMARY OF SPALLATION RESULTS FOR CONCRETE BARS

Test No.	x_0 in.	x_s in.	$\Delta x = x_s - x_0$ in.	t_0 10^{-6}sec	t_s 10^{-6}sec	$\Delta t = t_s - t_0$ 10^{-6}sec	$c_* = \Delta x/\Delta t$ 10^5in./sec	$\alpha = c_*/c$ †
CC-H-1-1	3.38	8.25	4.87	147.90	179.10	31.20	1.56	1.20
CC-L-1	5.14	10.75	5.61	114.10	142.00	27.85	2.01	1.51
CC-H-2-1	4.37	8.25	3.88	146.00	174.00	27.93	1.38	1.06
CC-L-3	6.39	11.38	4.99	107.50	130.50	23.03	2.16	1.62
CC-L-2	6.17	10.00	3.83	119.40	140.60	21.19	1.80	1.38
CC-K-2	7.20	10.80	3.60	117.20	136.20	18.97	1.89	1.45
CC-K-1	6.62	11.10	4.48	110.70	129.30	18.55	2.41	1.81
CC-J-3-1	4.81	8.00	3.19	149.10	170.60	21.58	1.47	1.13
CC-J-4-1	5.61	9.10	3.49	134.20	155.10	20.95	1.66	1.27
CC-J-2-1	4.35	8.80	4.45	139.30	156.10	16.78	2.65	2.07

† The wave interaction factor defined on p. 44

TABLE V (cont.) - SUMMARY OF SPALLATION RESULTS FOR CONCRETE BARS

Test No.	σ_s psi	ε_s 10^{-6}in./in.	$\dot{\varepsilon}_s$ sec^{-1}	$\varepsilon_s/\Delta t$ †† sec^{-1}	$\varepsilon_s/\Delta x/c$ ††† sec^{-1}	P_c psi	$\sigma_s/\Delta x$ †††† psi/in.	W in.-lbs
CC-H-1-1	1345	429.70	11.34	13.77	11.47	2457	276.10	1.53
CC-L-1	1486	446.30	7.29	16.02	10.58	2755	264.80	1.88
CC-H-2-1	1525	484.50	15.19	17.34	16.23	2864	393.00	1.69
CC-L-3	1628	489.00	15.42	21.23	13.03	3153	326.20	1.65
CC-L-2	1710	537.00	22.05	25.34	18.23	3249	446.40	1.64
CC-K-2	1769	555.10	22.66	29.26	20.04	3850	491.30	1.63
CC-K-1	1798	540.00	24.36	29.11	16.03	3814	401.30	1.54
CC-J-3-1	1807	566.20	24.86	26.24	23.08	3523	566.40	1.79
CC-J-4-1	1865	584.80	27.95	27.91	21.78	3634	534.30	1.79
CC-J-2-1	1962	631.50	32.54	37.63	18.16	3701	440.80	1.67
AVERAGE								1.68

†† The derived strain rate $\dot{\varepsilon}_{sd}$ defined by the thesis author on p. 47

††† The apparent strain rate $\dot{\varepsilon}_a$ defined by Birkimer (1970) on p. 44

†††† The derived tensile stress gradient defined by the thesis author on p. 42

TABLE V (cont.) - SUMMARY OF SPALLATION RESULTS FOR CONCRETE BARS

Test No.	U	K_w	β_w*	K_u	β_u**
	in.-lbs	psi^2-sec		$Kpsi^2$-in.	
CC-H-1-1	0.92	21.70	1.154	3.401	1.158
CC-L-1	1.66	27.65	1.350	6.535	1.583
CC-H-2-1	0.91	24.24	1.120	3.408	1.133
CC-L-3	1.54	24.20	1.190	6.046	1.372
CC-L-2	1.18	23.56	1.141	4.442	1.190
CC-K-2	1.31	23.56	1.191	4.927	1.312
CC-K-1	1.57	22.67	1.134	6.186	1.281
CC-J-3-1	1.03	26.00	1.107	3.890	1.120
CC-J-4-1	1.22	25.97	1.070	4.588	1.134
CC-J-2-1	1.39	23.79	1.105	5.079	0.890
AVERAGE	1.27	24.33	1.156	4.850	1.217

* β_w = Nonlinearity factor $K_w/(\sigma_s{}^2\Delta t/3)$

* β_u = Nonlinearity factor $K_u/(\sigma_s{}^2\Delta x/3)$

It is also observed (Table V) that the spall stress σ_s depends on the thickness of the tensile stressed zone (x_s-x_0). A narrow zone requires a larger tension for fracture and indicates a spatial dependence on the tensile strength.

c. Spallation Tensile Fracture Criteria

There is a sufficient amount of experimental and theoretical evidence to indicate that Rinehart's original spallation criterion of constant critical normal fracture stress should be modified. This criterion states that a spall will form instantaneously when a unique minimum value of normal net tensile stress is attained. This criterion has led to inaccurate predictions of spall in several instances. Disparities occur, in particular, in the thicknesses and number of spalls produced in multiple-spall experiments.

Some investigators explained the previously discussed discrepancies by assuming a time(spatial)-dependent spall mechanism; but Rinehart and Ahlquist (1970) felt that the critical normal fracture stress of a material depends on the transient compressive stress immediately preceding tension and on the state of stress at the time of fracture initiation. First, they believed that the action takes place very quickly in an exceedingly thin region so that statistically the probability is small of encountering one or more of the large flaws that contribute so significantly to the reduction of strength of most rocks under tension. They also conceived that the compressive wave that has just passed by the region of fracture (precompression) has strengthened the rock by collapsing some of the larger flaws. Secondly, they favored the idea that the state of stress at the time of fracture is not the same as that existing when the material is fractured by static loading. Just before the rock

spalls a state of plane strain exists along the incipient fracture plane. It therefore seems highly probable that lateral constraints imposed on the region of fracture could effectively increase the strength of the rock manifold.

To help resolve some of the above controversy, an attempt was made to study the effects that the compression phase of the stress-time history has on the spall behavior of brittle materials.

The following results (drawn from Table V and Figures 2.9 and 2.10) appear significant:

(1) the stress-dependent fracture tensile delay time Δt decreases with increasing tensile strength σ_s.

(2) the tensile fracture strength σ_s increases in an approximately linear manner with increasing peak compressive stress P_c. For example, the tensile stress required to form a spall increases by about 40 percent when the magnitude of the preceding compressive pulse increases about 50 percent.

(3) the tensile fracture stress σ_s increases with increasing fracture loading rate $\dot{\varepsilon}_s$.

(4) the fracture loading rate $\dot{\varepsilon}_s$ also increases with increasing precompression P_c.

(5) the fracture time Δt decreases with increasing peak compressive stress P_c.

Since it is observed that the spall strength is also a function of rate of loading, the precompression explanation of the increased tensile strength may not be unique. If an increased precompression produced a greater amount of crack nucleation, one might expect a decrease in the tensile strength, which is contrary to the trend found.

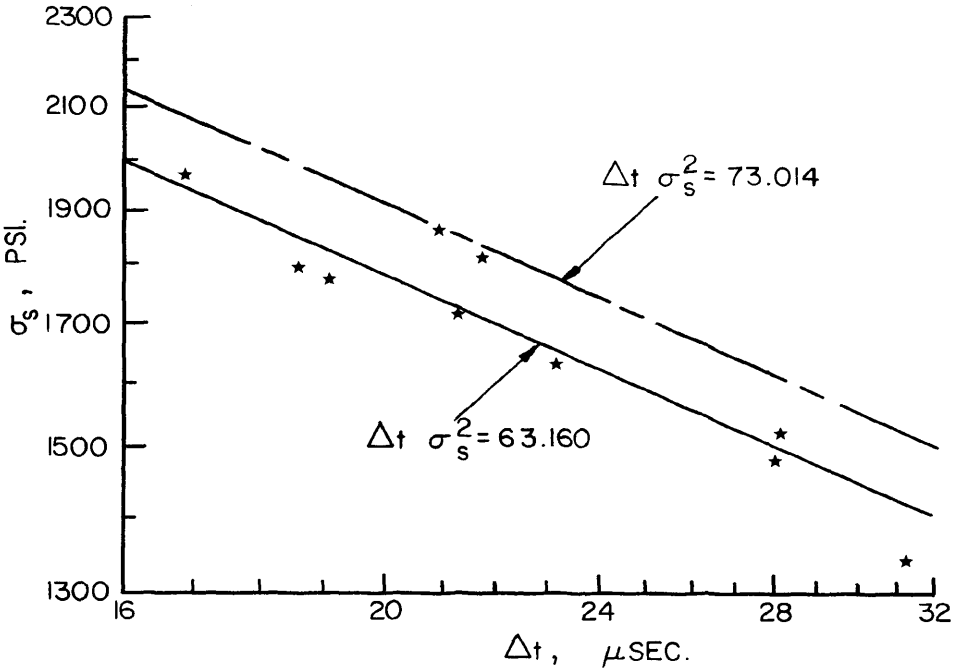

Figure 2.9 - Tensile spall strength σ_s vs. fracture delay time Δt

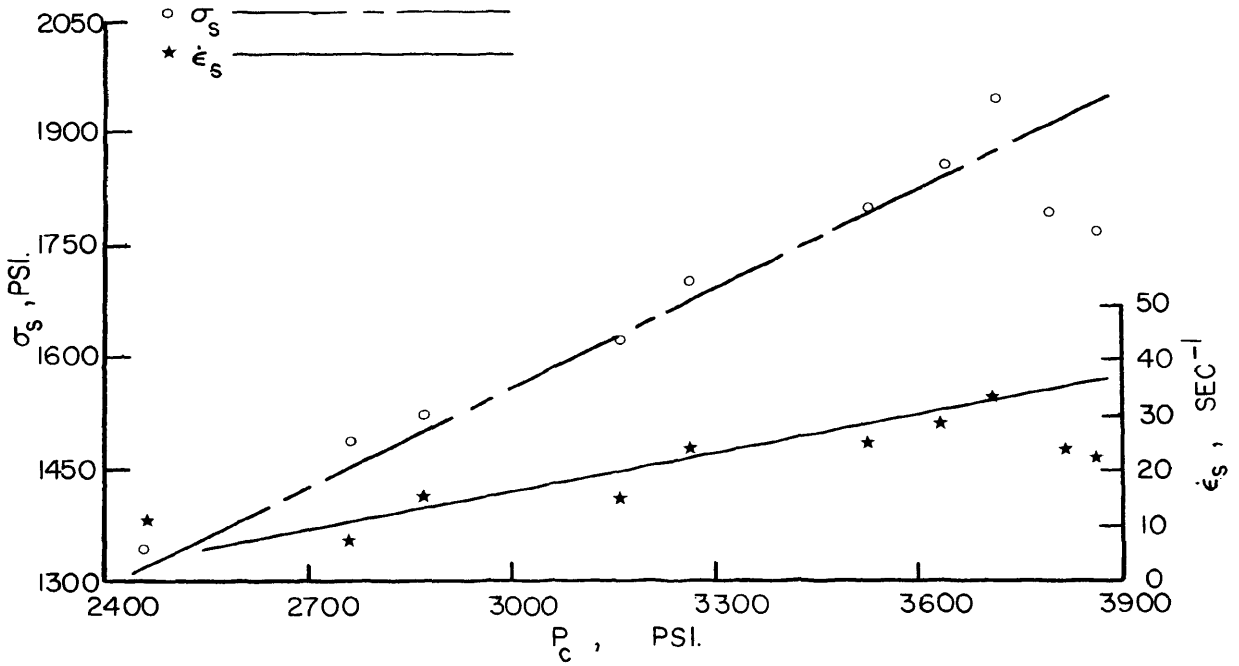

Figure 2.10 - Tensile spall strength σ_s and strain rate at spall time $\dot{\varepsilon}_s$ vs. peak compressive stress P_c

It is thought that other parameters, in addition to the critical tensile strength at the spall plane, should be included in the spall criterion, such as the distribution of stresses in space and time. Parameters that have been found experimentally to influence the spall behavior of materials are the tensile pulse duration at the spall plane, the critical spall stress at which tensile fracture begins, the size of the critically stressed region, the precompression of the material at the spall plane, state of stress at time of fracture, ambient temperature, and the material surface energy.

i. Critical Normal Fracture Strain Energy

When an elastic body is under the action of external forces, the body deforms and work is done by these forces. If a strained, perfectly elastic body is allowed to recover slowly to its unstrained state, it is capable of giving back all the work done by these external forces. For this reason the work done in straining such a body may be regarded as energy stored in the body and is called the "strain energy".

From the computer elastic wave propagation simulation the stress distribution along the bar was numerically known for different times, i.e., $\sigma(x,t)$. Therefore, at the time of fracture, the stress along the bar could be determined and represented by $\sigma_{bar}(x) = \sigma(x, \text{time of fracture})$. (See typical stress distribution in Figure 2.11).

Static fracture criteria are sometimes stated in terms of stored strain energy. Therefore, it may be reasonable to describe a spatial dependent criterion in terms of the strain energy stored within the bar material in the tensile stressed region of the net stress pulse to the left of the spall, U (see Figure 2.11).

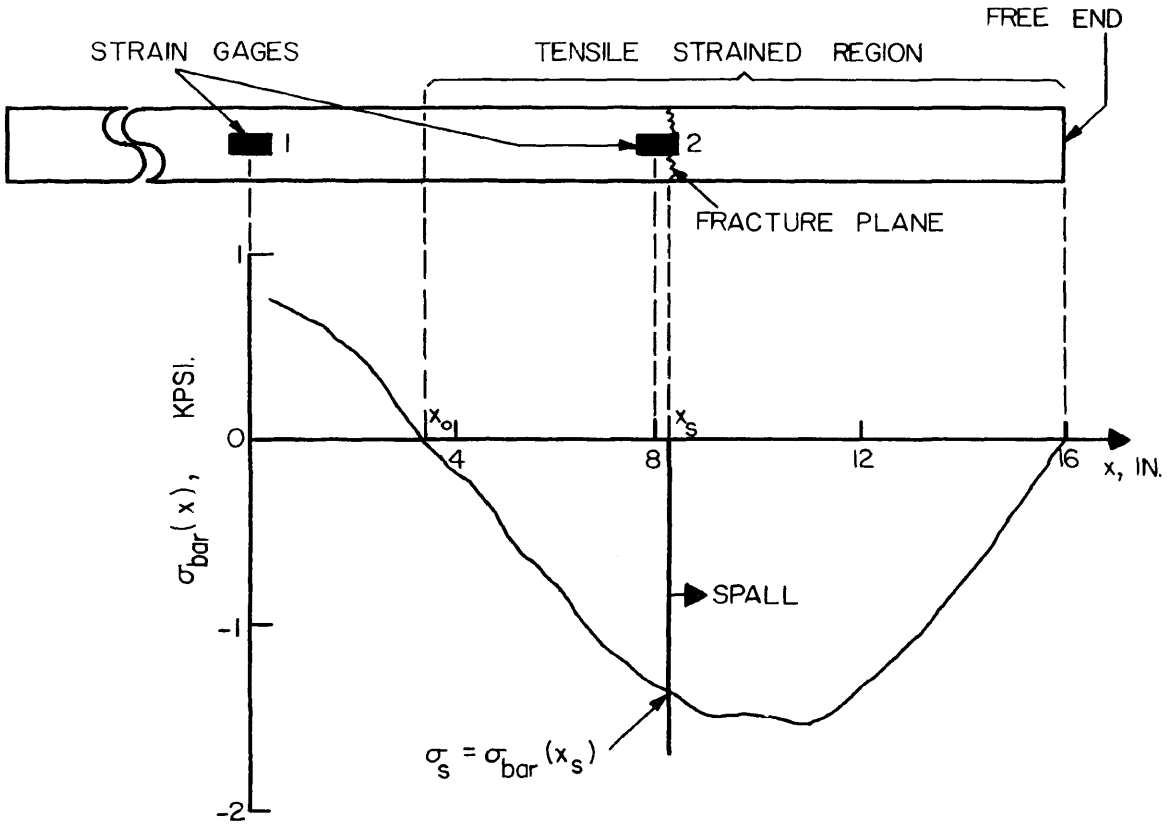

Figure 2.11 - Stress distribution along the bar at tensile fracture time t_s for specimen CC-H-1-1 (compression positive)

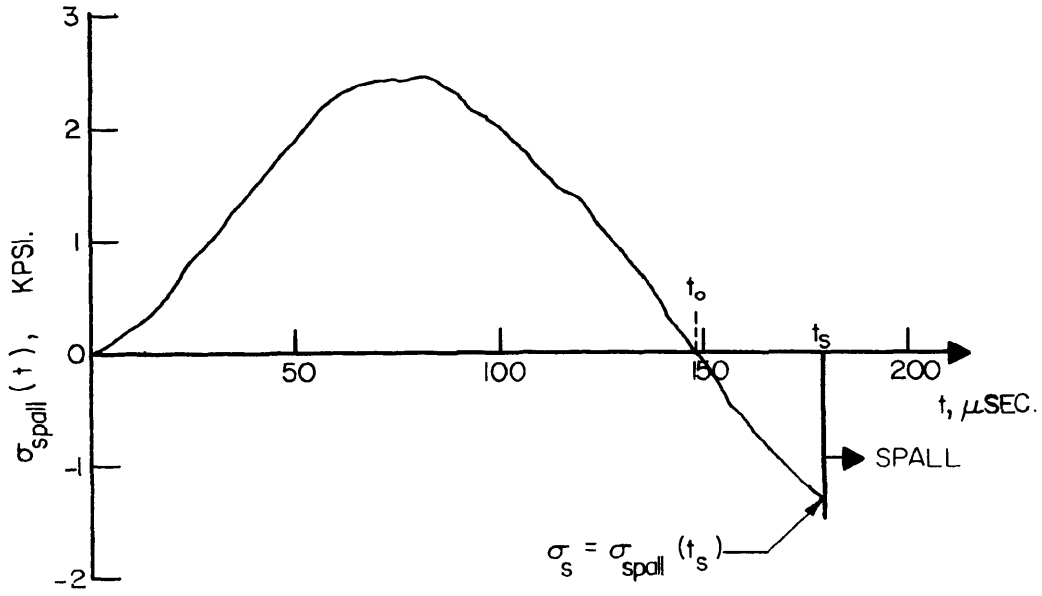

Figure 2.12 - Stress-time history at the spall plane for specimen CC-H-1-1 (compression positive)

A spallation criterion based on this concept has the form

$$U = \frac{A}{2E} \int_{x_0}^{x_s} \sigma_{bar}^2(x)dx \qquad (2.1)$$

where

$\sigma_{bar}(x)$ = the instantaneous net tensile stress along bar to the left of x_s at time t_s.

x_s = the location of spall plane.

x_0 = the location of zero tensile stress.

E = the Young's modulus of elasticity.

A = the cross-sectional area of bar.

Birkimer (1970) proposed the application of the critical fracutre strain energy theory, represented by Equation (2.1). He concluded that for his tabulated "minimum" calculated strength values the "critical" fracture strain energy can be considered relatively constant regardless of the "apparent" strain rate which he defined as the ratio of fracture strain ε_s to the rise time of the straining pulse to that fracture strain $(t_s - t_0)$.

Equation (2.1) was integrated numerically for the experimental and computed data at the first and second spall plane near the free bar end and the measured and calculated values of interest listed in Table V. From this tabulation, it is noted that the tensile fracture strain energy to the left of the spall U may be considered relatively constant regardless of the stress or deformation rates up to fracture and spall location. It is concluded that the use of minimum strength values (i.e., neglecting higher values) is not

required as was done by Birkimer (1970). It may be true that there is a restriction in the method of experiment or analysis rather than true material behavior during spallation. Errors due to interference of the incident compressional and reflected tensile pulses, which were not considered in Birkimer's analysis, may explain the necessity of using minimum strength values and also the difference in the value of average tensile fracture strain energy. The tensile fracture strain energy in this investigation was found to be 1.27 ± 0.38 in.-lbs. compared to 3.41 ± 0.48 in.-lbs. given by Birkimer (1968) for a similar concrete mix subjected to approximately the same apparent strain rates. This difference may also be due to the fact that the concrete used by Birkimer (1968) was stronger, having a static compressive strength of 6830 psi and an elastic modulus of 4.61×10^6 psi as compared to corresponding values of 4805 psi and 2.37×10^6 psi for the material used in this investigation.

ii. Critical Normal Fracture Mechanical Energy

Since fracture may also be considered basically a mechanism of energy transfer of mechanical energy to new surface energy, it may be more realistic to describe a time-dependent spall in terms of total mechanical energy passing through the spall plane up to the time of fracture. This energy W may be empirically constant for a given material. A spallation criterion based on this concept would have the form

$$W = A \int_{t_0}^{t_s} \sigma_{spall}(t)\, V_{spall}(t)\, dt \qquad (2.2)$$

where

σ_{spall} = the instantaneous net tensile stress at the spall plane

V_{spall} = the instantaneous net particle velocity at the spall plane

t = the length of time for which the spall plane has been in tension

t_s = the time at which spall fracture initiates

t_0 = the time at which the spall plane first experiences a tensile stress

A = the cross-sectional area of bar

If the material is assumed to be linearly elastic, $\sigma = \rho c v$, and Equation (2.2) becomes

$$W = \frac{A}{\rho c} \int_{t_0}^{t_s} \sigma^2_{spall}(t)\, dt \qquad (2.3)$$

where

ρ = the mass density

c = the bar wave speed

As $c = \sqrt{E/\rho}$, then Equation (2.3) becomes

$$W = \frac{Ac}{E} \int_{t_0}^{t_s} \sigma^2_{spall}(t)\, dt \qquad (2.4)$$

The stress-time history at the spall plane (shown typically in Figure 2.12) is given directly by the strain gage readings when spall occurs at the gage location, or theoretically by the computer elastic

simulation as discussed in 1.c.

Equation (2.4) was also numerically integrated using the experimental and theoretical data at the first two spall planes near the free end of the bar. The values of the tensile fracture mechanical energy W introduced into spall plane (Table V) are fairly constant regardless of the stress or strain rates up to fracture and spall location. The computed value of the tensile fracture mechanical energy was found to be 1.68 ± 0.18 in.-lbs. for concrete specimens. It is seen in this tabulation that W is more nearly constant than U, and the values of W are generally higher.

The use of mechanical energy W in the spallation criterion rather than stored strain energy U has the advantage that the former can also be applied when the incident compression pulse has a short rise time while the latter cannot ($x_s - x_0 = 0$). This limitation on the latter quantity was pointed out by Rinehart and Ahlquist (1970).

iii. Dependence of Strength on Stress Gradient and Rate

The critical normal fracture strain energy criterion of Equation (2.1) can be simplified and stated in terms of the fracture tensile stress with the simplifying assumption that the stress $\sigma_{bar}(x)$ in the tensile strained portion to the left of spall increases linearly along the bar. That is:

$$\int_{x_0}^{x_s} \sigma_{bar}^2(x)dx = \frac{1}{3}\sigma_s^2(x_s - x_0) \qquad (2.5)$$

Therefore, Equation (2.1) yields:

$$\Delta x \sigma_s^2 = \frac{6EU}{A} = C_1 \tag{2.6}$$

where

$\Delta x = x_s - x_0$ is the length of the tensile strained region to the left of fracture plane (Figure 2.11).

When the quantity on the left of Equation (2.6) becomes equal to or greater than C_1, fracture initiates. The space length criterion [Equation (2.6) or Equation (2.1)] has an undesirable property that it implies that for a very small space increment Δx the fracture strength becomes infinite, and conversely for large space increments it becomes zero.

The simplified fracture tensile strain energy criterion of Equation (2.6) can also be expressed equivalently as either a stress or strain gradient criterion

$$\sigma_s = \left(\frac{6EU}{A}\right)^{1/3}\left(\frac{\sigma_s}{\Delta x}\right)^{1/3} = C_2\left(\frac{\Delta\sigma}{\Delta x}\right)^{1/3} \tag{2.7}$$

or

$$\varepsilon_s = \left(\frac{6U}{AE^2}\right)^{1/3}\left(\frac{\sigma_s}{\Delta x}\right)^{1/3} = C_3\left(\frac{\Delta\sigma}{\Delta x}\right)^{1/3} \tag{2.7a}$$

where $\frac{\Delta\sigma}{\Delta x} = \frac{\sigma_s}{\Delta x}$ is the derived tensile stress gradient to the left of the spall plane in Figure 2.11.

Birkimer (1970) made a second assumption to introduce his stress (strain) pulse duration criterion, namely that the phase related

errors due to interference of the main compressional and reflected tensile pulse are negligible. That is:

$$\Delta x = c\Delta\tau \tag{2.8}$$

or

$$\frac{\Delta\sigma}{\Delta x} = \frac{1}{c}\frac{\Delta\sigma}{\Delta\tau} \tag{2.8a}$$

where $\Delta\tau$ is the apparent tensile duration. It should be noted that $\Delta\tau$ is an approximation for the tensile loading time from zero tension to fracture tension.

Substituting Equation (2.8a) into Equation (2.6) one obtains

$$\Delta\tau\ \sigma_s^2 = \frac{6EU}{Ac} = C_4 \tag{2.9}$$

When the quantity on the left of Equation (2.9) becomes equal or greater than C_4, fracture initiates.

The impulse criterion of Equation (2.9) implies that for very long (or small) time durations of applied tensile stress the fracture strength approaches zero (or infinite). This is also an undesirable feature of the criterion.

Birkimer's expression (1970) for the dynamic tensile strength [from Equation (2.9)] was

$$\sigma_s = \left(\frac{6EU}{Ac}\right)^{1/3}\left(\frac{\Delta\sigma}{\Delta\tau}\right)^{1/3} = C_5\,\dot{\sigma}_a^{\,1/3} \tag{2.10}$$

or

$$\varepsilon_s = \left(\frac{6U}{AcE^2}\right)^{1/3}\left(\frac{\Delta\sigma}{\Delta\tau}\right)^{1/3} = C_6\,\dot{\sigma}_a^{1/3} \tag{2.10a}$$

where

$$\dot{\varepsilon}_a = \frac{\varepsilon_s}{\Delta x/c} = \frac{\varepsilon_s}{\Delta\tau} = \text{"apparent" strain rate}$$

$$\dot{\sigma}_a = E\dot{\varepsilon}_a = \text{"apparent" stress rate.}$$

Therefore, the empirical relation between the spall stress and the cube root of the stress gradient or stress rate (Equation 2.7 or Equation 2.10) to describe time-dependent dynamic failure is in fact equivalent to the critical normal fracture strain energy, (Equation 2.11).

$$\int_0^{\Delta x} \sigma_{bar}^2(x)\,dx = \frac{2EU}{A} = \text{constant } K_u \tag{2.11}$$

This fracture criterion states that when the damage integral on some particular plane exceeds the critical energy value K_u, fracture initiates on that plane.

It is concluded that the substitution of the true tensile loading time interval which considers wave interactions for the assumed interval $\Delta\tau = \Delta x/c$ would result in more realistic rate values. Table V gives values for the apparent-time to true-time ratio, α. A better

expression for σ_s will be given by the stress (strain) gradient model rather than by the "apparent" stress (strain) rate criterion.

The assumption of a linear tensile stress-distance dependence (or constant spatial stress gradient to the left of spall) at fracture time may be a poor approximation in certain cases, depending on the shape of the waveform. This is seen by comparing the values of β_u in Table V, where β_u is the ratio of the true integral value, K_u, to the approximated integral value, $\sigma_s^2 \Delta x/3$.

The stress gradient model indicates that the fracture stress (strain) increases with increasing apparent tensile stress gradient at fracture, which is fairly true for the tabulated values in Table V.

Certainly the experimental minimum strength values reported by Birkimer (1970) do not contradict his apparent strain-rate one-third-power model. On the other hand Equation 2.10 in Table V and Figure 2.13 show that a poor correlation exists between spall stress σ_s and cube root of the apparent strain rate $\dot{\varepsilon}_a$. It is concluded that the two main assumptions made in the analysis may reduce the applicability of this model as was the case in this investigation.

A better simplified stress (or strain) rate dependence model for predicting the time dependent strength σ_s is proposed using the constant tensile fracture mechanical energy W. For a linear tensile stress-time history at spall

$$\int_{t_0}^{t_s} \sigma^2_{spall}(t)dt = \frac{1}{3}\sigma_s^2(t_s - t_0) \qquad (2.12)$$

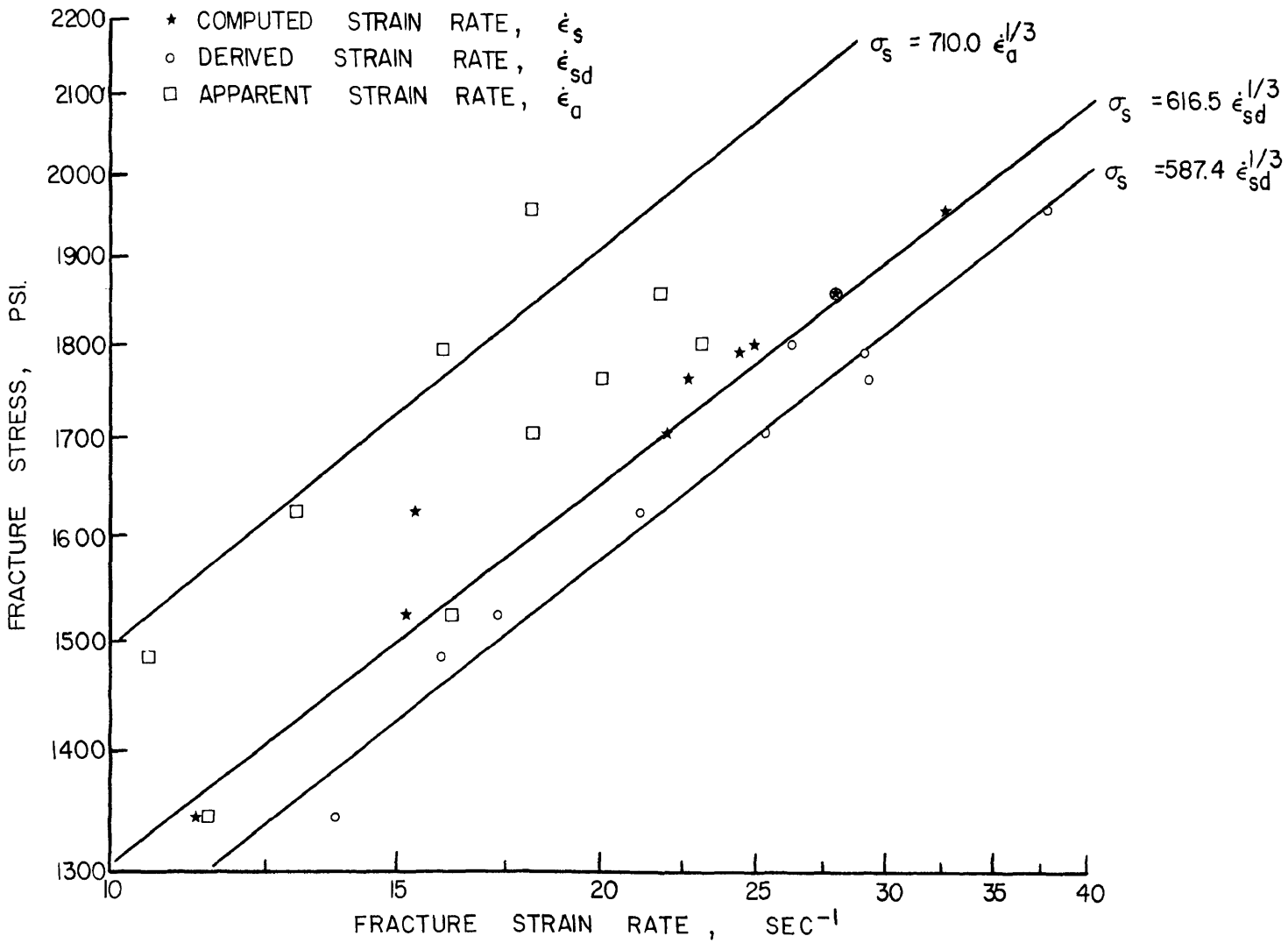

Figure 2.13 - Tensile fracture stress σ_s vs. fracture strain rate $\dot{\epsilon}_s$, $\dot{\epsilon}_{sd}$, or $\dot{\epsilon}_a$

Then, an impulse criterion is obtained from Equation (2.4),

$$\Delta t\ \sigma_s^2 = \frac{3EW}{Ac} = C_7 \tag{2.13}$$

where

$\Delta t = t_s - t_0$ is the finite tensile delay time required for fracture (crack) initiation.

Equation (2.13) represents the time-to-failure as a function of stress at the spall plane. It also has the undesirable property of predicting $\sigma_s = 0$ when Δt is very large. The results in Table V and Figure (2.9) show that the spall stress of the concrete is time dependent and increases with decreasing time of tensile loading.

The derived strain rate, $\dot{\varepsilon}_{sd}$, (Table V) is defined as the fracture strain divided by the rise time to fracture in the tensile spall history.

$$\dot{\varepsilon}_{sd} = \frac{\varepsilon_s}{\Delta t} \tag{2.14}$$

From Equations (2.13) and (2.14) the following is obtained

$$\sigma_s = \left(\frac{3E^2W}{Ac}\right)^{1/3} \dot{\varepsilon}_{sd}^{1/3} = C_8\ \dot{\varepsilon}_{sd}^{1/3} \tag{2.15}$$

or

$$\varepsilon_s = \left(\frac{3W}{EAc}\right)^{1/3} \dot{\varepsilon}_{sd}^{1/3} = C_9\ \dot{\varepsilon}_{sd}^{1/3} \tag{2.15a}$$

Therefore, a criterion relating fracture stress to the cube root of the stress (strain) rate has been shown to be equivalent to the critical normal fracture mechanical energy,

$$\int_0^{\Delta t} \sigma^2_{spall}(t)dt = \frac{EW}{Ac} = \text{constant } K_W \qquad (2.16)$$

This fracture criterion imples that when the damage integral on some particular plane becomes equal ore greater than the critical energy value K_W, fracture initiates on that plane.

Table V and Figure 2.13 show that in this experimental investigation, the strength values σ_s correlate fairly well with the cube root of the "derived" strain rate. This is seen by comparing the values of β_W in Table V, where β_W is the ratio of the true integral value, K_W, to the approximate integral value, $\sigma_s^2 \Delta t/3$. It is concluded from the above comparisons that the linear tensile stress-time assumption may not drastically limit the application of the simplified mechanical energy model [Equation (2.13) or (2.15)].

Also from Table V and Figure 2.13 it is noted that at fracture the derived strain rate $\varepsilon_s/\Delta t$ is a better approximation to the instantaneous strain rate at the time of fracture $\dot{\varepsilon}_s$ than is the apparent strain rate $\varepsilon_s/(\Delta x/c)$.

The several empirical spallation criteria discussed above are summarized in Table VI along with corresponding values of the various constants for the particular concrete.

TABLE VI - EMPIRICAL SPALLATION CRITERIA FOR CONCRETE*

Critical Normal Fracture Strain Energy				Critical Normal Fracture Mechanical Energy			
	Relation		Equation Number		Relation		Equation Number
1	$\int_0^{\Delta x} \sigma_{bar}^2(x)dx$	$= 4.850 \times 10^6$	2.11	1	$\int_0^{\Delta t} \sigma_{spall}^2(t)dt$	$= 24.33$	2.16
1	$\Delta x \sigma_s^2$	$= 11.95 \times 10^6$					
2	$\Delta x \sigma_s^2$	$= 14.55 \times 10^6$	2.6				
3	$\Delta \tau \sigma_s^2$	$= 111.0$	2.9	2	$\Delta t \sigma_s^2$	$= 73.01$	2.13
				1	$\Delta t \sigma_s^2$	$= 63.16$	
1	σ_s	$= 228.7 \left(\frac{\Delta\sigma}{\Delta x}\right)^{1/3}$					
2	σ_s	$= 244.2 \left(\frac{\Delta\sigma}{\Delta x}\right)^{1/3}$	2.7				
3	σ_s	$= 4.810\, \dot{\sigma}_a^{1/3} = 710 \dot{\varepsilon}_a^{1/3}$	2.10	2	σ_s	$= 616.5 \dot{\varepsilon}_{sd}^{1/3}$	2.15
				1	σ_s	$= 587.4 \dot{\varepsilon}_{sd}^{1/3}$	
1	ε_s	$= 7.12 \times 10^{-5} \left(\frac{\Delta\sigma}{\Delta x}\right)^{1/3}$					
2	ε_s	$= 7.60 \times 10^{-5} \left(\frac{\Delta\sigma}{\Delta x}\right)^{1/3}$	2.7a				

TABLE VI (cont.) - EMPIRICAL SPALLATION CRITERIA FOR CONCRETE*

Critical Normal Fracture Strain Energy			Critical Normal Fracture Mechanical Energy		
	Relation	Equation Number		Relation	Equation Number
3	$\varepsilon_s = 1.497 \times 10^{-6} \dot{\sigma}_a^{1/3} = 2.209 \times 10^{-4} \dot{\varepsilon}_a^{1/3}$	2.10a	2	$\varepsilon_s = 1.925 \times 10^{-4} \dot{\varepsilon}_{sd}^{1/3}$	2.15a
			1	$\varepsilon_s = 1.830 \times 10^{-4} \dot{\varepsilon}_{sd}^{1/3}$	
3	$\varepsilon_s = 2.060 \times 10^{-4} \dot{\varepsilon}_a^{1/3}$ (Birkimer, 1968)				

* σ_s in psi; ε_s in in./in.; $\dot{\varepsilon}_s$ in sec^{-1}; Δt in sec; and Δx in in.

1 Average value calculated from numerical integration of tensile stress pulse.

2 Average value based on linear approximation of tensile stress pulse.

3 Average value based on linear approximation of tensile stress pulse and assuming $\Delta x = c\Delta\tau$.

The expression for the fracture stress in terms of the fracture tensile delay time, $\Delta t\sigma_s^2 = 73.014$ (Equation 2.13 in Table VI) is the result of a linear approximation of the tensile spall stress pulse, while $\Delta t\sigma_s^2 = 63.160$ (Table VI) is the result of a numerical integration of the tensile spall stress pulse. The latter expression correlates well with the experimental values (Figure 2.9).

The expression for the fracture stress in terms of the apparent strain rate, $\sigma_s = 710.0\ \dot{\varepsilon}_a^{1/3}$ (Equation 2.10 in Table VI), is the result of a linear approximation of the net spatial tensile stress and of the assumption $\Delta x = c\Delta\tau$. The expression for the fracture stress in terms of the derived strain rate, $\sigma_s = 616.5\ \dot{\varepsilon}_{sd}^{1/3}$ (Equation 2.15 in Table VI), is the result of a linear approximation of the tensile spall stress pulse. The approximated derived strain rate formula ($\sigma_s = 616.5\ \dot{\varepsilon}_{sd}^{1/3}$) correlates (Figure 2.13) much better with the instantaneous strain rate $\dot{\varepsilon}_s$ than does the apparent strain rate formula ($\sigma_s = 710.0\ \dot{\varepsilon}_a^{1/3}$). The equation $\sigma_s = 587.4\ \dot{\varepsilon}_{sd}^{1/3}$ (Table VI) is the result of a numerical integration of the tensile spall stress pulse and correlates well with the derived strain rate $\dot{\varepsilon}_{sd}$ (Figure 2.13).

One should keep in mind when interpreting Figures 2.9 and 2.13 that different criteria, constant strain energy and constant mechanical energy as identified in Table VI, are employed in the derivations of the various equations.

iv. Cumulative Damage Criterion

Both the tensile mechanical energy and strain energy approaches proposed here with their equivalent criteria are special cases of a more generalized formulation by Tuler and Butcher (1968) and

Gilman and Tuler (1970) for metals.

They propose a cumulative damage model for fracture which assumes that fracture is not instantaneous, but rather that a finite time is required for crack (fracture) initiation. The model is of the form:

$$\int_0^{t_F} f[\sigma(t)]dt = 1 \qquad (2.17)$$

where t_F is fracture time

The phenomenological "energy" criteria correlate with the "cumulative damage" criterion of Equation (2.17) if for Equation (2.16)

$$f[\sigma(t)] = \frac{Ac}{EW}\sigma^2(t) \text{ and } t_F = \Delta t$$

and if for Equations (2.8) and (2.11)

$$f[\sigma(t)] = \frac{Ac}{2EU}\sigma^2(t) \text{ and } t_F = \Delta\tau$$

Thus, the "energy" criteria employ precise physical definitions of function $f[\sigma(t)]$ in the general cumulative damage model of Equation (2.17)

III. DYNAMIC COMPRESSION TESTS WITH THE SPLIT HOPKINSON BAR

A. INTRODUCTION

Experimental limitations prevent the direct measurement of stress and strain in a test specimen subjected to high rates of axial strain. The indirect method introduced by Kolsky (1949) and known as the split Hopkinson bar technique is commonly employed to determine the degree of rate sensitivity or constitutive law of the material at strain rates in the range from 50 to 10^4 in./in./sec. Basically, in this technique (Figure 3.1) a short cylindrical specimen is sandwiched between two long elastic bars in such a way that all center lines are collinear. Strain gages mounted on the bars are used to measure the strains generated by an impulsive force applied to one end of the bar-specimen-bar assembly. Measurements of the loading wave in the first bar, the wave reflected from the specimen, and the transmitted wave in the second bar are sufficient to determine the dynamic stress-strain-strain rate behavior of a material averaged over the length of the specimen when uniaxial stress loading is assumed.

Criticism of Kolsky's analysis has been directed mainly at the neglect of wave propagation and interaction effects in the short specimens used in such experiments and at boundary-interaction effects.

This chapter and Appendix C present the standard analysis and its restrictions as well as the complications which arise when brittle materials such as rocks are being tested. A computer wave propagation analysis is also presented to aid in solving the multiple-reflection problem in the specimen.

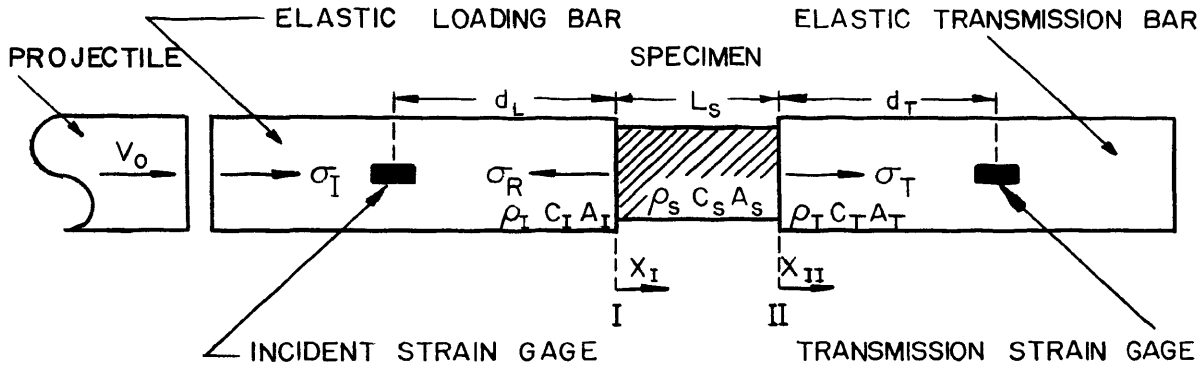

Figure 3.1 - Notation for stress analysis. X_I is displacement of Interface I, X_{II} is displacement of Interface II, σ_I is incident stress, σ_R is reflected stress, σ_T is transmitted stress, d is distance from gage to specimen-bar interface, L_S is specimen length, and ρcA is mechanical impedance

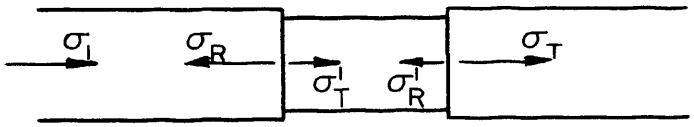

Figure 3.2 - Multiple reflections and interactions in split-bar specimen

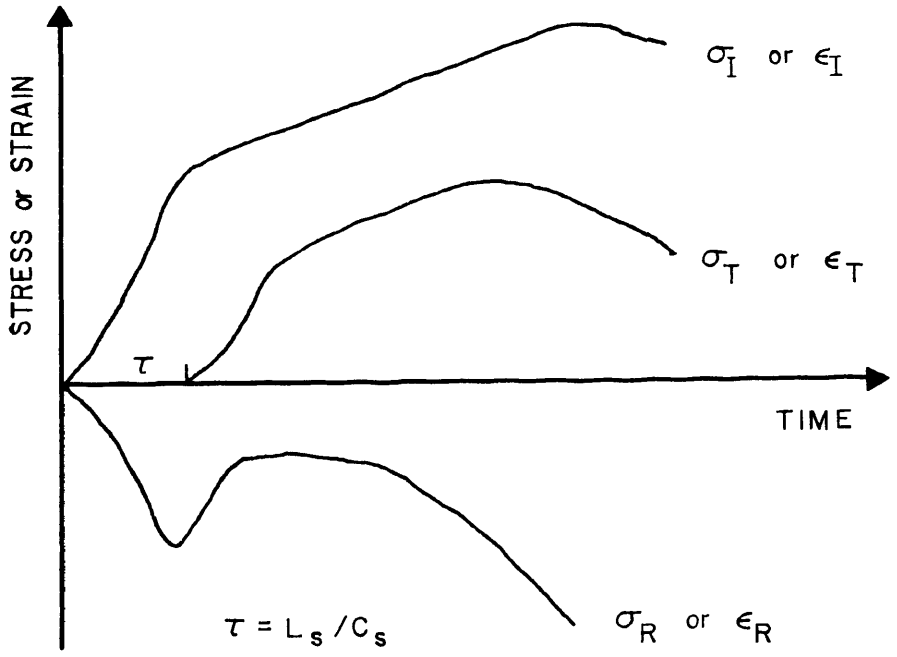

Figure 3.3 - Stress or strain time histories properly phased in time for standard analysis calculations

B. STANDARD ANALYSIS OF THE SPLIT HOPKINSON BAR

The experimental configuration of the split Hopkinson pressure bar as it used for determining dynamic-wave propagation properties and the notations used for analyzing a typical test are shown in Figure 3.1. Upon impact of the projectile, a compressive stress σ_I propagates along the incident (or "loading") bar and is partially reflected at the first interface. The reflected stress σ_R due to the impedance mismatch [Kolsky (1963, p.34)] at Interface I, propagates back into the loading rod. The resulting particle velocity at Interface I produces strain in the specimen as soon as the input wave σ_I enters the first interface.

The fraction of the loading stress which propagates as a transmitted stress σ_T' (Figure 3.2) in turn in partially reflected at Interface II as σ_R' and the stress σ_T is transmitted into the transmission bar. The reflected part of σ_T' at Interface II is reflected back and forth within the specimen losing some of its energy to the incident and transmitter bars at each reflection, until the specimen finally reaches the equilibrium stress distribution and $(\sigma_I+\sigma_R) \rightarrow \sigma_T$.

The strain gages on the loading bar measure the stress $(\sigma_I=E\varepsilon_I)$ wave in the incident pressure bar. Upon partial reflection of the transient at the specimen and after a time delay proportional to the distance of the gages from the first interface d_L, the loading gages record σ_R or $(\sigma_I+\sigma_R)$, depending on whether overlapping of the incident and reflected waves occurs. The set of strain gages on the transmission pressure bar enables the determination of the transmitted compressive wave σ_T (Figure 3.1).

The strain gages mounted on the loading and transmission bar record the strain pulses which are analyzed to obtain a dynamic stress-strain-strain rate curve for the material being tested. The derivations for the one-dimensional standard no-wave analysis method are presented in Appendix C.

The standard method of analysis for the split Hopkinson pressure bar is subject to the following simplifying assumptions:

1. One-dimensional stress in both bars with no radial inertia effect.

2. One-dimensional stress in the specimen with no radial inertia effect.

3. The stress, strain, and strain rate are uniform over the specimen length with no wave propagation and interaction effects. This assumption is equivalent to neglecting the effect of longitudinal inertia in the specimen.

4. Frictionless interfaces.

5. Axial forces and velocities are continuous at the bar-specimen interfaces.

Though average stress, strain, and strain rate data are thus readily obtained, inertia effects are in reality negligible only if a very short specimen is used (Kolsky, 1949). On the other hand, radial frictional effects at the specimen-bar interfaces become more significant as the specimen length is decreased. This friction effect may mask the true dynamic behavior of the material under test since the stress state is not simply uniaxial.

Davies and Hunter (1963) considered corrections for axial, radial and tangential inertia and for the effects of friction. They have

discussed these errors as a function of specimen size for metals, and have shown that, for an optimum specimen size, the length should be nearly the same as the diameter.

The assumptions made in the simple analysis may become very critical and the results may be of questionable validity when brittle materials such as rocks are being tested because the brittle specimen may not reach the stress equilibrium over its length (a few reflections have taken place within the thin wafer) before fracture occurs. In this case the loading wave length to specimen length ratio may be meaningless in its effect on the σ - ε curve of the rock specimen. Another factor influencing the high strain rate technique of rock testing is the statistical nature of flaws and inhomogeneities within the rock which may necessitate a greater specimen size for meaningful results.

The author believes that one answer to the problem of determining true dynamic-wave propagation properties of brittle materials is in the computer wave-simulation approach. This can be done by assuming a constitutive relation for the specimen material, and using a trial and error computer process. For each incident strain pulse the wave propagation and interaction detail may be computed at any point in the specimen, as well as the reflected and transmitted strain pulses in the elastic bars. These computed strain gage outputs are then compared with experimentally measured ones. If they agree, the assumed constitutive law is considered accurate; if not, another model-parameter combination can be made until there is satisfactory agreement between the constructed strain-time curves and the experimental strain gage data. The wave analysis information may then be used, if desired, with the standard method to separate the inertia effect from the strain rate effect in the

averaged (derived) stress-strain-strain rate relation for brittle materials.

The computer simulation method can also be used as a back up to the conventional method of analyzing split bar data. In the latter method one is always confronted with the question as to what part of the derived stress-strain-strain rate curves are valid. By inserting the derived constitutive relation into the wave simulation program, one can verify their validity.

C. FINITE-DIFFERENCE ANALYSIS OF THE SPLIT HOPKINSON BAR

In order to determine the degree to which average stresses, strains, and strain rates (computed with the standard method) approximate actual stresses, strains, and strain rates in the material, a finite-difference computer code for the simulation of the elastic pulse propagation problem in the split Hopkinson pressure bar technique was developed. This simple wave analysis was used to (1) check the finite-differencing technique presented in Appendix A, (2) study bar- specimen-loading pulse parameters that may be important in the standard approach and so aid in the designing and planning of laboratory experiments, and in the interpretation of results, (3) perform an elastic wave analysis verification for experimental data without neglecting wave effects.

The computer approach outlined in the last part of Section B was applied to an assumed linearly-elastic specimen to determine how the derived σ_{avg}-ε_{avg}-$\dot{\varepsilon}_{avg}$ curves depart from the assumed rate insensitive behavior for various combinations of the bar-specimen-loading pulse parameters. Also, computed numerical gage data may be compared to experimental numerical gage data to verify if the materials tested have

a linear elastic-strain rate insensitive constitutive law.

1. Computer Simulation for a Sine Loading Wave

Kolsky's (1949) technique was simulated in the computer for a sine incident strain pulse propagating into the experimental assembly. The specimen and bar materials, and loading pulse parameters selected (Table VII) were identical to those used by Wu and Hustrulid (1971).

The loading strain wave, ε_I, was defined as

$$\varepsilon_I = A \sin\frac{\pi}{\lambda} c_I t, \text{ for } 0 \leq t \leq \lambda/c_I \tag{3.1}$$

where

A is the maximum amplitude

λ is the wave length.

TABLE VII - DATA USED IN THE COMPUTER SIMULATION

	Steel bars	Specimen
Specific weight, lb./in.^{3}	0.2828	0.0966
Wave speed, 10^5 in./sec.	1.9558	2.0976
Young's modulus, 10^6 psi	28	11
Diameter, in.	1.5	1.5
Length, in.	84	1,2,5
Space increment, in.	0.233	0.250
Amplitude, A, 10^{-6} in./in.	995	
Wave length, λ, in.	10	

2. Simulation Results

Theoretical split-bar test data were generated for a sine wave input [Equation (3.1)] into the split-bar finite-difference code. This computer simulation provided the true shapes of the reflected and transmitted pulses. These were then used as if they were experimental data to be reduced with the standard method of analysis to obtain "derived" values of stress, strain and strain rate as a function of time. The true values of stress and strain at the finite-difference mesh points were averaged along the specimen and compared with the derived values. It was found that the specimen length may influence the slope and shape of the stress-strain curve for a given loading pulse duration and intensity (see Figure 3.4). It was interesting to note, however, that the derived strain (and strain rate) - time curves agreed well with curves representing the averages of mesh point values along the specimen. Thus, the derived curves of ε_{avg} and $\dot{\varepsilon}_{avg}$ vs. time reflect, contrary to Kumar's assumption (1968), true average dynamic effects no matter what specimen size is used. It was apparent that the distributions of stress, strain, and rate of strain were in general, not uniform along the length of the specimen. As expected, the degree of non-uniformity is most severe during the earlier portions of the loading history.

Similarly, errors in the delay time τ (Figure 3.3) affected the slope and shape of the derived stress and strain-time curves as well as the stress-strain curve (see Figure 3.5).

An overstress caused by the axial inertia effect was observed in the early part of the loading cycle in the one-dimensional wave analysis. Therefore, data collected during the first few microseconds in the Hopkinson split-bar type tests should be ignored. The initial distortion

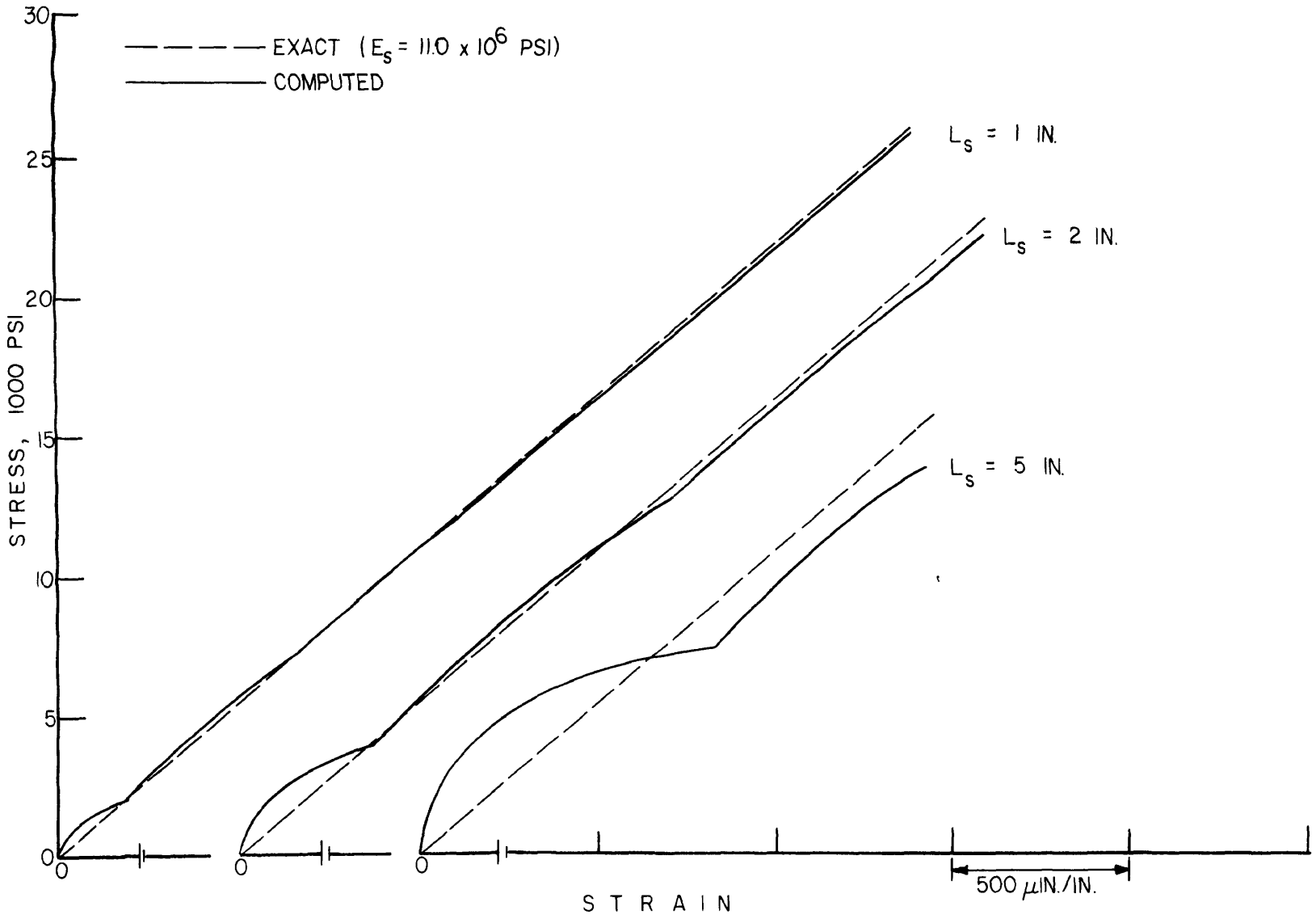

Figure 3.4 - Comparison of the derived stress-strain curves for simulated test conditions in Table VII. Data points were taken at 1.19 μ sec intervals

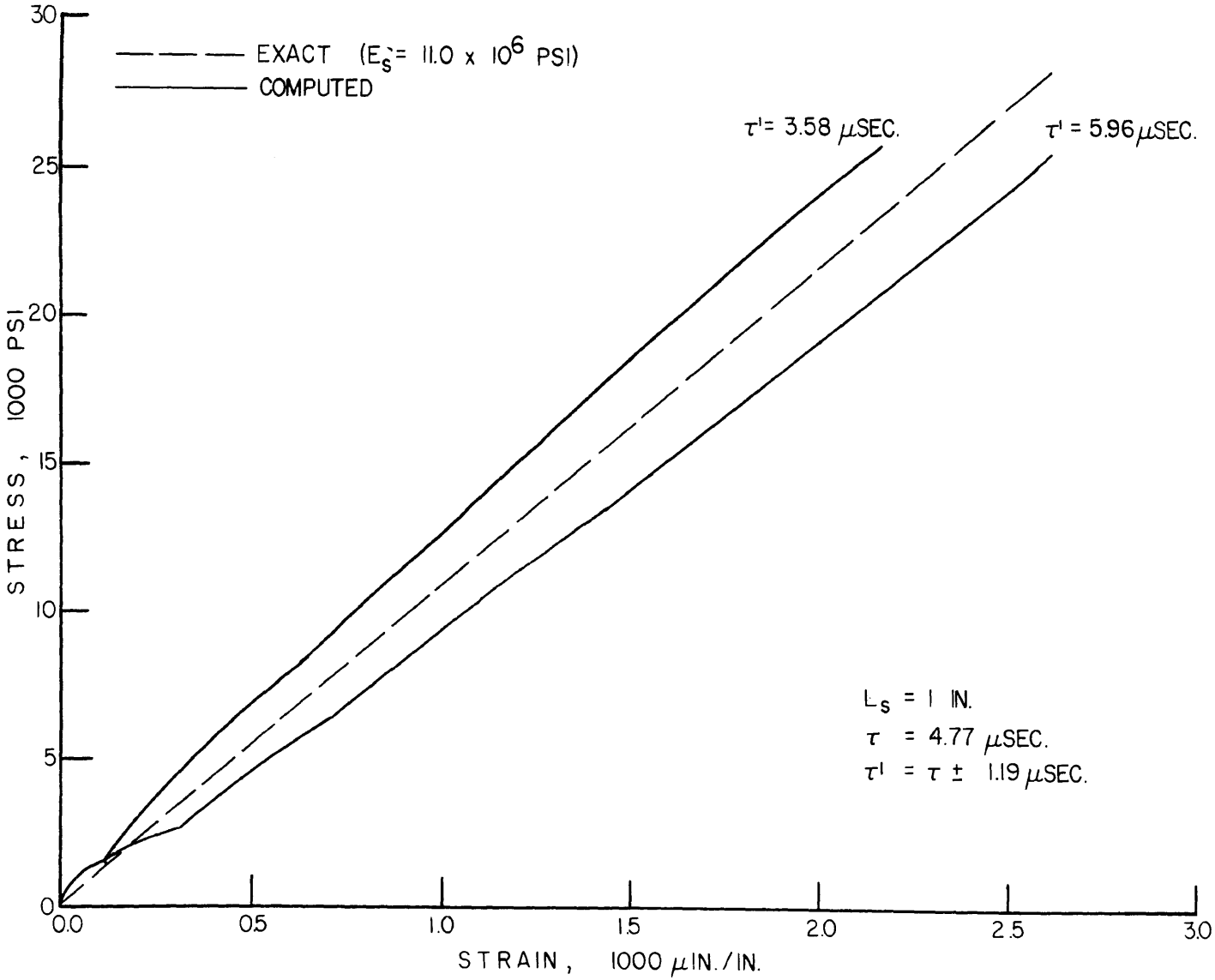

Figure 3.5 - Effect of an error of one time interval (1.19 μ sec) in the delay time τ on the derived stress-strain curves. Simulated test conditions are listed in Table VII

of the derived stress-strain curve may be sufficient to preclude the determination of the elastic modulus and even the yield stress for elastic-plastic materials. The common criterion used for selecting values from the derived stress, strain and strain-rate curves that approach those actually in the sample, is the stress difference at the specimen ends. It was observed that a stress difference of over 10 percent of the first interface stress still resulted in a true stress-strain curve (i.e., elastic with assumed modulus).

From the computer simulation it was noted that increased derived strain rates were obtained by reducing the specimen length. It was also found that when the specimen length increased the derived stress levels in the vicinity of the maximum stress departed from true (assumed) elastic behavior, again because of axial inertia effects (see Figure 3.4). Therefore, the standard method of analysis may introduce important errors in the maximum derived stress as the specimen length increases. Green and Perkins (1968) in studying the effect of specimen size in dynamic loading concluded that the apparent fracture stress decreases as specimen length increases, the diameter remaining constant. They agreed with Mogi (1965) and Grosvenor (1963) in that such a decrease in the strength is due to a decrease in the end effects as the specimen length increases. From the above analysis the author believes that this explanation may be ambiguous because in the split -bar test for brittle materials the effect of the stress gradient on the strength may be severe. Here the effects of size and stress gradient on the strength need to be separated. Although little has been done in this area, it is an important consideration in the split-bar test. The presence of stress gradient, flaws and inhomogeneities in the material, and frictional end

effects are known to cause an apparent size effect in the strength and deformation behavior under static loading and would be expected to do likewise for dynamic loading.

A wave analysis of split-bar data may offer the possibility of studying the effects of stress gradient on rock failure under dynamic compressive conditions, a factor which has not yet been examined either experimentally or theoretically. This refinement may allow the determination of a time dependence criterion for prediction of true dynamic compressive strength at high strain rate and under steep stress gradients.

D. EQUIPMENT, INSTRUMENTATION AND EXPERIMENTAL PROCEDURE

The high strain rate experiments were done in a large diameter split Hopkinson bar apparatus similar in design to that used by Kolsky (1949) and others.

The equipment, instrumentation, and experimental procedure are similar to those used for the long bar spallation tests. Bai (1970) gives a complete description of the split Hopkinson pressure bar device used in this investigation. The schematic of the experimental arrangement and instrumentation is shown in Figure 3.6. The loading and transmission bars were both 7 ft. long and 1.497 in. in diameter with mirror finish ends, and made from 7075-T6 aluminum alloy (ρc = 53.31 lb-sec/in.^{3}). The strain gages were mounted at the midpoint of each elastic bar. For each test the rock specimen was placed in firm contact between the two axially aligned bars to improve the wave transmission across the interfaces.

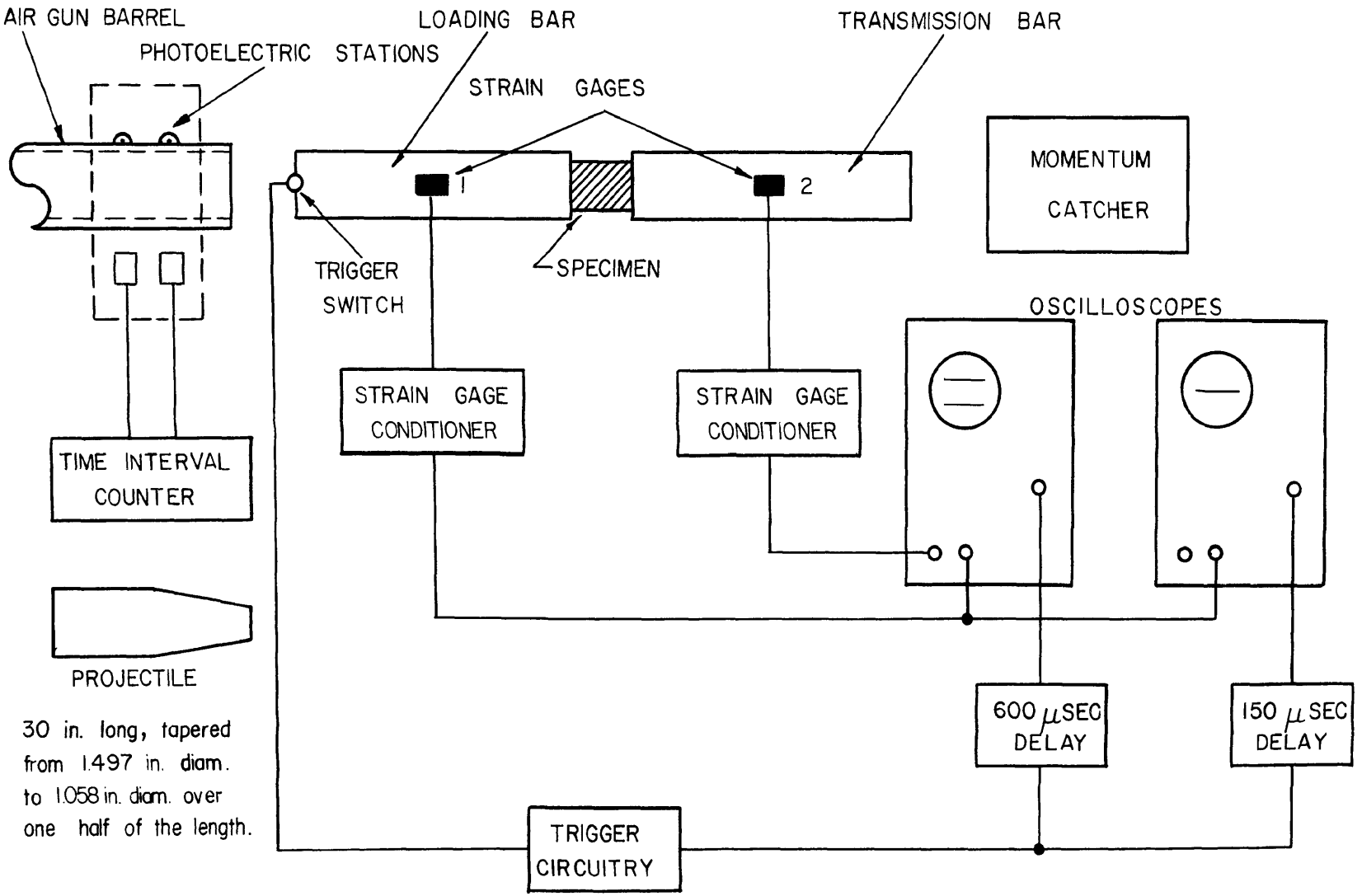

Figure 3.6 - Schematic of instrumentation for split Hopkinson bar

A tapered aluminum projectile (made from the same material as the bars), 3 ft. long, impacted the input bar to generate the incident stress pulse. The magnitude of the loading pulse depends on the projectile impact velocity, length, and shape. The impact also triggered the oscilloscopes which after a suitable time delay recorded and stored strain records at the gage locations as a function of time (a typical result is shown in Figure 3.7). The oscilloscope screens were photographed with a Polaroid camera and these records were projected onto graph paper for machine digitizing and analysis.

A momentum trap was placed a short distance from the free end of the transmission bar to absorb the assembly momentum. This prevented tearing the strain gage leads from the bars during the later rigid body motion of the bars.

The bar wave velocity of each pressure bar was obtained by measuring the transient time in a single-bar experiment. Its value was 2.040×10^5 in./sec. Young's modulus was then calculated from the relation $c^2 = E/\rho$ to give $E = 10.904 \times 10^6$ psi.

Pulses were recorded at the two gage stations with no specimen in the pressure bar set up to compensate for the joint effect always present despite the mirror finish on the ends of the bars and great care in alignment. In order to decrease frictional or end effects, an appropriate specimen geometry of length to diameter (see Table VIII) was used and the flat surfaces of the specimens were lubricated with a thin layer of high-vacuum grease. The lubrication minimized the interface shearing stresses present when dissimilar materials expand radially. The strain gage transducers were calibrated by placing a calibrating shunt resistance across one of the gages as was done in the long bar experiment.

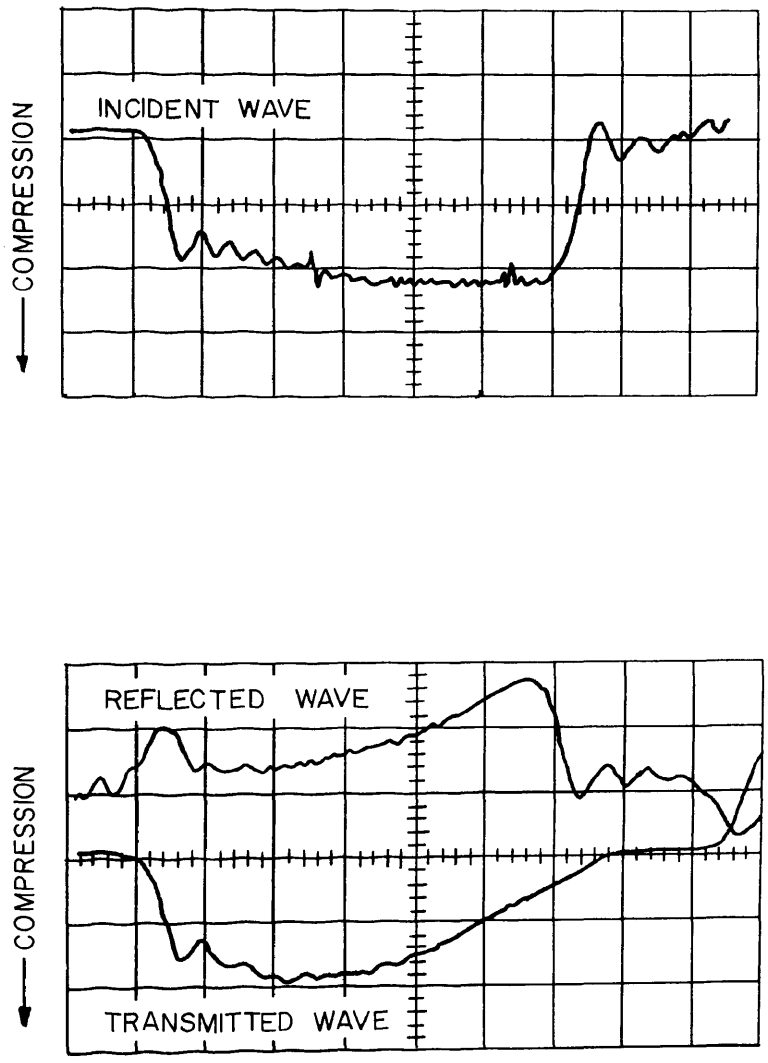

HORIZONTAL SCALE: 50 μSEC. PER MAJOR DIVISION

VERTICAL SCALE: 314.46 μIN./IN. PER MAJOR DIVISION

Figure 3.7 - Typical oscilloscope traces of incident, reflected and transmitted strain pulses

TABLE VIII- COMPRESSIVE STRESS-STRAIN-STRAIN RATE DATA FOR CONCRETE

Specimen No.	Specimen Length (Spec. diam=1.471") in.	Projectile Velocity in./sec	Secant* Modulus 10^6psi	Ultimate Conditions Stress psi	Ultimate Conditions Strain 10^{-6}in./in.	Ultimate Conditions Strain Rate Sec^{-1}
J-1-2	1.478	377	1.40	6836	4863	39
H-1-3	1.547	323	1.42	6480	4538	37
J-1-B	1.487	373	1.66	7399	4436	33
J-1-3†	1.008	368	1.83	6907	3763	32
I-4-1	1.525	320	2.05	7030	3414	14

*Dynamic secant moduli from zero stress to ultimate fracture stress.

†Seven reflections in the specimen before fracture.

E. ANALYSIS AND TEST RESULTS

Five short cylindrical specimens of concrete, with length approximately equal to the diameter, were tested in the compressional split bar assembly, and the experimental strain gages results analyzed with the conventional (standard) method to determine the dynamic σ-ε-$\dot{\varepsilon}$ curves. The specimen ends were ground smooth and parallel to ± .002 in. The governing criteria for specimen size were axial and radial inertia errors associated with the analysis and the statistical variation of material properties. A tapered projectile (see Figure 3.6) was used to produce a slowly increasing incident stress pulse so that the brittle failure would occur during a period of relative stress equilibrium in the specimen. Very high initial strain rates should be avoided when one is testing brittle materials since failure may occur so early in the loading cycle that meaningful results cannot be obtained. The strain-time information from the gages was processed as explained in Appendix C. The values of the average stress, strain, strain rate, and stress difference between the specimen ends as a function of time were computed. These input and output data together with the stress-strain relationship were plotted for a typical specimen in Figures 3.8 to 3.11 . Similar sets of curves for the remaining specimens are included in Appendix D.

Typical strain gage records after compensation for the joint effect are shown in Figure 3.8 . It is seen from these curves that the incident compressive stress has a gradual increase to its maximum. This was obtained with the tapered projectile and is necessary to avoid premature brittle fracture when there is a significant stress difference between the specimen ends. The shape of the slowly increasing stress region of the loading pulse can be controlled by properly tapering the projectile.

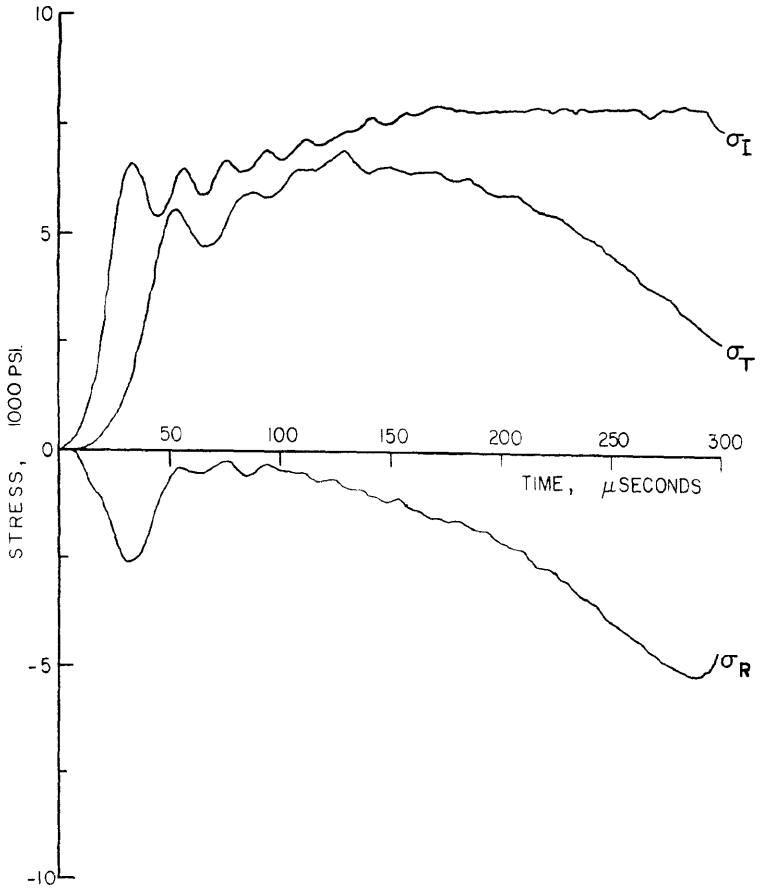

Figure 3.8 - Incident, reflected, and transmitted stress pulses for specimen I-4-1

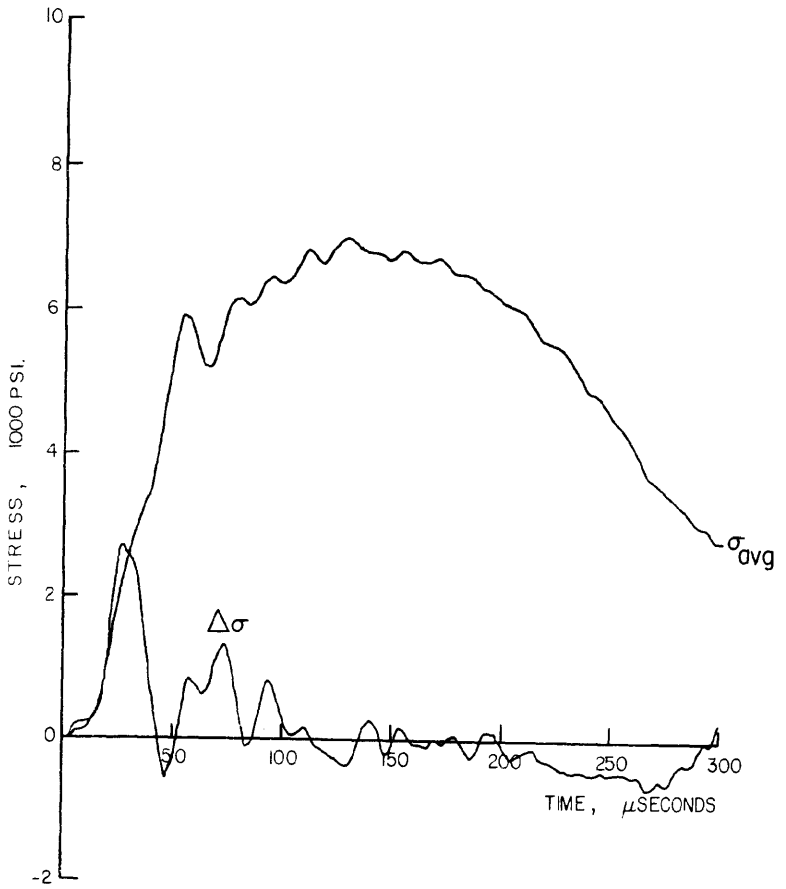

Figure 39 - Average stress and stress difference vs. time for specimen I-4-1

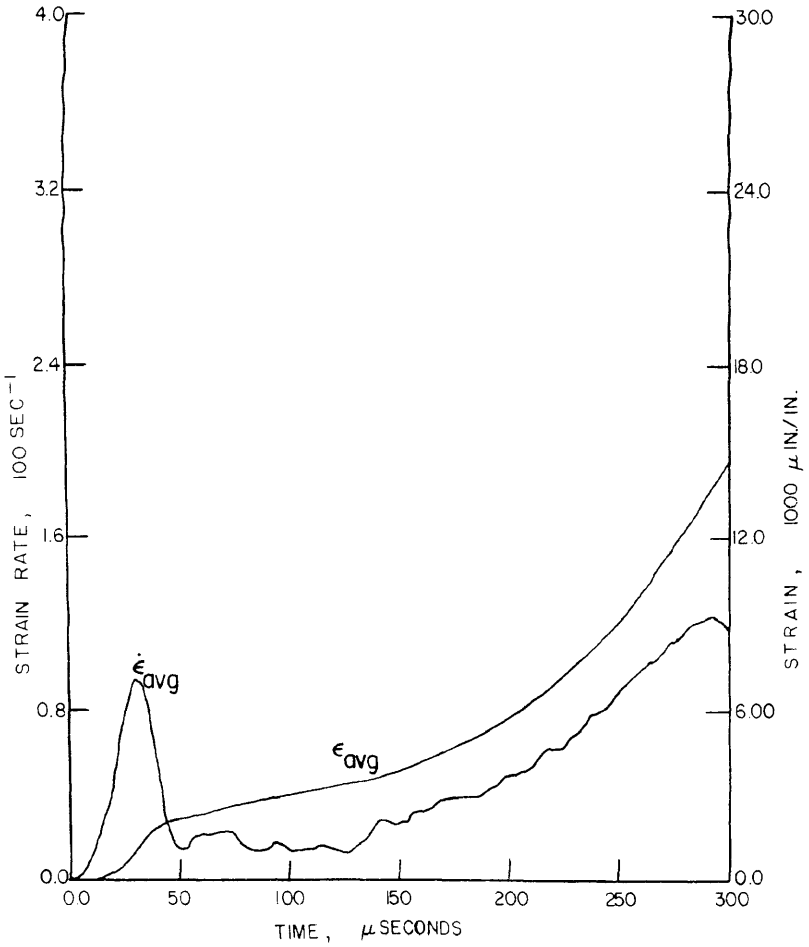

Figure 3.10 - Average strain and strain rate vs. time for specimen I-4-1

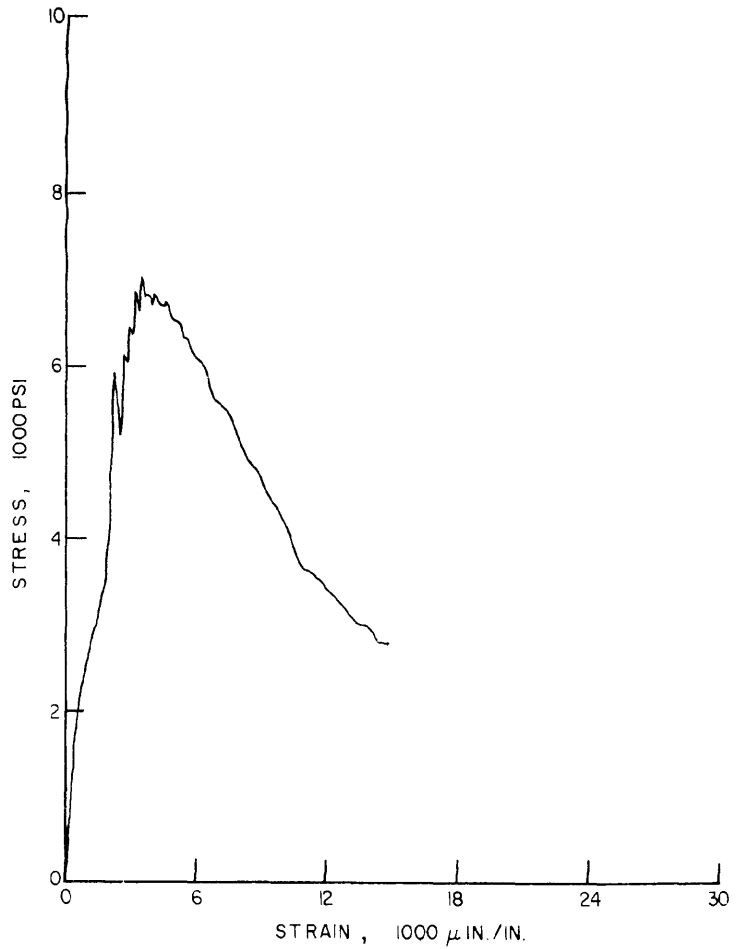

Figure 3.11 - Average stress vs. average strain for specimen I-4-1

The rapid increase in the reflected stress σ_R and the decrease in the transmitted pulse σ_T, at later loading times, are an indication of a reduction of the effective mechanical impedance ($\rho_s c_s A_s$) of the specimen as a result of crack growth. This will reduce in turn the load-bearing capacity ability of concrete in the post-failure region as will be discussed later.

The dynamic stress-strain-strain rate curve of Figure 3.11 was obtained by plotting stress versus strain at corresponding times from Figures 3.9 and 3.10.

1. Dynamic Deformation and Failure

Reasonable dynamic σ-ε-$\dot{\varepsilon}$ curves up to failure were obtained directly from the computed σ-ε-$\dot{\varepsilon}$ plots (see Figure 3.11 and Appendix D) in those regions where the stress difference was less than 10 percent. These close-to-equilibrium dynamic loading curves at various strain rates are shown in Figure 3.12. The average strain rate is stated for each section of the stress-strain curve in Figure 3.12 along with the maximum variations. These variations were at most 28 percent of the average value for the regions plotted. The loading curves in Figure 3.12 should not be considered strictly as constant strain rates, but rather reasonable approximations.

The stress-strain curves at desired constant strain rates are usually obtained by first plotting the instantaneous strain rates at a given strain versus stress for a group of tests and then cross plotting with a family of so-obtained constant strain curves. This refinement was not attempted here due to the limited number of tests and the relatively large amount of scatter in the results.

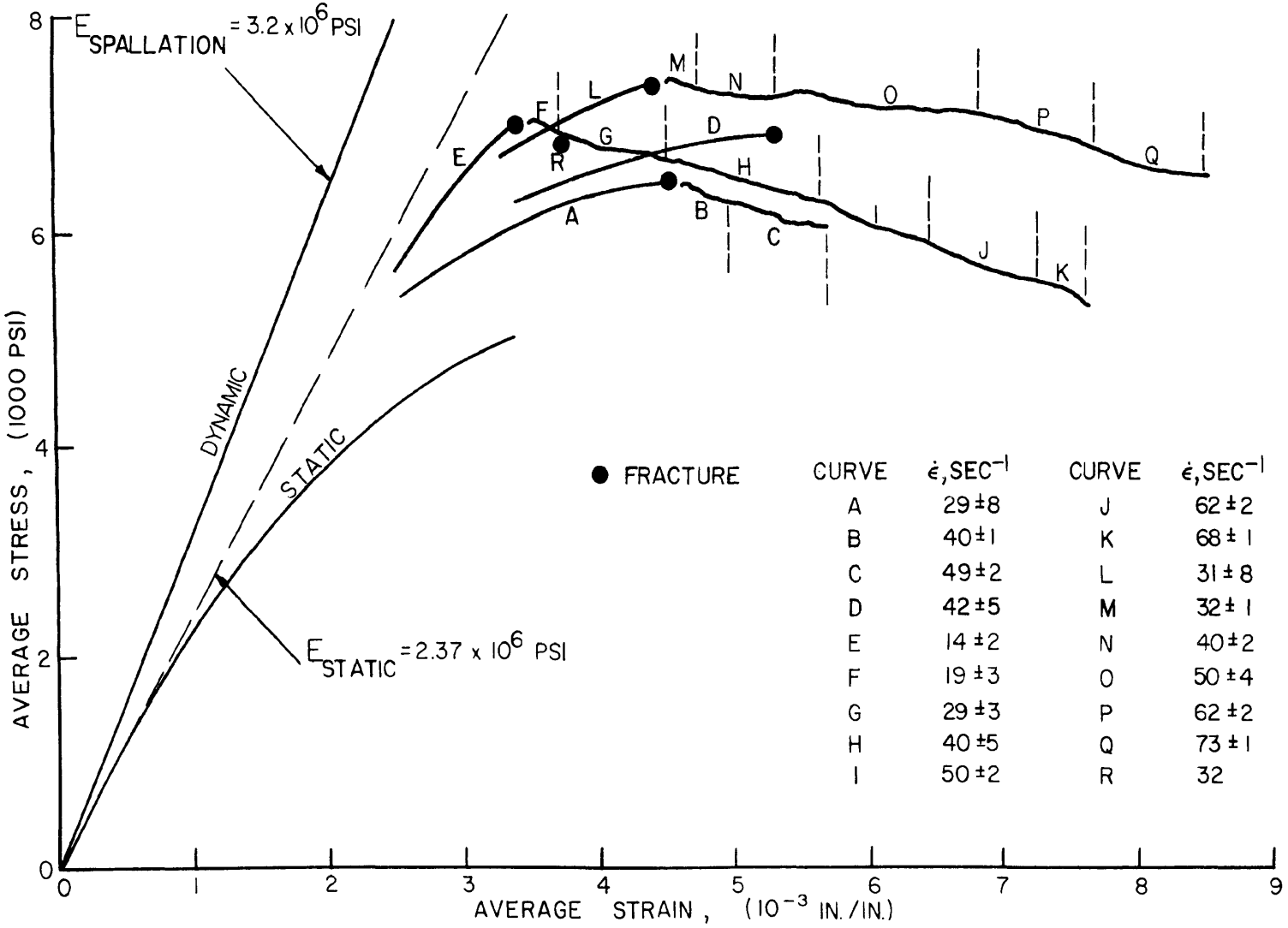

CURVE	$\dot{\epsilon}$, SEC^{-1}	CURVE	$\dot{\epsilon}$, SEC^{-1}
A	29±8	J	62±2
B	40±1	K	68±1
C	49±2	L	31±8
D	42±5	M	32±1
E	14±2	N	40±2
F	19±3	O	50±4
G	29±3	P	62±2
H	40±5	Q	73±1
I	50±2	R	32

Figure 3.12 - Experimental rate-sensitive stress-strain curves for concrete under uniaxial compression at different strain rates

Unconfined compressive stress-strain-strain rate results for the concrete summarized in Table VIII are values under ultimate conditions, defined at the time when stress reaches its maximum value. Table VIII and Figure 3.12 indicate that the failure strain in the concrete increases with strain rate, which is consistent with the results of Atchley and Furr (1967). It is also shown that the dynamic compressive failure strain (3763 - 4863 μ in./in.) for the higher strain rates (32 - 39 sec^{-1}) were greater than the corresponding static value (3450 μ in./in.), which is in agreement with Watstein's results (1953).

The failure stress is relatively constant and shows relatively little sensitivity at the strain rate values employed, which was also reported by Green and Perkins (1968, p. 46), and Atchley and Furr (1967). The dynamic to static compressive strength ratio varied from 1.42 to 1.46.

A secant modulus can be defined as the slope of the straight line containing the zero loading point and the fracture point at which reasonable equilibrium has been established. It is shown from Table VIII and Figure 3.12 that the secant modulus decreases, with increasing instantaneous strain rate.

The moduli determined from both long bar velocity measurements was significantly greater than its corresponding static value (Figure 3.12). The ratio of dynamic to static Young's moduli was 1.35. Brittle failure occurred at such low strain levels that the specimen was not in a state of uniform stress in the early part of the dynamic experiments. Therefore, no valid moduli could be calculated from the σ-ε-$\dot{\varepsilon}$ curves derived by the conventional method.

Figure 3.12 and Table VIII indicate that the strength is not a function of strain rates in the range 14 - 39 sec^{-1}. The strength de-

pendence on strain rate at very high rates (10^2 - 10^4 sec^{-1}) reported by Green and Perkins (1968), and Kumar (1968) may be due to early failure (less than five wave reflections within the specimen) which alters the state of uniaxial stress along the specimen.

Rummel and Fairhurst (1970, p. 197) suggested that many rocks deform in a nonlinear manner near failure when loaded at moderately slow strain rates. In a similar way, Figure 3.12 indicates that a regime of slow damage (or crack growth) may precede the onset of unstable failure propagation under dynamic loading in concrete. Further studies of the near-failure region of dynamic deformation are necessary for a better understanding of the processes involved.

Strain rates can be held constant for lower rate testing as with stiff and servo-controlled testing machines. However, constant strain rates are not achieved in the higher-rate split-bar testing. In the reported controlled rock testing the strain rate has thus played a role as a parameter, and not necessarily as an independent variable, although it has been treated as such. The strain-rate history or variable strain-rate loadings may be important in the deformation and failure of rocks and rock-like materials.

2. Post-Failure Behavior

For static loads up to failure the rock is in stable equilibrium with the stresses applied to it; difficulties in measuring stresses and strains arise at or near failure when the equilibrium breaks down resulting in a violent and uncontrolled release of energy. With force as the independent variable the usual constant rate of loading used in conventional compressional rock testing implies that the force be increased to the specimen's maximum loading-bearing capacity (compressive "strength")

with the failure generally being catastrophic in nature (Bieniawski, et al., 1970). It is therefore of great importance to study the behavior of failed rock, which may contribute significantly to an understanding of rock stability problems and lead to the development of better methods of controlling the violent failure of rock structures.

Several investigators (Wawersik, 1968; Crouch, 1971; Rummel and Fairhurst, 1970; Hudson, et al., 1971; among others) have recently studied experimentally the mechanical behavior of disintegrating rock by considering the displacement as the independent variable. Two methods have been used to control the excess energy release during failure: a stiff testing machine and a servo-controlled testing system. When the load is thus controlled during the loading and unloading portion of the curve it is found that explosive failure of rock specimens is not necessarily an intrinsic rock property but is often due to a rapid release of strain energy stored within the testing machine. These tests, where a fixed displacement rate has been applied to the rock specimen, have demonstrated that rocks do retain some strength after the ultimate strength of the rock has been reached.

The literature on controlled rock failure is abundant for very low constant strain rate loading; however, no research has been reported in the high strain rate range. The author has used the split Hopkinson bar technique and its simple method analysis, to show the potential of this technique in allowing reasonable unloading post-failure dynamic curves. As was shown in Appendix C, the simple analysis allows one to determine the displacements of the specimen ends as a function of time. These displacements can then be considered as the independent variables. By controlling the shape, intensity, and duration of the incident wave

passing through the bar-specimen-bar assembly one may devise a dynamic-controlled testing system which will produce any desired unloading path. The use of different projectile shapes and sizes will aid the control of the incident wave. There is no reported work on the dynamic post-failure of rock and rock-like materials. The author herein presents some of his findings related to the dynamic wave propagation post-failure of concrete.

Figure 3.12 also shows the σ-ε-$\dot{\varepsilon}$ curves for the failed concrete. It is interesting to see the great increase in strain (about 100 percent) with a decrease in stress during unloading (about 20 percent) at different strain rates. This reduction in load-bearing capacity ability of concrete in a post-failure region is the result of crack growth which also causes a reduction of the effective mechanical impedance ($\rho_s c_s A_s$) of the specimen. The unloading paths of the dynamic computed curves shown in Appendix D were obtained when the data was processed with no regard to specimen end stress difference; that is, high stress gradients were present within the specimen during some portions of the unloading cycle.

IV. SUMMARY, CONCLUSIONS, AND RECOMMENDATIONS

A. LONG BAR DEFORMATION AND FRACTURE BY SPALLATION

The process of spallation and its separation into two phenomena of stress wave propagation and interaction in plain concrete (a rock-like material) and fracture under dynamic loading is described in this dissertation.

Fundamental to the study of spallation phenomena was the determination of stress, strain, and strain-rate history at the spall plane, and the stress distribution along the bar at time of fracture initiation. As the stress condition in the interior of the material cannot be measured directly, it was inferred from measurements of surface strains on the concrete bars and solution of the stress wave propagation problem. It was necessary as a prelude to the solution of the marching problem, to know or assume the dynamic properties of the concrete and its dynamic constitutive relation. A one-dimensional finite-difference wave-propagation computer code was used to calculate the stress distribution along the bar at any desired time and the stress history at any location resulting from an axial projectile impact on one end of the bar.

The strain gage signals were used to substantiate the assumed elastic constitutive relation and to determine the critical fracture time at which tensile fracture begins. The measured spall coordinate and the critical fracture time were input to the computer code to calculate the stress, strain, and strain rate-time histories at spall plane up to the time of fracture and the stresses along the bar at the instant of fracture. These quantities were then used in the development of different types of time-dependent dynamic fracture models.

A general criteria based on the concept of cumulative damage was proposed to explain the time-dependent dynamic criteria for fracture by spallation in concrete bars.

The principal conclusions resulting from this investigation on concrete are:

1. The finite-difference technique is accurate and reliable when applied in the numerical solution of the one-dimensional elastic stress wave propagation problem in long cylindrical bars. This dissertation shows how a judicious combination of computer and experimental stress methods permits more accurate descriptions of dynamic loading effects on materials.

2. The simple elastic wave analysis explained the material behavior reasonably well over the dynamic-wave stress loading conditions employed. Attenuation and dispersion were found to be negligible in the long bars.

3. The dynamic Young's modulus was significantly greater than its corresponding static value. The ratio of dynamic to static Young's moduli was 1.35.

4. The dynamic compressive strength deduced from the peak compressive stress propagating in the long concrete bars was linearly dependent on projectile velocity. However, the extent of the comminution at the impacted end was not dependent on the projectile velocity since the crushed zone length varied greatly, even for approximately the same nozzle energy of the spherical-nosed cylindrical projectiles. The dynamic to static compressive strength ratio varied from 0.50 to 0.80 for the particular striker and velocities used. Stresses significantly higher than these could not be induced into the intact bar by increasing

the impact velocity. The higher energy of the striker would go mostly into additional comminution rather than stress wave energy into the intact portion of the bar.

5. The instantaneous critical spall stress (or strain) at which tensile fracture begins increased with increasing instantaneous fracture spall strain rate, and decreased with increasing tensile stress rise time to fracture. This was an indication of a time dependence of the spall strength for concrete. A similar time dependence for dynamic fracture by spallation was also observed in terms of the space-tensile stress variation at fracture.

6. For the range of strain rates investigated (7 to 33 sec^{-1}) the dynamic tensile strength was 3.5 to 5.0 times its static value. An approximation for the dynamic tensile strength was 1200 to 1800 times the static Young's modulus.

7. At fracture the derived strain rate $\varepsilon_s/\Delta t$ is a better approximation to the instantaneous strain rate at time of fracture $\dot{\varepsilon}_s$ than is the apparent strain rate $\varepsilon_s/\Delta x/c$.

8. The tensile fracture stress increased in an approximately linear manner with increasing peak incident compressive stress. Since it was observed that the spall strength was also a function of rate of loading, the precompression explanation of the increased tensile strength is not complete.

9. The critical normal fracture strain energy and mechanical energy criteria are proposed to explain the spatial and time dependence explanation of spallation in concrete. The critical tensile fracture strain energy was defined as the energy stored in the tensile-stressed part of

the bar between the impact end and the spall at the time of fracture initiation. The energy value was found to be 1.27 ± 0.38 in.-lbs. for concrete bars 1.47 in. diameter subjected to instantaneous strain rates varying from 7 to 33 sec^{-1}. The use of minimum strength values was not required for the constancy of the strain energy.

The critical tensile fracture mechanical energy was more nearly constant than the corresponding strain energy and the values of the former were generally higher. This critical mechanical energy was defined as the energy passing through the spall plane up to the time of fracture initiation and was found to have the value 1.68 ± 0.18 in.-lbs. at the time of fracture, again for 1.47 in. diameter bars. Care must be taken when extrapolating the results of this dissertation to other size bars because the area A is a scale factor.

10. Both the tensile mechanical energy and strain energy criteria were shown to be equivalent to the tensile stress gradient and rate dependent criteria under the usual assumption of linearity in the net stress pulse. It was also shown that the energy criteria were special cases of a more generalized cumulative damage model of the form:

$$\int_0^{Z_F} f[\sigma(Z)]dZ = 1$$

where

Z is the space or time coordinate

Z_F is the value of Z at fracture initiation

$f[\sigma(Z)]$ is a second order stress damage function in terms of the physical material properties (E and c), cross-sectional area A, and the constant energy transferred or stored (W or U). The quantities A and c affect $f[\sigma(Z)]$ proportionately and E and W (or U) inversely. The mechanical energy concept has a more reasonable physical basis (energy transfer from mechanical energy to new surface energy at spall plane) for incorporation into the cumulative damage criterion.

11. The empirical spallation energy criteria for concrete and their equivalent expressions are summarized in Table VI at the end of Chapter II.

The expression for the fracture strain in terms of the apparent strain rate $\varepsilon_s = 2.209 \times 10^{-4} \dot{\varepsilon}_a^{1/3}$ (Equation 3.10a) is similar to the one reported by Birkimer (1968) $\varepsilon_s = 2.060 \times 10^{-4} \dot{\varepsilon}_a^{1/3}$ for another concrete. This indicates that perhaps there is a constant representing the spall resistance of the concrete materials, which will depend on the strain energy, Young's modulus, wave velocity, and cross-sectional area.

12. The cumulative damage energy concept may be applied to spallation in rock and rock-like materials loaded in uniaxial stress (bar geometry) or uniaxial strain (plate geometry).

In view of the great potential of the application of the findings obtained from this dissertation, the following recommendations are made:

a. Investigate the application of the cumulative damage energy criterion for several rocks impacted in uniaxial stress, and correlate the results with the static physical properties to predict spallation behavior of unknown rocks.

b. Continue investigating the dynamic behavior of concretes with different material strengths, and correlate the results to find a possible

spall resistance constant. A correlation with the static mechanical properties of the concrete may be found to predict spallation behavior for concretes (W, U, etc.) subjected to bar geometry loading.

c. Study the possible application of the cumulative damage energy criterion to the spallation of rock and rock-like materials for uniaxial strain loading (plate geometry) to determine if the state of stress affects the general spallation criterion proposed for uniaxial stress loading.

B. COMPRESSIONAL SPLIT HOPKINSON BAR TESTING

A critical study of the principles and conventional analysis of the compressional split Hopkinson bar technique for rock and rock-like material testing has been presented. The restrictions and complications involved in split-bar testing of brittle materials were pointed out in this dissertation (pp. 56-57). A computer code to reduce data generated in the technique has been developed, using the conventional analysis. Experimental strain-time data can be inserted in the code to compute average stress, strain, and strain rate as a function of time and the stress difference-time history at specimen ends. This program also allowed plotting of the stress and stress difference-time, strain-time, strain rate time, and the stress-strain relationships.

The degree to which average stresses, strain, and strain rates approximate actual stresses, strains, and strain rates in the material when the standard method of analysis has been used for processing experimental data was investigated. A finite-difference computer code for the simulation of the elastic wave propagation problem in the split Hopkinson bar technique was developed. Theoretical split-bar test data were generated for a sine wave input into the split-bar finite-difference

code. The computer simulation provided the true shapes of the reflected and transmitted pulses. These were then used as if they were experimental data to be reduced with the standard method of analysis to obtain "derived" values of stress, strain, and strain rate as a function of time. The simulated values of stress and strain averaged along the specimen at the mesh points were also determined and compared with the derived values.

Split-bar experiments were performed in a large diameter split Hopkinson bar apparatus for concrete specimens. The experimental strain gages results were analyzed with the conventional method to determine dynamic deformation, failure, and post-failure behavior.

On the basis of discussions and results from the conventional and elastic wave simulation analyses, and from the split-bar experiments on concrete, the following conclusions are drawn:

1. The high-strain-rate split Hopkinson pressure bar technique used to obtain the dynamic-wave propagation properties of brittle materials such as rocks requires careful wave analysis in the bar and specimen for accurate interpretation of experimental data. The assumptions made in the standard analysis may become very critical and the results may be of questionable validity because the brittle specimen may not reach the stress equilibrium over its length (a few reflections have taken place within the thin wafer) before brittle failure occurs. In this case the ratio of loading wave length to specimen length may be meaningless in its effect on the dynamic stress-strain curve of the rock specimen. Another factor controlling the high-strain-rate technique of rock testing is the statistical distribution of flaws and inhomogeneities which may call for a greater specimen size.

The author believes that the true dynamic-wave propagation properties of brittle materials could best be determined by a computer wave simulation approach.

2. From the computer simulation for a sine incident strain pulse propagating into the experimental assembly it was found that:

a. Specimen length may have a significant effect on the slope and shape of the stress-strain curve for a given loading pulse duration and intensity. However, the derived strain and strain rate-time curves agreed well with curves representing the averages of mesh point values along the specimen. Thus, the derived strains and strain rates signify true average dynamic effects no matter what specimen size is used.

b. The distributions of stress, strain, and rate of strain in the test specimen are, in general, not uniform. As expected, the magnitude of this non-uniformity is most severe during the earlier portions of the loading cycle.

c. Errors in the delay time caused significant errors in the slope and shape of the derived stress and strain-time curves as well as the stress-strain curve.

d. A stress difference between specimen ends of over 10 percent still resulted in an accurate stress-strain curve (i.e., elastic with assumed modulus).

e. For the same input pulse, increased derived strain rates are obtained when specimen length is reduced.

f. When the specimen length is increased, the derived stress levels in the vicinity of the maximum stress decreased and departed from true (assumed) elastic behavior because of axial inertia effects. This fac-

tor should be considered in the explanation of the decrease in strength with increasing specimen length.

g. The end-effects explanation of the decrease in strength as the specimen length increases may be ambiguous for brittle materials because in the split-bar test the effect of the stress gradient on the strength may be severe. The presence of stress gradient, flaws and inhomogeneities in the material, and frictional end effects generally cause an apparent size effect in the strength and deformation behavior.

3. The experimental results on concrete show a sensitivity of failure strain to strain rate. For the higher rates the strain increases.

4. The dynamic compressive failure strain (3763 - 4863 μ in./in.) for the higher strain rates (32 - 39 sec^{-1}) were greater than the corresponding static value (3450 μ in./in.).

5. The failure stress is relatively constant and shows relatively little sensitivity at the strain rates values employed (14 to 39 sec^{-1}). The dynamic to static compressive strength ratio varied from 1.42 to 1.46.

6. A secant modulus, defined as the slope of the straight line containing the zero loading point and the maximum stress at which reasonable equilibrium has been reached, decreases with increasing instantaneous strain rate at fracture.

7. Brittle failure occurred at such a low strain level that the specimen was not in a state of uniform stress in the earlier part of the dynamic experiments. Therefore, no valid moduli could be calculated from the σ-ε-$\dot{\varepsilon}$ curves derived by the conventional method.

8. The reported data from other investigators at very high strain rates usually indicate increasing strength with increasing strain rates. The author suggests that this behavior may be masked by the early failure

(less than five wave reflections within the specimen) which alters the state of uniaxial stress along the specimen.

9. The author reports the first data on high-strain-rate controlled dynamic failure. The split Hopkinson bar technique and its simple method of analysis were used to obtain reasonable unloading post-failure dynamic curves. By controlling the shape, intensity and duration of the incident wave passing through the bar-specimen-bar assembly one may devise a dynamic controlled testing system which will produce any desired unloading dynamic path.

10. In the post-failure region there is a great increase in strain (about 100 percent) with load-bearing capacity loss (about 20 percent) at different strain rates. This reduction in load-bearing capacity ability of concrete is a result of crack growth which also causes a reduction of the effective mechanical impedance ($\rho_s c_s A_s$).

The following recommendations are proposed:

a. Determine the dynamic-wave propagation properties of brittle materials by computer simulation. This wave analysis information may then be used with the conventional method to separate the inertia effect from the strain rate effect in the averaged (derived) stress-strain-strain rate relation for brittle materials.

b. A wave analysis of split-bar data may offer the possibility of studying the effects of stress gradient on rock failure under dynamic compressive conditions, a factor which has not yet been examined either experimentally or theoretically. This refinement may allow a separation of the effects of size and stress gradient on the strength and deformation, and the determination of a time dependence criterion for the prediction of true dynamic compressive strength.

c. Study the dynamic behavior of rocks and rock-like materials with the standard analysis of the split Hopkinson bar to improve the understanding of the near-failure region of dynamic loading and the effect of the strain-rate history in the deformation and failure behavior.

d. Study controlled dynamic deformation, failure, and post-failure of rocks and rock-like materials using the split Hopkinson bar apparatus.

BIBLIOGRAPHY

Ames, William F. Numerical Methods for Partial Differential Equations. New York: Barnes & Noble, Inc., 1969.

Atchley, B.L., and Furr, H.L. "Strength and Energy Absorption Capabilities of Plain Concretes under Dynamic and Static Loading," J. Amer. Concrete Inst., Proceedings, Vol. 64, No. 11, pp. 745-756, 1967.

Attewell, P.B. "Response of Rocks to High Velocity Impacts," Bull. Inst. of Min. Met., Vol. 71, pp. 705-724, 1962.

Bacon, L.O. "A Method of Determining Dynamic Tensile Strength of Rock at Minimum Loading," U.S. Bureau of Mines Rept. of Investigations 6067, 1962.

Bai, W. "The Design, Construction and Experimental Verification of a Split Hopkinson Bar," M.S. thesis, University of Missouri at Rolla, Rolla, Missouri, 1970.

Bieniawski, Z.T., Denkhaus, H.G., and Vogler, U.W. "Failure of Fractured Rock," Internat. J. Rock Mech. Min. Sci., Vol. 6, No. 3, pp. 323-341, 1969.

Birkimer, D.L. "Critical Normal Fracture Strain of Portland Cement Concrete," Ph.D. thesis, University of Cincinnati, Cincinnati, Ohio, 1968.

Birkimer, D.L. "A Possible Fracture Criteria for the Dynamic Tensile Strength of Rock," 12th Symp. Rock Mech., Rolla, Missouri (November 1970), Symp. Proceedings, AIME, pp. 573-590, 1971.

Butcher, B.M., Barker, L.M., Munson, D.E., and Lundergan, C.D. "Influence of Stress History on Time-Dependent Spall in Metals," AIAA Journal, Vol. 2, pp. 977-990, June 1964.

Crouch, S.L. "A Note on Post-Failure Stress-Strain Path Dependence in Norite," Internat. J. Rock Mech. Min. Sci., Vol. 9, No. 2, pp. 197-204, 1972.

Davies, R.M. "A Critical Study of the Hopkinson Pressure Bar," Philosophical Transactions of the Royal Society of London, Series A, Vol. 240, No. 821, pp. 375-457, 1948.

Davies, E.D.H., and Hunter, S.C. "The Dynamic Compression Testing of Solids by the Method of the Split Hopkinson Bar," J. Mech. Phys. Solids, Vol. 11, pp. 155-179, 1963.

Gilman, J.J., and Tuler, F.R. "Dynamic Fracture by Spallation in Metals," Internat. J. Fracture Mech., Vol. 6, No. 2, pp. 169-182, 1970.

BIBLIOGRAPHY - CONTINUED

Green, S.J., and Perkins, R.D. "Uniaxial Compression Tests at Varying Strain Rates on Three Geologic Materials," 10th Symp. Rock Mech., Austin, Texas (May 1968), Symp. Proceedings, AIME, pp. 35-53, 1972.

Grosvenor, N.E. "Specimen Proportion - Key to Better Compressive Strength Tests," Mining Engineering, Vol. 15, No. 1, pp. 31-33, 1963.

Hakalehto, K.O. "The Behavior of Rock Under Impulse Loads," Acta Polytechnica Scandinavica, 1969.

Hino, K. "Fragmentation of Rock Through Blasting and Shock Wave Theory of Blasting," Quart. Colo. School of Mines, Vol. 51, No. 3, pp. 191-209, 1956.

Hopkinson, B. "Collected Scientific Paper," (1912). Cambridge: Univ. Press, p. 423, 1921.

Hudson, J.A., Brown, E.T., and Fairhurst, C. "Shape of the Complete Stress-Strain Curve for Rock," 13th Symp. Rock Mech., Urbana, Illinois, August 1971.

Kolsky, H. "An Investigation of the Mechanical Properties of Materials at Very High Rates of Loading," Proceedings of the Physical Society, Section B., Vol. 62, pp. 676-700, 1949.

Kolsky, H. Stress Waves in Solids. New York: Dover Publications, Inc., 1963.

Kumar, A. "The Effect of Stress Rate and Temperature on the Strength of Basalt and Granite," Geophysics, Vol.33, No. 3, pp. 501-510, 1968.

Millinger, F.M., and Birkimer, D.L. "Measurements of Stress and Strain on Cylindrical Specimens of Rock and Concrete Under Impact Loading," Department of the Army, Ohio River Division Laboratories, Corps of Engineers, Cincinnati, Ohio, 1966.

Mogi, K. "Some Precise Measurements of Fracture Strength of Rocks Under Uniform Compressive Stress," Department of Geology and Geophysics, Massachusetts Institute of Technology, Cambridge, Massachusetts, November 1965.

Rinehart, J. "On Fractures Caused by Explosives and Impacts," Quart. Colo. School of Mines, Vol. 55, No. 4, 1960.

Rinehart, J. "Determination of the Dynamic Fracture Strength of Rock," Trans. Amer. Geophys. Union, Vol. 45, No. 1, 1964.

Rinehart, J. "Dynamic Fracture Strength of Rocks," 7th Symp. Rock Mech., University Park, Pennsylvania, June 1965.

BIBLIOGRAPHY - CONTINUED

Rinehart, J.S., and Ahlquist, N. "Comments on 'A Possible Fracture Criterion for the Dynamic Tensile Strength of Rock' by D.L. Birkimer," 12th Symp. Rock Mech., Rolla, Missouri (November 1970), Symp. Proceedings, AIME, pp. 591-592, 1971.

Rummel, F., and Fairhurst, C. "Determination of the Post-Failure Behavior of Brittle Rock Using a Servo-Controlled Testing Machine," Rock Mechanics, Vol. 2, No. 4, pp.189-204, 1970.

Saluja, S.S. "Mechanism of Rock Failure Under the Action of Explosives," 9th Symp. Rock Mech., Golden, Colorado (April 1967), Symp. Proceedings, AIME, pp. 297-319, 1968.

Shockey, D.A., Petersen, C.F., Curran, D.R., and Rosenber, J.T. "Failure of Rock Under High Rate Tensile Loads," 14th Symp. Rock Mech., University Park, Pennsylvania, June 1972.

Stowe, R.L., and Ainsworth, D.L. "Effect of Rate of Loading on Strength and Young's Modulus of Elasticity of Rock," 10th Symp. Rock Mech., Austin, Texas (May 1968), Symp. Proceedings, AIME, pp. 3-34, 1972.

Tuler, F.R., and Butcher, B.M. "A Criterion for the Time Dependence of Dynamic Fracture," Internat. J. Fracture Mech., Vol. 4, No. 4, pp. 431-437, 1968.

Watstein, D. "Effect of Straining Rate on the Compressive Strength and Elastic Properties of Concretes," J. Amer. Concrete Inst., Proceedings, Vol. 49, No. 8, pp. 729-744, 1953.

Wawersik, W.R. "Detailed Analysis of Rock Failure in Laboratory Compression Tests," Ph.D. thesis, University of Minnesota, Minneapolis, Minnesota, 1968.

Wu, P., and Hustrulid, W. "An Analysis of the Hopkinson Split Bar Method of Rock Testing," 5th Conference on Drilling and Rock Mech., Austin, Texas (January 1970), Conference Proceedings, AIME, pp. 93-100, 1971.

Wuerker, R.G. "Influence of Stress Rate and Other Factors on the Strength and Elastic Properties of Rocks," Quart. Colo. School of Mines, Vol. 54, No. 3, pp. 3-31, 1959.

VITA

Esteban Eulogio Miranda was born on February 13, 1939, in Tocopilla, Antofagasta Province, Chile. He graduated as a Mining Technician from the State Technical University School of Mines at Antofagasta, Chile, in 1959.

He received a Bachelor of Science degree in Mining Engineering from the State Technical University at Santiago in 1962, and when he submitted his thesis, he was awarded the degree of Industrial Mining Engineer in June 1967 and became a registered professional engineer.

His academic experience was obtained in the State Technical University where he served as an Assistant Professor of Engineering Mechanics (1963), an Associate Professor of Engineering Mechanics, (1964-1965), and a Professor of Mining Engineering (1966-1968). He has also been Professor of Engineering Mechanics in the Catholic University-Santiago (1964-1966), and Lecturing Professor for a course in Classical Mechanics at the Military Polytechnical Academy during 1965.

He has been on leave of absence from the State Technical University since August 1968 and has held a Fellowship from the International Bank for Development, under an aid contract for the State Technical University, for the period of September 1968 to September 1971. He received a Master of Science degree in Mining Engineering from the University of Missouri-Rolla in August 1969 and advanced to candidacy for the Ph.D. shortly thereafter. Since September 1969 he has been a Senior Research Assistant at the Rock Mechanics and Explosives Research Center in the Universityof Missouri-Rolla.

On February 20, 1964, he was married to the former Nancy C. Dubo, and he has three children.

APPENDIX A

FINITE DIFFERENCE METHOD OF ANALYSIS

Wave propagation problems in cylindrical bars are often approached with a one dimensional theory because of the many complications which arise in the use of a two or three dimensional theory. For the latter cases additional equations must be programmed and more detailed considerations must be given to the constitutive relation, boundary conditions, yield conditions, and the approximation of artificial viscosity. The incorrect use of those quantities may cause more significant errors in the desired solution than if a simple theory is employed. Also, the accuracy of two or three dimensional numerical methods is limited by the cost of performing the numerical calculations.

This appendix provides the theoretical base necessary for impact experiments utilizing a bar geometry as in spallation and dynamic stress-strain-strain rate measurements for rock and rock-like materials.

The simple one dimensional linear elastic stress wave equation, $\sigma_{XX} - \sigma_{TT} = 0$, is said to be a hyperbolic partial differential equation and has been investigated for many years. While analytical solutions exist for many of the classical problems, numerical solutions have become popular for complex propagation problems arising in science and engineering. The high-speed digital computer has made possible the numerical approach to those problems. Of the known numerical approaches, the finite-difference method is one of the most useful, and its application has been growing with the research and establishment of criteria for stability and convergence of solutions.

Two different boundary conditions are considered, each pertaining

to the particular wave propagation problems being studied, and explicit difference schemes are developed to solve them. The following discussion shows how experimental methods and computer solutions can be effectively combined to solve a problem which defies solution by either one alone.

A. LINEAR ELASTIC WAVE PROPAGATION

The mathematical model of the one dimensional solution for the analysis of longitudinal wave propagation in cylindrical bars is represented by the following governing equations given by Kolsky (1963, p. 42).

Equation of motion: $$\frac{\partial \sigma(x,t)}{\partial x} = \rho \frac{\partial v(x,t)}{\partial t} = \rho \frac{\partial^2 u(x,t)}{\partial t^2} \tag{A.1}$$

Continuity equation: $$\frac{\partial u(x,t)}{\partial x} = \frac{\partial \varepsilon(x,t)}{\partial t} \tag{A.2}$$

where by definition $$\varepsilon(x,t) = \frac{\partial u(x,t)}{\partial x}$$

Constitutive equation: Hooke's Law $$\sigma(x,t) = E\varepsilon(x,t) \tag{A.3}$$

where

$\sigma(x,t)$ = axial stress

$\varepsilon(x,t)$ = axial strain

$u(x,t)$ = axial displacement

$v(x,t)$ = longitudinal particle velocity

x = axial coordinate

t = time

ρ = mass density

E = Young's modulus of elasticity

Equations (A.1), (A.2), and (A.3) lead to the familiar elastic wave equations which may be expressed in terms of stress, strain, displacement, or particle velocity.

$$\frac{\partial^2 \Theta}{\partial t^2} = c^2 \frac{\partial^2 \Theta}{\partial x^2} \tag{A.4}$$

where $\Theta = \sigma(x,t)$, $\varepsilon(x,t)$, $u(x,t)$ or $v(x,t)$

$c = \sqrt{E/\rho}$ is the bar wave velocity.

The most elementary assumptions commonly made in the one dimensional approach result in approximate solutions, the accuracies of which depend on the following conditions:

(1) plane transverse sections of the bar remain plane during the passage of the stress wave,

(2) the stress acts uniformly over each section, and,

(3) the effects of lateral inertia are neglected.

The longitudinal expansions and contractions of sections of the bar will, however, necessarily result in lateral deformations, the ratio between lateral and longitudinal strains being given by Poisson's ratio. This lateral motion will result in a non-uniform distribution of stress across the sections and plane transverse sections will become distorted. The effect of lateral inertia in cylindrical bars is discussed by Kolsky (1963) and it is shown that it becomes important when the operative wave lengths are of the same order of magnitude or less than the diameter of the bar. The above assumptions are valid when the wavelengths are large compared with the diameter of the bar. Also, under this condition the pulse will

undergo very little change in form or amplitude as it propagates along the bar.

B. FINITE-DIFFERENCE METHOD OF APPROXIMATION FOR THE WAVE EQUATION

The dimensionless form of the wave Equation (A.4) is:

$$\frac{\partial^2\phi(X,T)}{\partial X^2} - \frac{\partial^2\phi(X,T)}{\partial T^2} = 0 \qquad (A.5)$$

where $\phi(X,T)$ may represent: displacement, $U(X,T)$, velocity, $V(X,T)$, strain, $\varepsilon(X,T)$, or stress, $S(X,T)$. The coordinates X and T represent space and time coordinates. Capital letters are used herein to designate dimensionless variable. The characteristics of the above wave equation have slopes $\frac{dT}{dX} = \pm 1$, Ames (1969).

In general the method of characteristics provides the most accurate process for solving hyperbolic equations. It is probably the most convenient method as well when the initial data are discontinuous, because the propagation of discontinuities in the solution domain along the characteristics is difficult to deal with on any grid other than a grid of characteristics. Problems involving no discontinuities, however, can be solved satisfactorily by convergent and stable finite-difference methods with rectangular grids, and the organization of the computations for a digital computer is usually easier than for the method of characteristics.

From a retangular net (Figure A.1), with constant intervals $H = \Delta X$ and $K = \Delta T$, one may write:

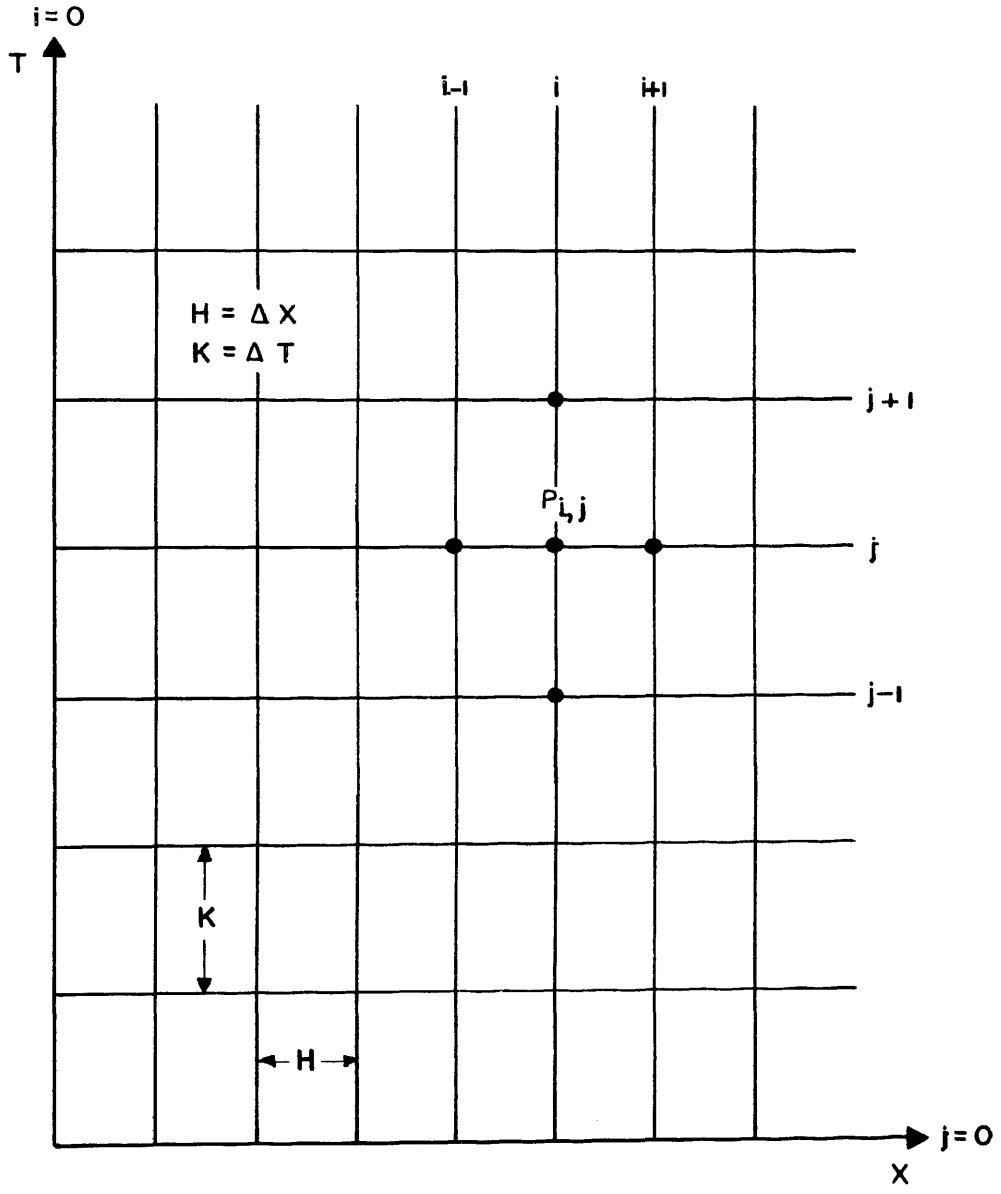

Figure A.1 - Rectangular net. $X_i = i\Delta X = iH$ and $T_j = j\Delta T = jK$

$$\phi_{i,j} = \phi(P_{i,j}) = \phi(X_i,T_j) = \phi(i\Delta X, j\Delta T) = \phi(iH,jK)$$

for $-\infty < i < \infty$

$0 \leq j < \infty$

The finite-difference approximation with central-difference expressions for the non-dimensional wave Equation (A.5) has been given by Ames (1969, p. 193) as follows:

$$\frac{\Phi_{i,j+1} - 2\Phi_{i,j} + \Phi_{i,j-1}}{K^2} = \frac{\Phi_{i+1,j} - 2\Phi_{i,j} + \Phi_{i-1,j}}{H^2} \qquad (A.6)$$

where $\Phi_{i,j}$ is the finite difference solution at point $P_{i,j} = P(X_i,T_j)$. This scheme enables one to solve for $\Phi_{i,j+1}$ since all of the other values in the Equation (A.6) are presumed to be known; that is: $\Phi_{i-1,j}$; $\Phi_{i,j}$; $\Phi_{i+1,j}$; $\Phi_{i,j-1}$ are known.

$$\text{Thus, } \Phi_{i,j+1} = M^2(\Phi_{i-1,j} + \Phi_{i+1,j}) + 2(1-M^2)\Phi_{i,j} - \Phi_{i,j-1} \qquad (A.7)$$

where

$$M = K/H = \Delta T/\Delta X$$

The explicit central difference formula (A.7) allows the calculation of a single value on a new row, $j + 1$, in terms of values on the previous rows, j and $j - 1$ (see computational molecule, Figure A.2). Thus to start the marching process the first two rows, $j = 0$ and $j = 1$, must be ob-

tained initially after which the step-by-step calculation proceeds in a simple way.

C. DIFFERENCE SCHEME FOR THE PURE INITIAL VALUE PROBLEM

A pure initial value problem exists for the interior points of cylindrical bars since no boundary condition is involved. Ames (1969, p. 193-196) has formulated this as

$$\phi_{XX} = \phi_{TT} \ , \ T > 0$$

$$\phi(X,0) = F(X) \tag{A.8}$$

$$\phi_T(X,0) = G(X)$$

While the initial condition specifies the exact initial values $\phi_{i,0}$ on the line T = 0,

$$\phi_{i,0} = \phi(X_i,0) = F(X_i) = F(i\Delta X) = F(iH) = F_i \tag{A.9}$$

the second initial condition in Equation (A.8) is used to find approximate values on the line T = K, or j = 1, with a "false" boundary at j = -1 and the second order central difference formula

$$\frac{\partial \phi}{\partial T}\Big|_{i,0} = \frac{\phi_{i,1} - \phi_{i,-1}}{2K} + O(K^2) \tag{A.10}$$

Writing $G(X_i) = G(i\Delta X) = G(iH) = G_i$ the following approximation is obtained

$$\Phi_{i,1} - \Phi_{i,-1} = 2KG_i \tag{A.11}$$

with an associated error of K^2. With j = 0 in the approximated wave Equation (A.7), the result is

$$\Phi_{i,1} = M^2 (\Phi_{i-1,0} + \Phi_{i+1,0}) + 2(1-M^2) \Phi_{i,0} - \Phi_{i,-1}$$

Upon replacing $\Phi_{i,-1}$ with its value from Equation (A.11) and solving for $\Phi_{i,1}$, one obtains

$$\Phi_{i,1} = \frac{1}{2} M^2(F_{i-1} + F_{i+1}) + (1 - M^2) F_i + KG_i \tag{A.12}$$

Equation (A.12) gives approximate values of Φ on the line j = 1. These values would be exact if G(X) were a linear function of X. Thus Equations (A.7), (A.9), and (A.12) provide the necessary difference solution for the pure initial value problem. These equations can be simplified by using the criteria of stability and convergence, $M \leq 1$. The condition of M = 1 is of special interest not only because it corresponds to maximizing the permissible time interval K for fixed H, but also because it has the interesting property that any solution of the differential wave Equation (A.8) also satisfies exactly the difference equation

$$\Phi_{i,j+1} = \Phi_{i-1,j} + \Phi_{i+1,j} - \Phi_{i,j-1} \quad \text{for } j \geq 1 \tag{A.13}$$

The maximum time increment K reduces the number of time steps (or computation time) for the duration of interest and thereby decrease possible round off errors. The finite-difference Equation (A.13) is there-

fore the simplest form of the approximated wave Equation (A.7), resulting in saving of computing steps and time. The round off error may be further reduced since the use of M = 1 as a multiplier in the difference formulas does not introduce any error.

D. DIFFERENCE SCHEME FOR BOUNDARY POINTS

Two selected boundary conditions are considered. These are of practical interest in developing solutions for wave analysis of the 1) long bar spallation tests, and 2) split Hopkinson pressure bar experiments, both for linear elastic specimens.

1. ϕ is prescribed at boundary

This is the simplest boundary value problem, typical of the long bar spallation tests, since no computation is needed at the boundary and all calculations are performed in the interior. Therefore, the method described previously in Section C applies.

The boundary condition common to the long bar spallation experiments is that stresses vanish at the free end. Solutions to this problem are obtained by starting with previously obtained values of ϕ in the first two rows [obtained from the prescribed initial values of $\phi(X,0)$ and $\phi_T(X,0)$, and the known boundary data $\phi(0,T)$ and $\phi(L,T)$] and working forward in time by means of the difference equation.

2. Boundary conditions at interface between two elastic bars

This boundary value problem is directly related to the wave analysis of the split Hopkinson pressure bar. Consider two long linear elastic bars of different materials joined to become one continuous axisymmetric bar. For the sake of simplicity the cross-sectional areas of rods will be considered to be same. The material properties on either side

of the joint plane are shown in Figure A.3 . It is convenient to choose the coordinate system so that x = 0 at the joint plane.

At x = 0 (Interface I) the boundary conditions are:

a. Balance of forces: $\sigma(0^-;t) = \sigma(0^+;t)$ (A.14)

Hence, from the constitutive equation (Hooke's Law) (A.3),

$$E_1\varepsilon(0^-;t) = E_2\varepsilon(0^+;t)$$

or from the definition of strain,

$$u_x|_{(0^-;t)} = K_1\, u_x|_{(0^+;t)} \tag{A.15}$$

where $$K_1 = E_2/E_1 \tag{A.16}$$

Also from Equation (A.14)

$$\frac{\partial^2\sigma(0^-;t)}{\partial t^2} = \frac{\partial^2\sigma(0^+;t)}{\partial t^2} \tag{A.17}$$

b. Continuity of displacements: $u(0^-;t) = u(0^+;t)$ (A.18)

Hence,

$$\frac{\partial^2 u(0^-;t)}{\partial t^2} = \frac{\partial^2 u(0^+;t)}{\partial t^2} \tag{A.19}$$

The wave equation for displacements [Equation (A.4)] for both sides of the Interface I yields:

$$u_{tt}|_{(0^-;t)} = c_1^2 \, u_{xx}|_{(0^-;t)} \tag{A.20}$$

$$u_{tt}|_{(0^+;t)} = c_2^2 \, u_{xx}|_{(0^+;t)} \tag{A.21}$$

Combining Equations (A.20) and (A.21), and using Equation (A.19) one obtains

$$u_{xx}|_{(0^-;t)} = K_2 \, u_{xx}|_{(0^+;t)} \tag{A.22}$$

where

$$K_2 = (c_2/c_1)^2 \tag{A.23}$$

The equation of motion [Equation (A.1)] for both sides of the Interface I yields:

$$\sigma_x|_{(0^-;t)} = \rho_1 \, u_{tt}|_{(0^-;t)} \tag{A.24}$$

$$\sigma_x|_{(0^+;t)} = \rho_2 \, u_{tt}|_{(0^+;t)} \tag{A.25}$$

Equations (A.24) and (A.25) may be combined and used with Equation (A.19) to yield:

$$\sigma_x|_{(0^-;t)} = K_{11} \, \sigma_x|_{(0^+;t)} \tag{A.26}$$

where

$$K_{11} = \rho_1/\rho_2 \tag{A.27}$$

The wave Equation for stresses (A.4) can be written for both sides of the Interface I as:

$$\sigma_{tt}|_{(0^-,t)} = c_1^2 \, \sigma_{xx}|_{(0^-,t)} \tag{A.28}$$

$$\sigma_{tt}|_{(0^+,t)} = c_2^2 \, \sigma_{xx}|_{(0^+,t)} \tag{A.29}$$

Combining Equations (A.28) and (A.29) and using (A.17) yields:

$$\sigma_{xx}|_{(0^-,t)} = K_2 \, \sigma_{xx}|_{(0^+,t)} \tag{A.30}$$

Therefore, the three boundary conditions at Interface I (x = 0) can be expressed for $\psi = \sigma$ or u, as:

(1) $$\psi(0^-,t) = \psi(0^+,t) = \psi(0,t) \tag{A.31}$$

[From Equations (A.14) and (A.18)]

(2) $$\psi_x|_{(0^-,t)} = K_1 \, \psi_x|_{(0^+,t)} \tag{A.32}$$

where $$K_1 = \begin{cases} \rho_1/\rho_2 \text{ when } \phi=\sigma \\ E_2/E_1 \text{ when } \phi=u \end{cases} \tag{A.33}$$

[From Equations (A.26) and (A.15)]

(3) $$\psi_{xx}|_{(0^-,t)} = K_2 \psi_{xx}|_{(0^+,t)} \tag{A.34}$$

where $$K_2 = (c_2/c_1)^2 \tag{A.35}$$

[From Equations (A.30) and (A.22)]

For the difference solution of the boundary value problem described the spatial meshes are chosen as shown in Figure A.4 . The mesh sizes depend on the wave velocities of the material and the time increment which is chosen by considering pulse shape and bar length. That is,

$$\Delta x_1 = c_1 \Delta t_1 \tag{A.36}$$

$$\Delta x_2 = c_2 \Delta t_2 \tag{A.37}$$

since $M = \Delta T / \Delta X = 1$

and if $\Delta t_1 = \Delta t_2 \ (= \Delta t)$

then
$$\frac{\Delta x_1}{\Delta x_2} = \frac{c_1}{c_2} \tag{A.38}$$

Taylor's expansion of ψ for both sides of the Interface I, neglecting terms higher than second order, yields:

$$\psi(-\Delta x_1, t) = \psi(0^-, t) + (-\Delta x_1)\ \psi_x|_{(0^-, t)} + \frac{1}{2}(-\Delta x_1)^2\ \psi_{xx}|_{(0^-, t)} \tag{A.39}$$

$$\psi(\Delta x_2, t) = \psi(0^+, t) + (\Delta x_2)\ \psi_x|_{(0^+, t)} + \frac{1}{2}(\Delta x_2)^2\ \psi_{xx}|_{(0^+, t)} \tag{A.40}$$

where ψ can be either σ or u

Eliminating ψ_x from Equations (A.39), (A.40), and (A.32) yields:

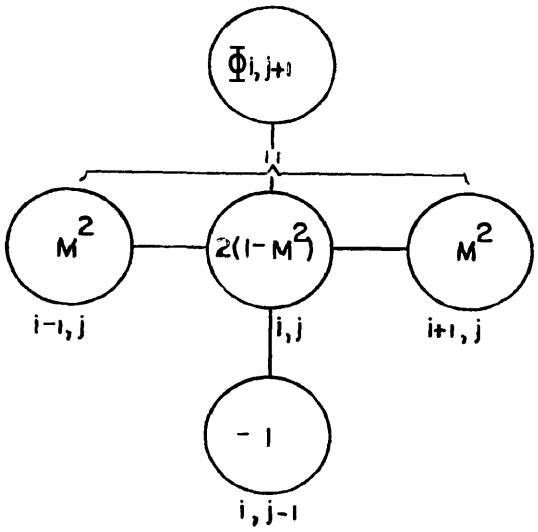

Figure A.2 - Computational molecule for the explicit scheme of Equation (A.7)

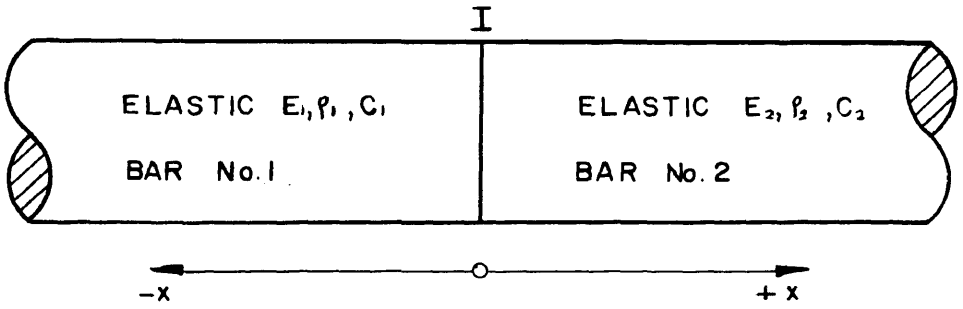

Figure A.3 - Interface between two linear elastic bars

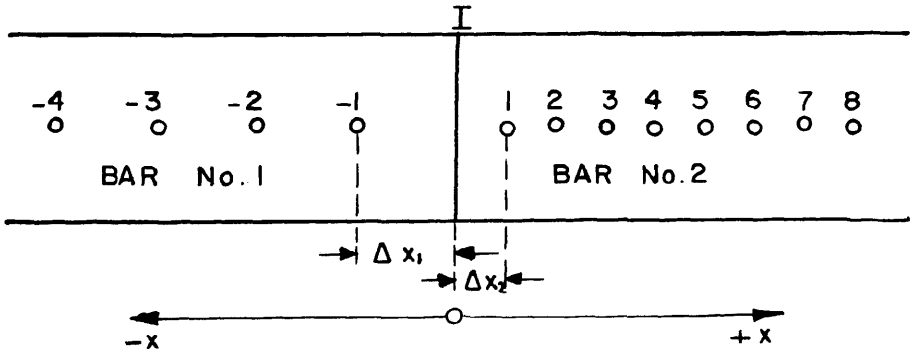

Figure A.4 - Difference spatial mesh

$$\Delta x_2\ \psi(-\Delta x_1,t) + K_1\Delta x_1\psi(\Delta x_2,t) = \Delta x_2\ \psi(0^-,t) + K_1\Delta x_1\ \psi(0^+,t) + \frac{1}{2}\Delta x_2\Delta x_1^2\ \psi_{xx}|_{(0^-,t)} + \frac{1}{2}K_1\Delta x_1\Delta x_2^2\ \psi_{xx}|_{(0^+,t)} \tag{A.41}$$

where K_1 is given by Equation (A.33).

Solving Equations (A.41), (A.34), and (A.31) for $\psi_{xx}|_{(0^-,t)}$ yields:

$$\psi_{xx}|_{(0^-,t)} = \frac{2}{\Delta x_1\Delta x_2\left(\Delta x_1+\frac{K_1}{K_2}\Delta x_2\right)}\left\{\Delta x_2\ \psi(-\Delta x_1,t) - (\Delta x_2 + K_1\Delta x_1)\ \psi(0,t) + K_1\ \psi(\Delta x_2,t)\right\} \tag{A.42}$$

Substituting Equation (A.42) into the wave Equation, $\psi_{tt}(x,t) = c^2\ \psi_{xx}(x,t)$ one obtains

$$\{\text{right hand side of Equation (A.42)}\}\ c_1^2 = \psi_{tt}(0^-,t) \tag{A.43}$$

The difference form of Equation (A.43) is:

$$\frac{2c_1^2}{\Delta x_1\Delta x_2\left(\Delta x_1 + \frac{K_1}{K_2}\Delta x_2\right)}\left\{\Delta x_2\Psi_{-1,j} - (\Delta x_2+K_1\Delta x_1)\ \Psi_{0,j} + K_1\Delta x_1\Psi_{1,j}\right\} = \frac{\Psi_{0,j+1} - 2\ \Psi_{0,j} + \Psi_{0,j-1}}{(\Delta t)^2} \tag{A.44}$$

where $\Psi_{i,j}$ is the finite difference solution at point $P_{i,j} = P(x_i, t_j)$.

Equation (A.44) with Equation (A.36) and (A.38) becomes:

$$\Psi_{0,j+1} = 2\left(\frac{1}{1 + \frac{K_1}{K_2}\frac{c_2}{c_1}}\right)\Psi_{-1,j} + 2\left(1 - \frac{1}{1 + \frac{K_1}{K_2}\frac{c_2}{c_1}}\right)\Psi_{1,j} - \Psi_{0,j-1} \qquad (A.45)$$

where

$$\frac{K_1}{K_2}\frac{c_2}{c_1} = \begin{cases} \dfrac{E_1}{E_2}\dfrac{c_2}{c_1}, & \text{if } \Psi \text{ is stress, and} \\ \dfrac{E_2}{E_1}\dfrac{c_1}{c_2}, & \text{if } \Psi \text{ is displacement} \end{cases}$$

Thus Equations (A.45) and (A.9) provide the necessary explicit difference formulas for solving the interface boundary problem.

E. MODELING FOR COMPUTER CALCULATIONS

In propagation or "marching" problems the solution marches out from the initial state guided and modified in transit by the side boundary conditions. In this section the "time marching" problems of spallation and split Hopkinson bar will be presented as they have been formulated to be solved by computer. Because of the length of the codes, a listing is not given here, but is available at the UMR Rock Mechanics and Explosives Research Center library.

1. Spallation Problem

The finite-difference model corresponding to the long bar spallation experiment is shown in Figure A.5. The boundary data at x = 0 will be provided by the gages reading at location 1 near the impact end.

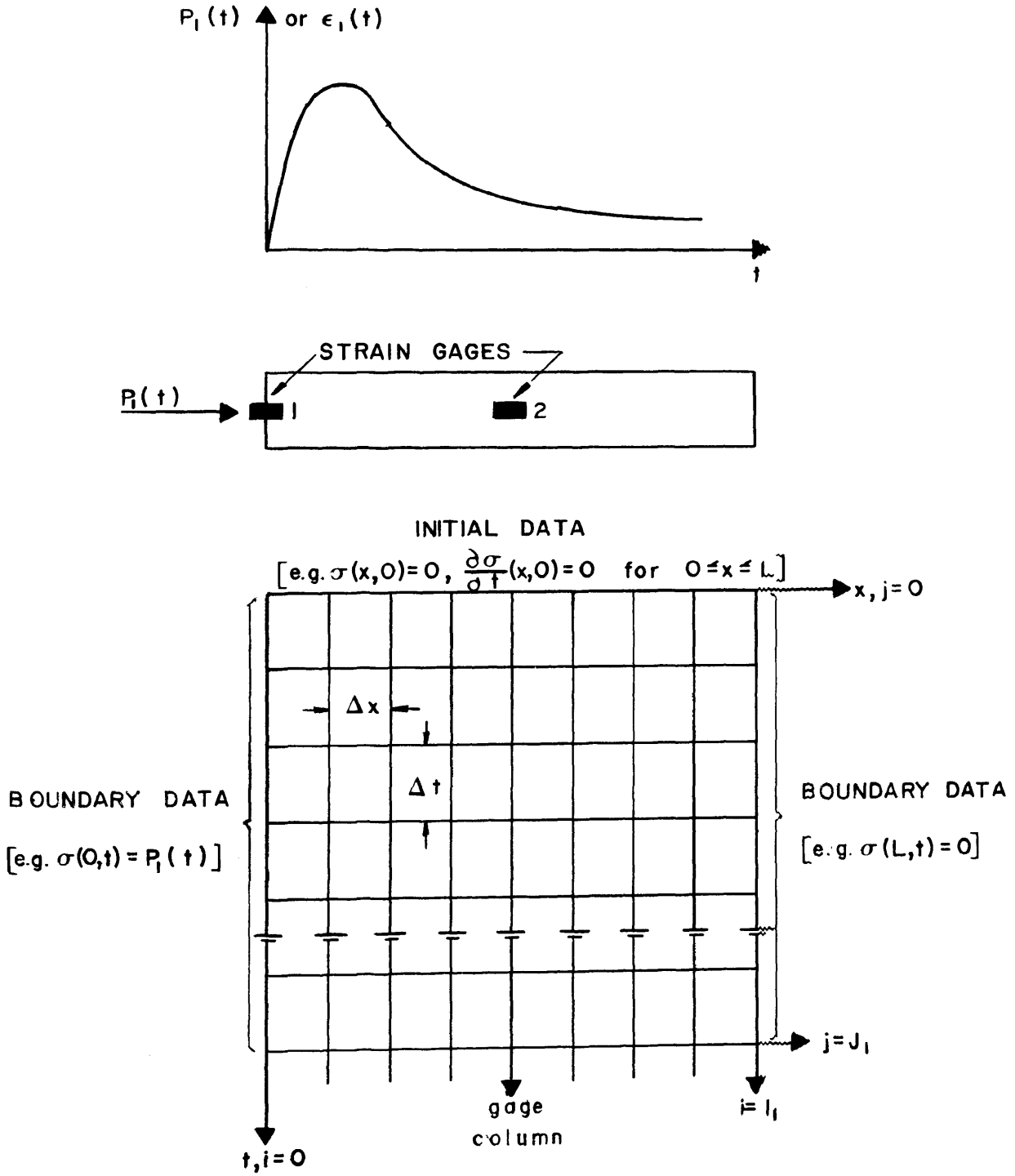

Figure A.5 - (Top) Incident elastic strain pulse $\varepsilon_1(t)$ at gage 1. The elastic stress pulse is $P_1(t) = E\varepsilon_1(t)$
(Middle) Long bar of length L; $L = I_1\Delta x$
(Bottom) Rectangular net illustrating input of two-point initial data and one-point boundary data for the finite difference model at long bar experiments

Due to most efficacious choice of $M(c\Delta t/\Delta x = 1)$, Equation (A.7) becomes Equation (A.13) which can be expressed for stresses as:

$$\sigma_{i,j+1} = \sigma_{i-1,j} + \sigma_{i+1,j} - \sigma_{i,j-1} \qquad (A.46)$$

The above Equation (A.46) is an explicit formula for the unknown stress $\sigma_{i,j+1}$ at the (i,j+1)th mesh point in terms of known stresses along the (j and j-1)th time rows. Hence, to start the marching process, the first two rows, j = 0 and j = 1, must be obtained. The known boundary and initial values are displayed in Figure A.5 , where the first row, at j = 0, is given by:

$$\sigma_{0,0} = P_1(0)$$

$$\sigma_{i,0} = 0 \quad \text{for } 0 < i \leq I_1 \ ,$$

and the second row, at j = 1, is given by

$$\sigma_{0,1} = P_1(\Delta t) = P_1(1)$$

$$\sigma_{1,1} = P_1(0)$$

$$\sigma_{i,1} = 0 \quad \text{for } 1 < i \leq I_1$$

The third row, at j = 2, is then given by

$$\sigma_{0,2} = P_1(2\Delta t) = P_1(2)$$

$\sigma_{i,2}$ = {right hand side of Equation (A.46) for j = 1 and $0 < i < I_1$}

$$\sigma_{I_1,2} = 0$$

The marching process may continue as long as desired, that is $j = J_1$ where $J_1 \Delta t$ = total finite differencing time.

The computer program must have at least the following features:

a. the small time increment $\Delta t (= \Delta x/c)$ must be computed from the given input values of Δx and c.

b. the points, $P_1(i) = P_1(i\Delta t)$ for i = 0,1,2..., for the incident stress wave $P_1(t)$ at small time intervals of Δt must be computed from the experimental pulse input data. Because of the large number of increments Δt, a direct reading of the incremental strain values from the enlarged oscilloscope records is difficult.

Since the strain curves in this investigation were fairly smooth, greater time increments are used in the digitizing process and additional intermediate points computed by linear interpolating between digitized input experimental data points. The use of more accurate interpolation formulas was not justified since the experimental accuracy did not warrant an additional refining effort.

c. the calculation of the row j + 1 from the known rows j and j - 1, using Equation (A.46) must be done in such a way that the available computer storage is adequate. See flowchart in Figure A.6.

A flow diagram of the finite-difference computer code used in this dissertation is shown in Figure A.7.

2. Split Hopkinson Bar Problem

The finite-difference model corresponding to the Kolsky's experimental technique is shown in Figure A.8. The boundary data at x = 0

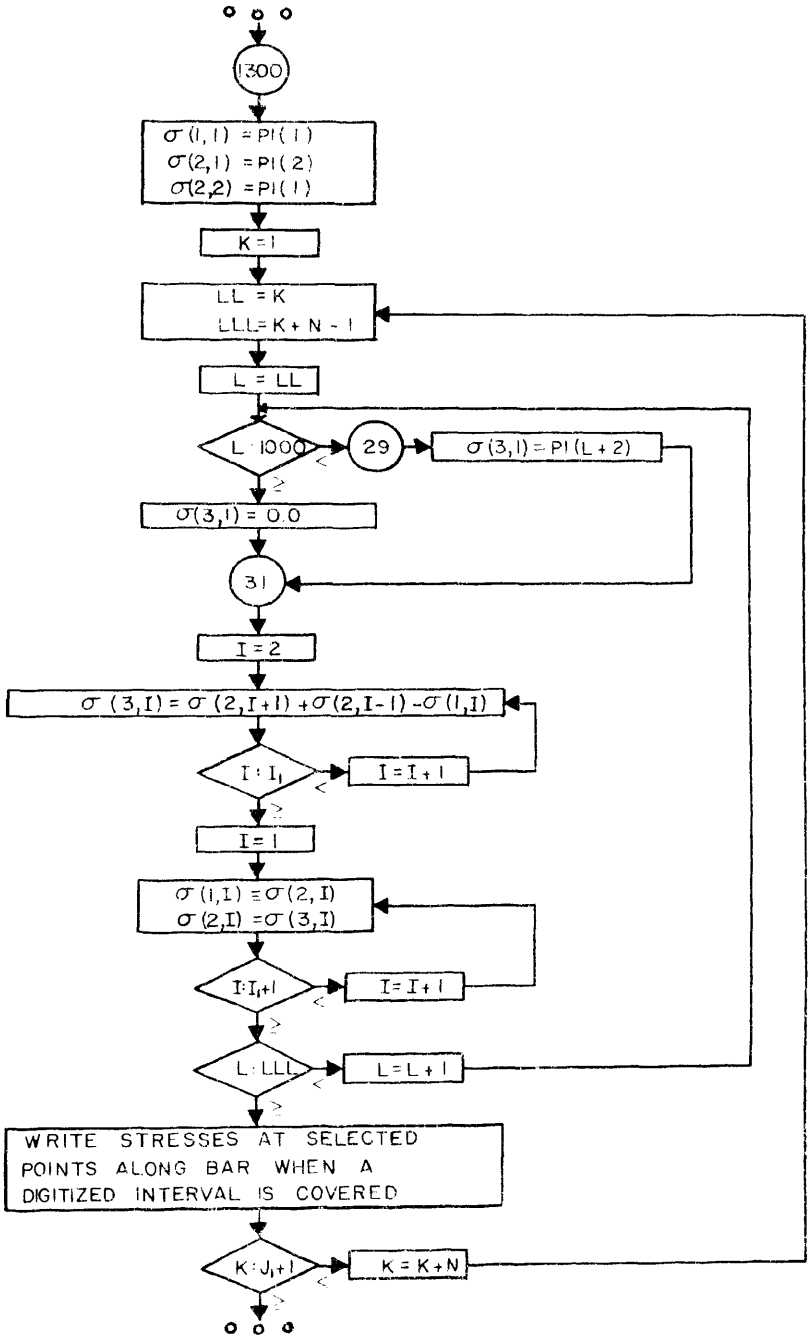

Figure A.6 - Flowchart for the calculation of stresses along long bar $\sigma(j,i) = \sigma_{i,j}$. To eliminate the zero value of the subscript i and j were adjusted from $(0,I_1)$ and $(0,J_1)$ to $(1,I_1+1)$ and $(1,J_1+1)$. N = numbers of subintervals Δt between digitized input data points. NPØINT = total number of digitized input data points. NSUB = total number of points over the incident stress pulse, separated by Δt.

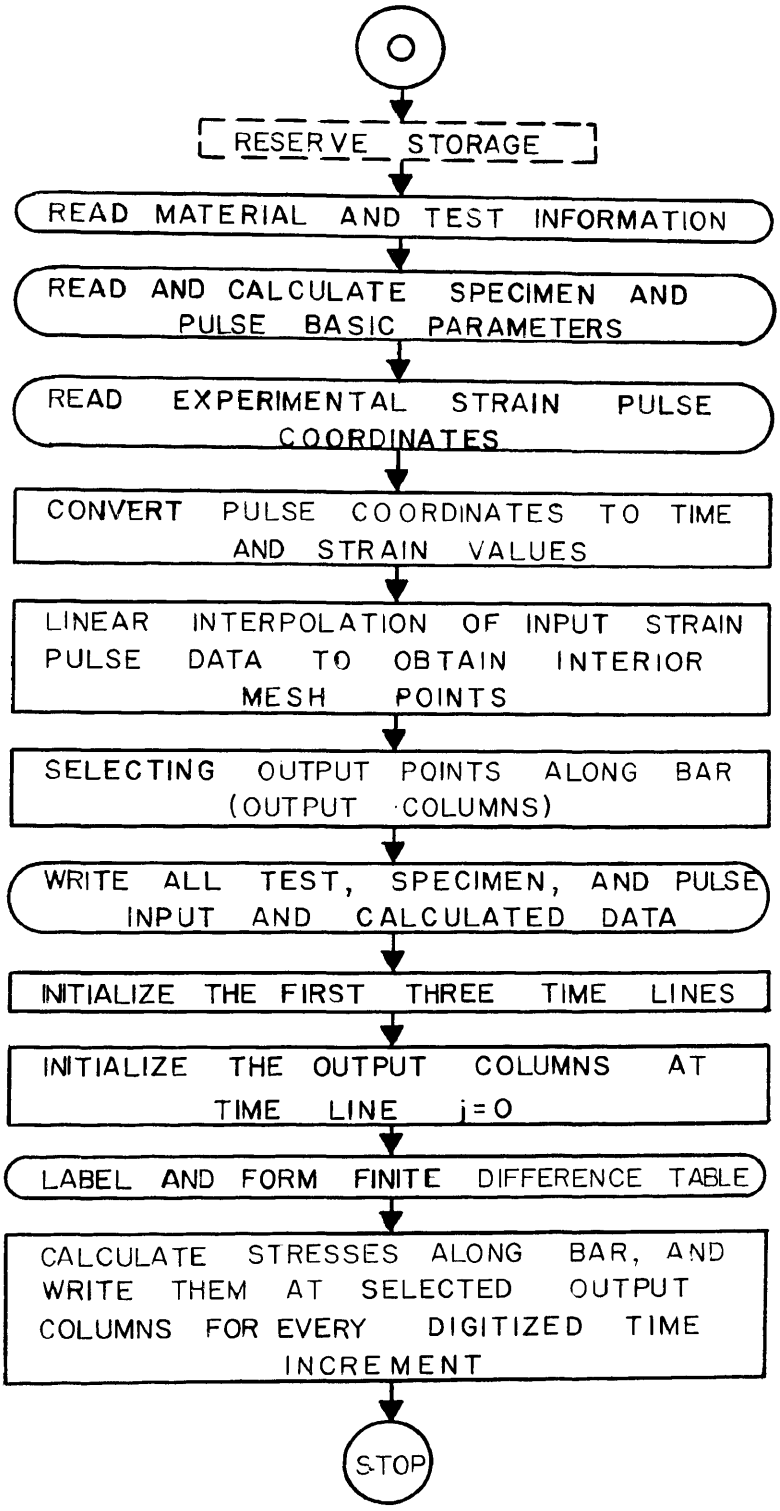

Figure A.7 - Flow diagram of the finite difference computer code

were provided by the gages located on the loading bar near the impact end.

Similarly as in the spallation problem, to start the time marching process, values for the first two rows are needed. From the known boundary and initial values displayed in Figure A.8, the first row, at $j = 0$, is given by:

$$\sigma_{0,0} = P_1(0)$$

$$\sigma_{i,0} = 0 \qquad \text{for } 0 < i \leq I_3$$

the second row, at $j = 1$, is given by

$$\sigma_{0,1} = P_1(\Delta t) = P_1(1)$$

$$\sigma_{1,1} = P_1(0)$$

$$\sigma_{i,1} = 0 \qquad \text{for } 0 < i \leq I_3$$

the third row, at $j = 2$, is then given by:

$$\sigma_{0,2} = P_1(2\Delta t) = P_1(2)$$

$$\sigma_{i,2} = [\text{right hand side of Equation (A.46) for } j = 1 \text{ and } 0 < i < I_1]$$

$$\sigma_{I_1,2} = 2\left(\frac{1}{1 + \frac{E_I c_s}{E_s c_I}}\right)\sigma_{I_1-1,1} + 2\left(1 - \frac{1}{1 + \frac{E_I c_s}{E_s c_I}}\right)\sigma_{I_1+1,1}$$

$$- \sigma_{I_1,0}$$

[from Equation (A.45) for stresses]

$$\sigma_{i,2} = \{\text{right hand side of Equation (A.46) for } j = 1 \text{ and } I_2 < i < I_3\}$$

$$\sigma_{I_3,0} = 0$$

The step by step numerical calculation may continue ahead as long as it is desired to solve the elastic wave propagation problem being studied (or until $j = J_1$, where $J_1\ \Delta t$ = total finite differencing time).

The computer program must have at least the following features:

a. the small time increment Δt $(=\Delta x_s/c_s)$ must be computed from the given input values of Δx_s and c_s for the specimen;

b. the small space increment Δx_I $(=c_I \Delta x_s/c_s)$ for the bars must be computed from the given input values of $c_I, \Delta x_s/c_s$;

c. the points $P_1(i) = P_1(i\Delta t)$ must be calculated in the same manner as in the spallation problem;

d. the calculation of the line $j + 1$ must be done in a similar way as explained in the spallation problem.

The flow diagram of the finite-difference computer code used for the split-bar configuration follows the general pattern as for the long bar spallation problem shown in Figure A.7 .

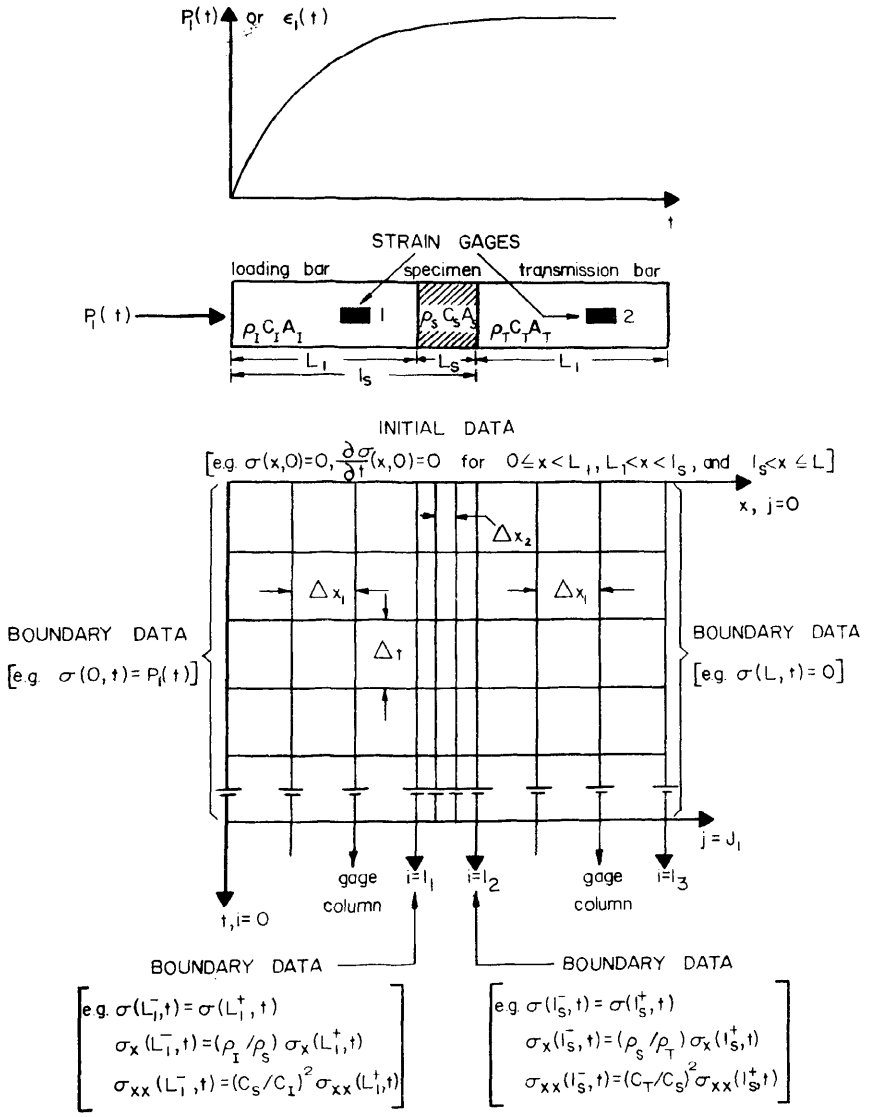

Figure A.8 - (Top) Incident (loading) elastic strain pulse $\varepsilon_1(t)$ at Gage 1. The elastic stress pulse is $P_1(t) = E\,\varepsilon_1(t)$

(Middle) Split Hopkinson bars of total length L; $L = 2L_1+L_S$, $L_1=I_1\Delta x$, $L_S=(I_2-I_1)\Delta x_2$ and I_3 = total number of space increments

(Bottom) Rectangular net illustrating input of two-point initial data and one and three-point boundary data for the finite-difference model of split Hopkinson pressure bar experiments.

APPENDIX B

SPALLATION DATA FOR CONCRETE

Graphs of the Comparisons of Experimental
and Theoretical Strains
and Strain Rate History at Spall Plane

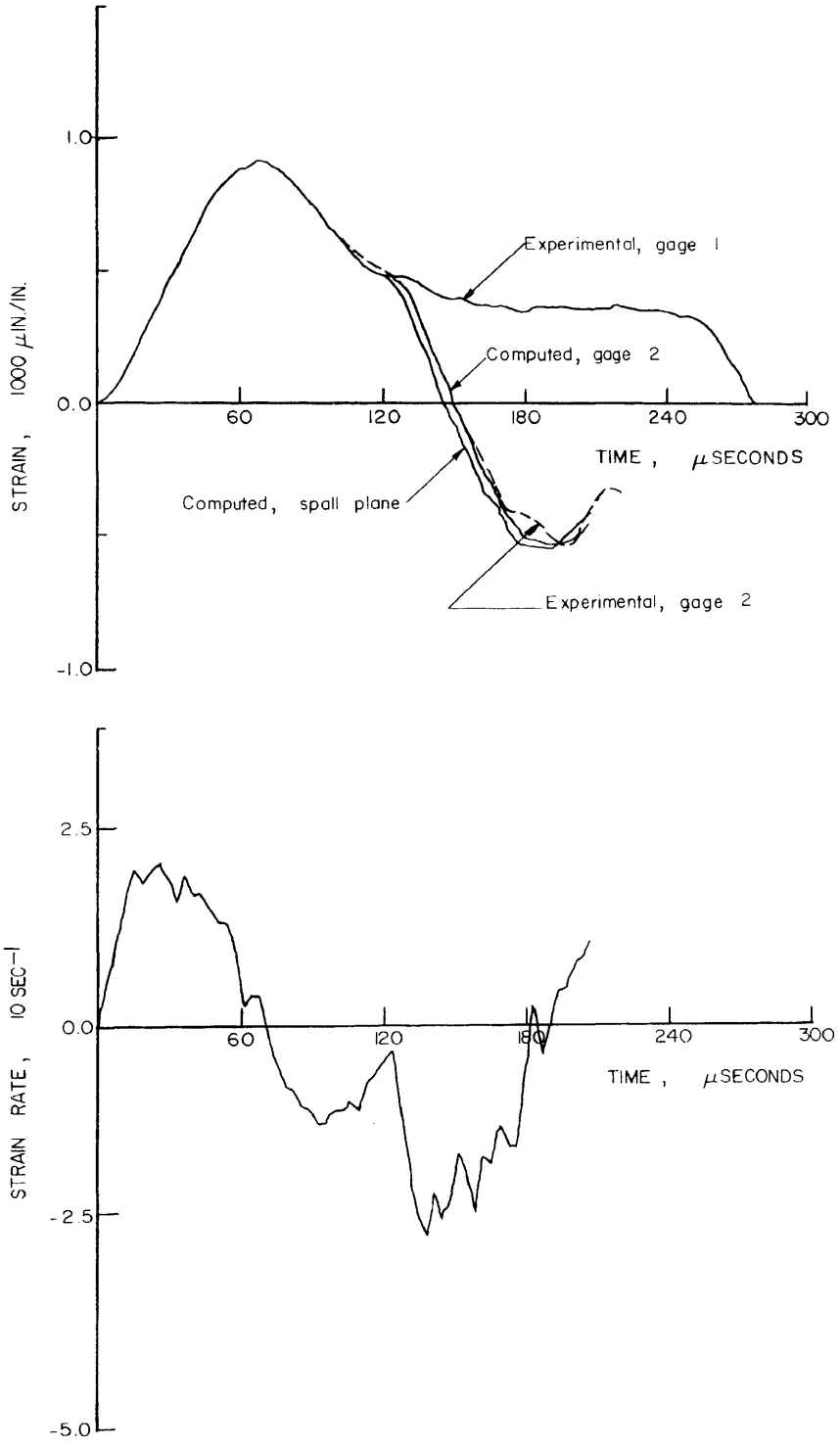

Figure B.1 (a) - Comparison of experimental and theoretical strains for specimen CC-H-2-1 (Compression positive)
(b) - Strain rate history at spall plane for specimen CC-H-2-1

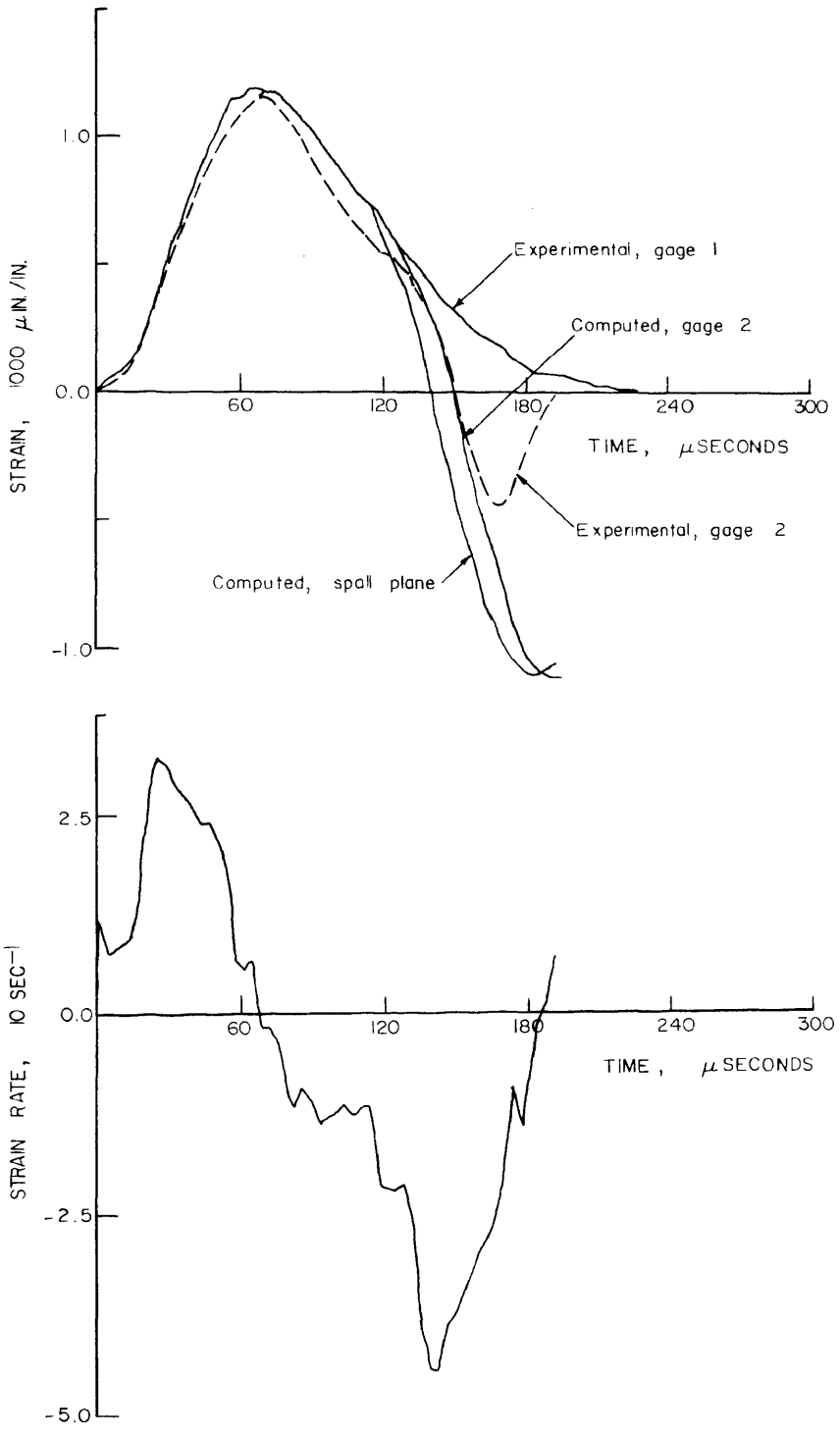

Figure B.2 (a) - Comparison of experimental and theoretical strains for specimen CC-J-2-1 (compression positive)
(b) - Strain rate history at spall plane for specimen CC-J-2-1

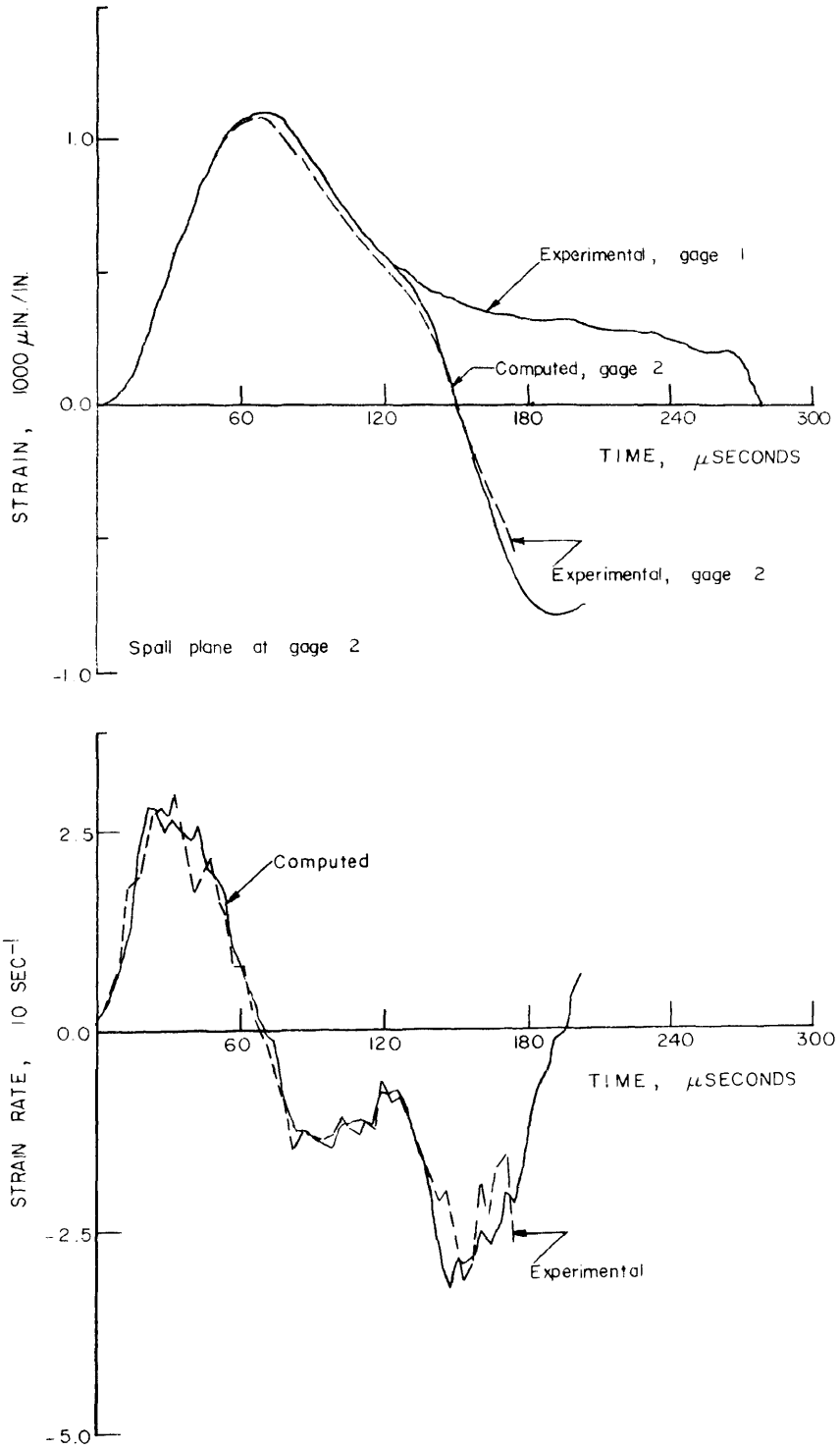

Figure B.3 (a) - Comparison of experimental and theoretical strains for specimen CC-J-3-1 (compression positive)
(b) - Strain rate history at spall plane for specimen CC-J-3-1

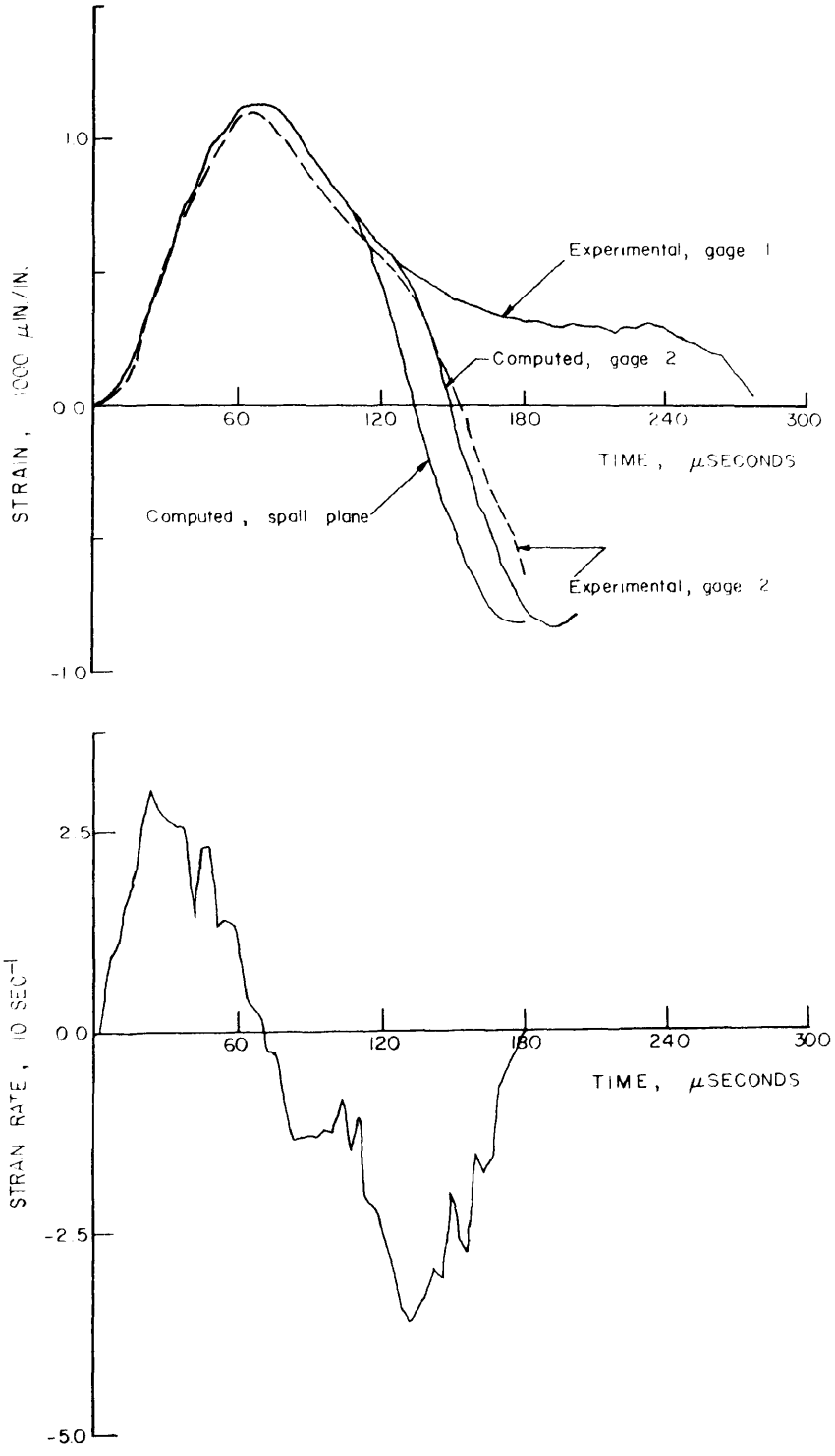

Figure B.4 (a) - Comparison of experimental and theoretical strains for specimen CC-J-4-1
(b) - Strain rate history at spall plane for specimen CC-J-4-1

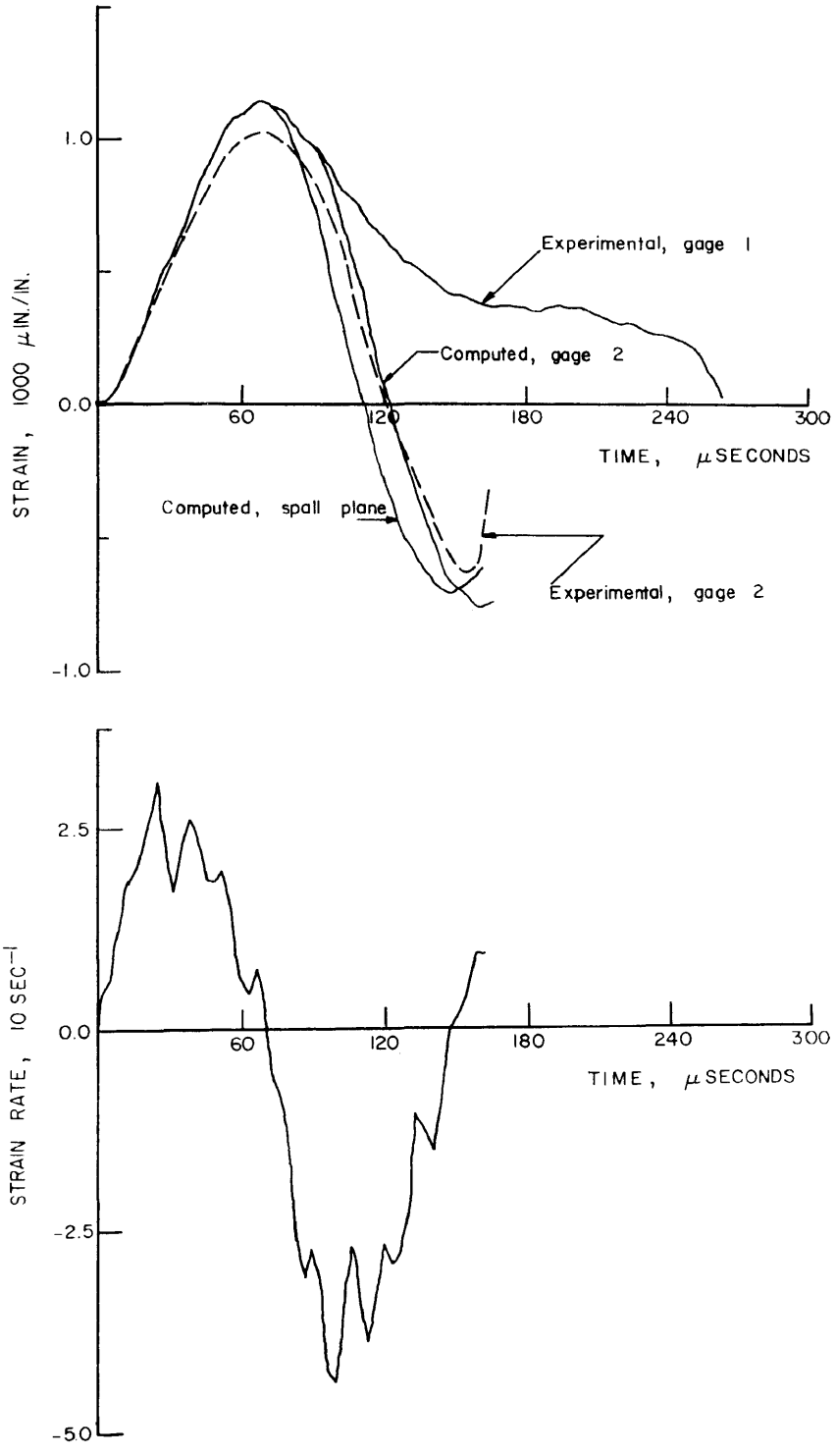

Figure B.5 (a) - Comparison of experimental and theoretical strains for specimen CC-K-1 (compression positive)
(b) - Strain rate history at spall plane for specimen CC-K-1

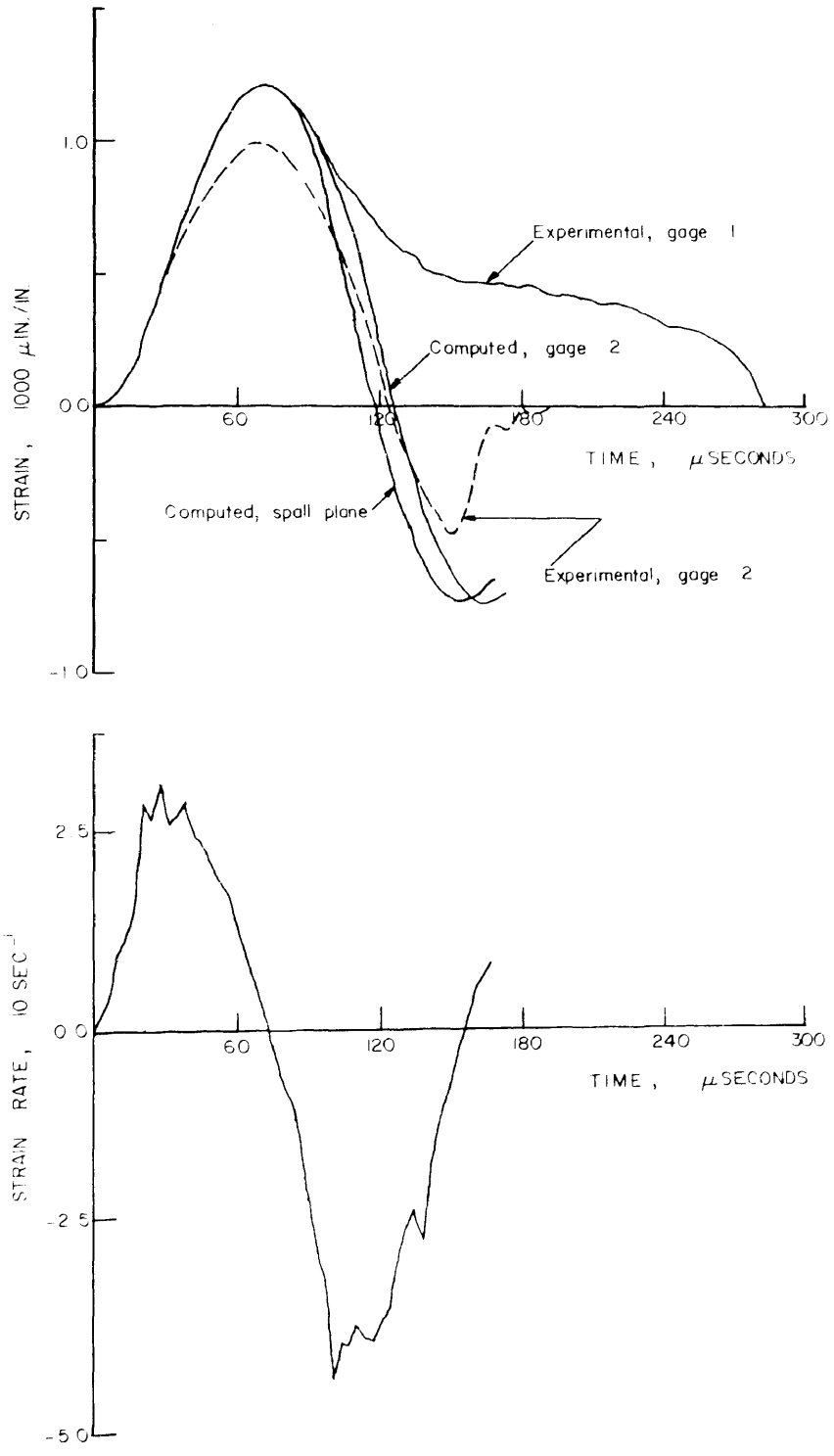

Figure B.6 (a) - Comparison of experimental and theoretical strains for specimen CC-K-2 (compression positive)
(b) - Strain rate history at spall plane for specimen CC-K-2

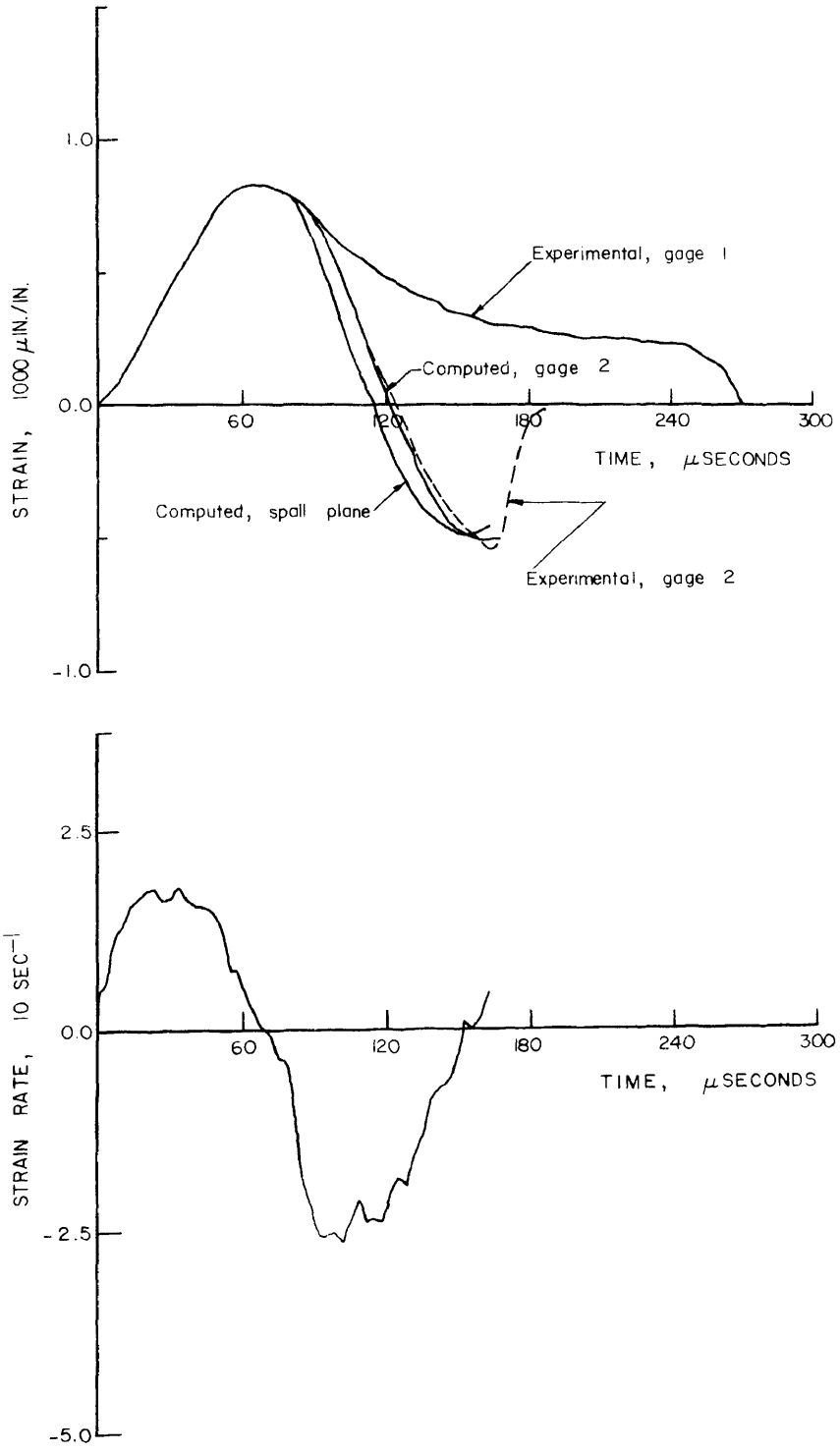

Figure B.7 (a) - Comparison of experimental and theoretical strains for specimen CC-L-1 (compression positive)
(b) - Strain rate history at spall plane for specimen CC-L-1

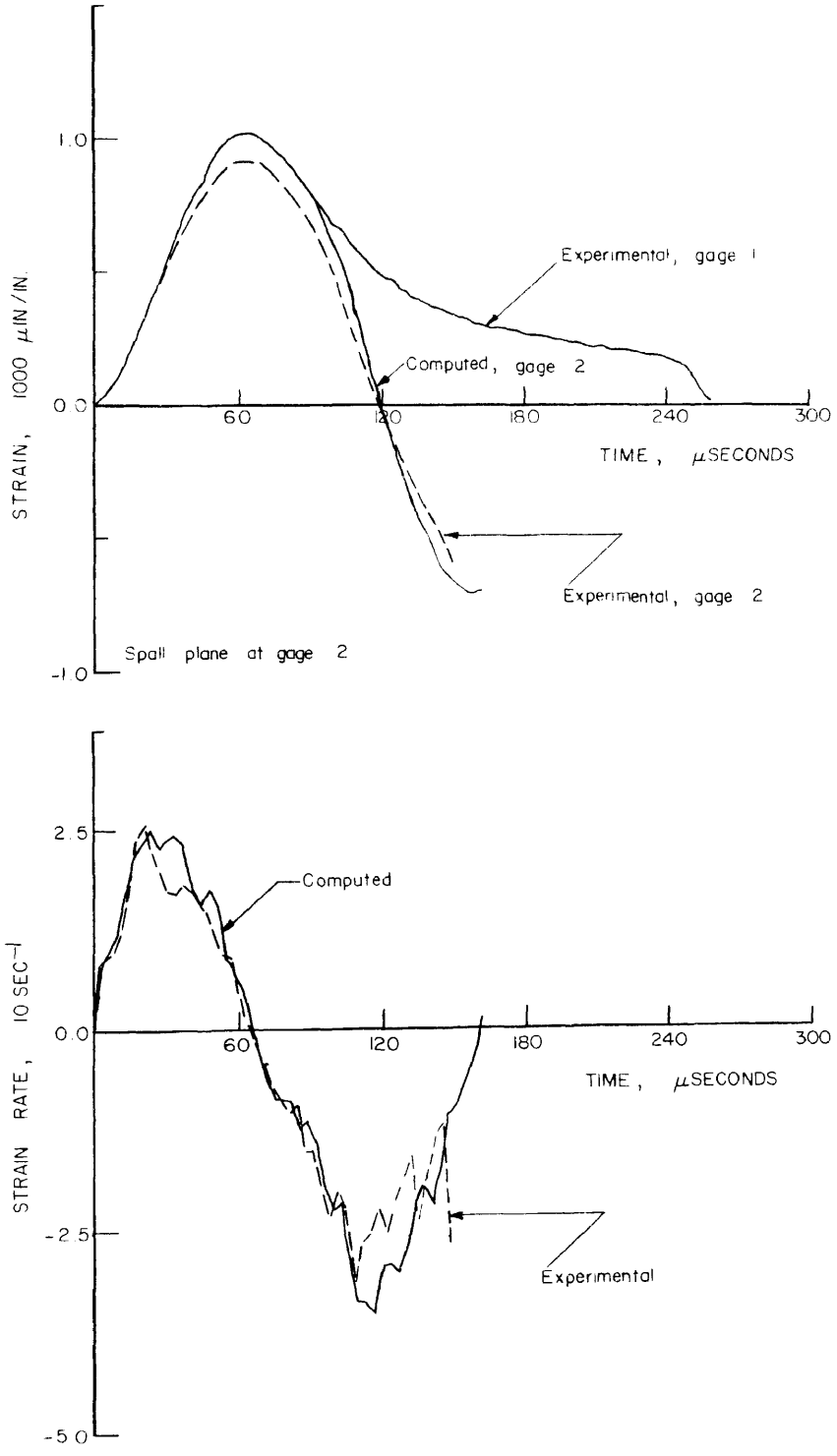

Figure B.8 (a) - Comparison of experimental and theoretical strains for specimen CC-L-2 (compression positive)
(b) - Strain rate history at spall plane for specimen CC-L-2

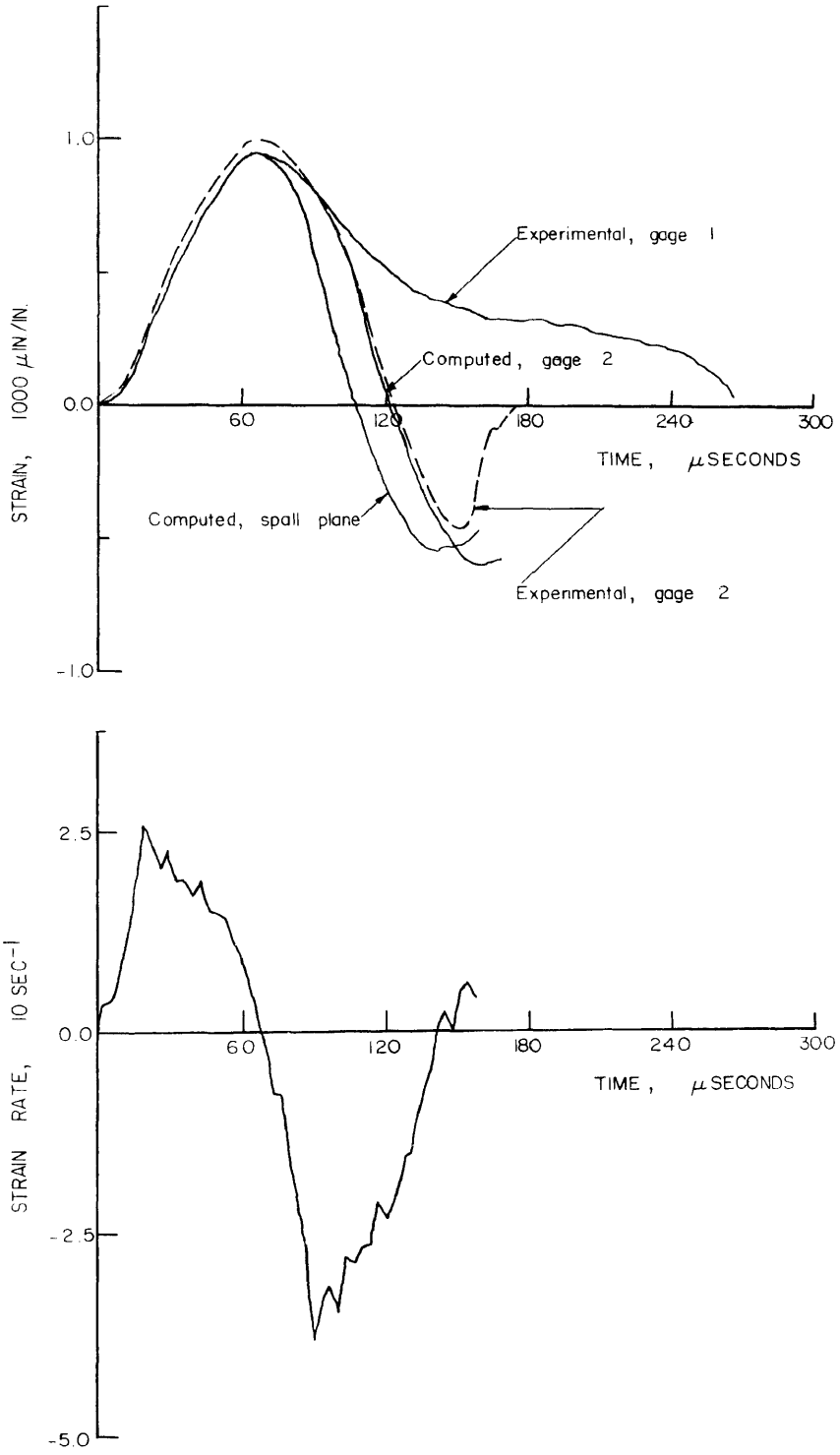

Figure B.9 (a) - Comparison of experimental and theoretical strains for specimen CC-L-3 (compression positive)
(b) - Strain rate history at spall plane for specimen CC-L-3

APPENDIX C

DERIVATIONS FOR CONVENTIONAL SPLIT HOPKINSON BAR ANALYSIS

For one-dimensional plane elastic stress wave propagation in the loading and transmission bars in the split Hopkinson bar test assembly, the following relation must be satisified, Kolsky (1963, p. 43):

$$\sigma = \rho c v \tag{C.1}$$

If one neglects the one-dimensional stress reflections in the specimen (that is, wave propagation and interaction, and radial and longitudinal inertia effects), the average stress in the specimen, σ_{avg}, can be defined as:

$$\sigma_{avg} = \frac{1}{2} (\sigma_{\text{specimen I}} + \sigma_{\text{specimen II}}) \tag{C.2}$$

where

$\sigma_{\text{specimen I}}$ = compressive stress in the specimen at Interface I.

$\sigma_{\text{specimen II}}$ = compressive stress in the specimen at Interface II.

The stress applied in the loading bar at Interface I, $\sigma_{\text{bar I}}$, is given by

$$\sigma_{\text{bar I}} = \sigma_I + \sigma_R \tag{C.3}$$

where compression is designated as positive and tension as negative. The stress introduced into the transmission bar across Interface II, $\sigma_{\text{bar II}}$, is given by

$$\sigma_{\text{bar II}} = \sigma_T \tag{C.4}$$

The stress in the specimen at Interface I, $\sigma_{\text{specimen I}}$, is given by

$$\sigma_{\text{specimen I}} = \sigma_T' \tag{C.5}$$

The stress in the specimen at Interface II, $\sigma_{\text{specimen II}}$, is given by

$$\sigma_{\text{specimen II}} = \sigma_T' + \sigma_R' \tag{C.6}$$

The boundary condition of equal forces on opposite sides of the interface and Equations (C.3) and (C.4) leads to the following expressions for $\sigma_{\text{specimen I}}$ and $\sigma_{\text{specimen II}}$

$$\sigma_{\text{specimen I}} = \frac{(\sigma_I+\sigma_R)A_I}{A_s} \tag{C.7}$$

$$\sigma_{\text{specimen II}} = \frac{\sigma_T A_T}{A_s} \tag{C.8}$$

The average stress in the specimen from Equation (C.2) is then given by

$$\sigma_{avg} = \frac{1}{2}\left[(\sigma_I+\sigma_R)\frac{A_I}{A_s} + \sigma_T \frac{A_T}{A_s}\right] \tag{C.9}$$

or in terms of strains,

$$\sigma_{avg} = \frac{1}{2}\left[(\varepsilon_I+\varepsilon_R)\frac{E_I A_I}{A_s} + \varepsilon_T \frac{E_T A_T}{A_s}\right] \tag{C.9a}$$

For the above Equations (C.3), (C.4), (C.5), (C.6), (C.7), (C.8), and (C.9), all the stresses (or strains) are to be measured at the same instant of time at the Interfaces I and II. In reality the stresses, σ_I, σ_R, and σ_T (or strains ε_I, ε_R, and ε_T) are measured at the strain gage stations locates some distance from these interfaces. A shift of the reflected and transmitted pulses along the time axis is therefore necessary in the calculation of the average stress in the specimen. The reflected and transmitted signals may be made time coincident by placing the gages on the loading and transmission bars equidistant from the specimen ($d_L = d_T$).

Since particle velocities are assumed to be continuous across Interfaces I and II, Equation (C.1) can be used to obtain

$$\dot{X}_I = \frac{\sigma_I}{\rho_I c_I} + \frac{-\sigma_R}{\rho_I c_I} \tag{C.10}$$

$$\dot{X}_{II} = \frac{\sigma_T}{\rho_T c_T} \tag{C.11}$$

where

$\dot{X}_I$= particle velocity at Interface I.

$\dot{X}_{II}$= particle velocity at Interface II.

Equation (C.10) shows that the net particle velocity of Interface I is made up of contributions from both the incident and reflected stress waves.

The average strain rate, $\dot{\varepsilon}_{avg}$, over the specimen length is given by

$$\dot{\varepsilon}_{avg} = \left(\frac{d\varepsilon}{dt}\right)_{avg} = \frac{\dot{X}_I - \dot{X}_{II}}{L_s} \tag{C.12}$$

Substituting Equations (C.10) and (C.11) into Equation (C.12) gives

$$\dot{\varepsilon}_{avg} = \frac{1}{L_s}\left(\frac{\sigma_I - \sigma_R}{\rho_I c_I} - \frac{\sigma_T}{\rho_T c_T}\right) \tag{C.13}$$

or in terms of strains,

$$\dot{\varepsilon}_{avg} = \frac{1}{L_s}\left[c_I(\varepsilon_I - \varepsilon_R) - c_T\varepsilon_T\right] \tag{C.13a}$$

The average strain in the specimen ε_{avg} at any instant t is given in terms of strain by

$$\varepsilon_{avg} = \int_0^t \dot{\varepsilon}_{avg}\, dt = \frac{1}{L_s}\int_0^t \left[c_I(\varepsilon_I - \varepsilon_R) - c_T\varepsilon_T\right]dt \tag{C.14}$$

Therefore, the average specimen stress, strain, and strain rate histories are given by the Equations (C.9), (C.14), and (C.13). It should be noted that multiple wave reflections within the specimen are not considered in the above analysis which is sometimes referred to as Kolsky's thin wafer technique. As it was pointed out before, the incident, reflected, and transmitted strain pulses must have the same

time origin for the computation so that time shifts must be performed in processing the experimental data.

If the incident strain gage is located sufficiently far from Interface I, as in the thesis investigation, σ_I and σ_R will not overlap each other in time and can be recorded separately. The zero time corresponds to the zero stress (or strain) point for both σ_I and σ_R pulses. The dynamic stress-strain-strain rate curve is found by plotting stress versus strain at correponding times.

The specimen introduces an additional time delay, τ, in the transmitted pulse because of the different arrival times at the two interfaces. This delay time is given by,

$$\tau = \frac{L_s}{c_s} \tag{C.15}$$

where

c_s = the propagation velocity in the specimen.

The proper representation of the pulses for the standard analysis is given in Figure 3.3, where the transmitted pulse has been shifted in the positive time direction by the amount τ.

APPENDIX D

SPLIT HOPKINSON BAR DATA FOR CONCRETE

Input and Output Curves

For the Conventional Analysis

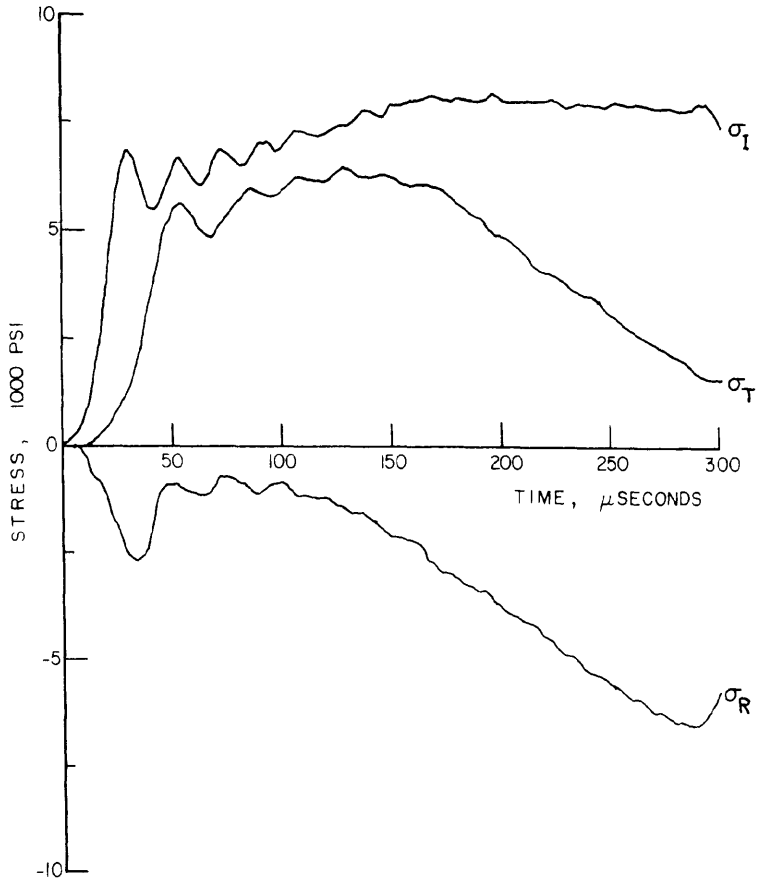

Figure D.1 - Incident, reflected, and transmitted stress pulses for specimen H-1-3

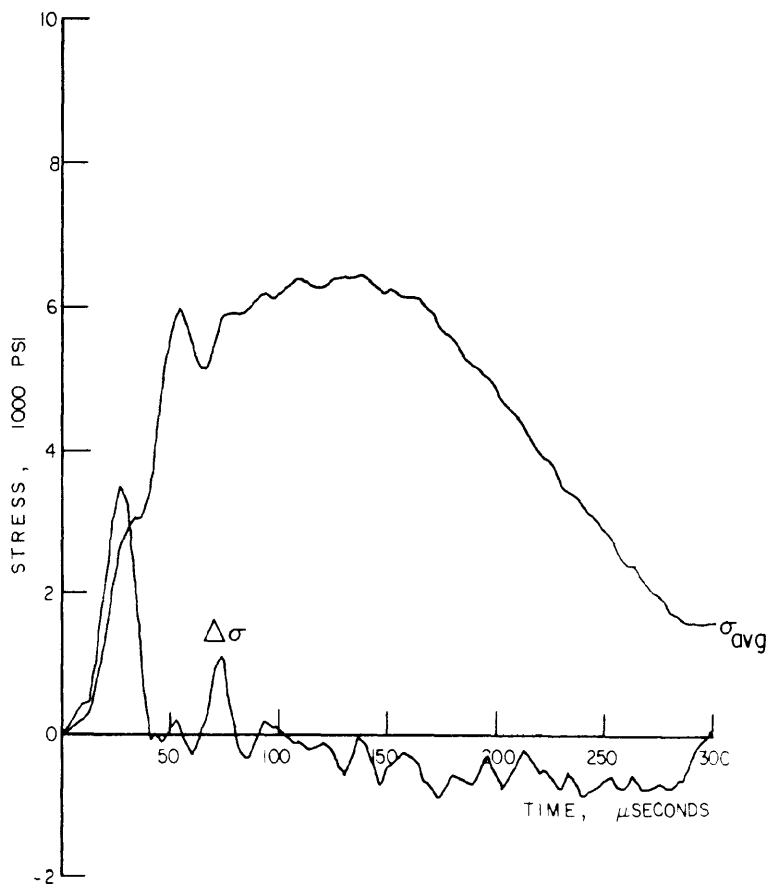

Figure D.2 - Average Stress and stress difference vs. time for specimen H-1-3

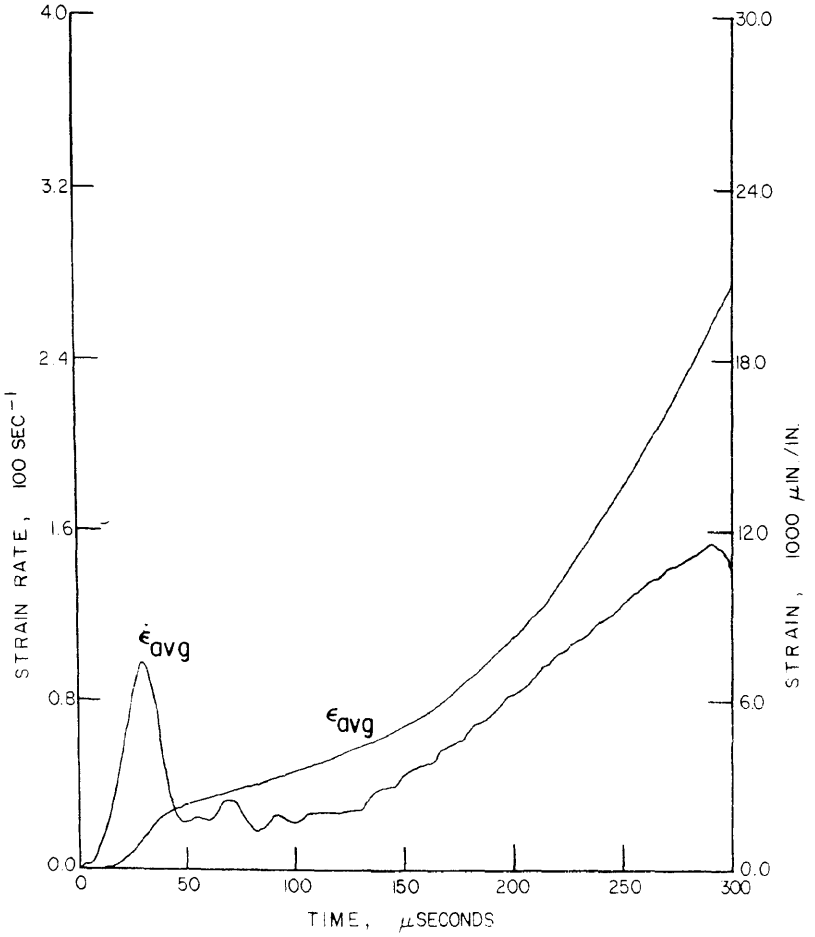

Figure D.3 - Average strain and strain rate vs. time for specimen H-1-3

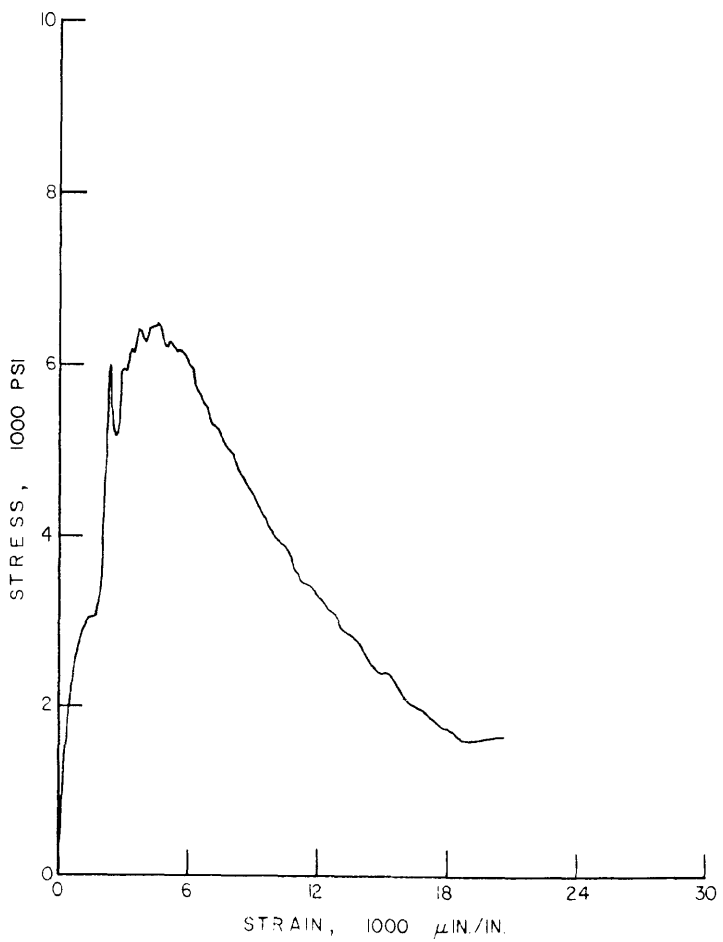

Figure D.4 - Average stress vs. average strain for specimen H-1-3

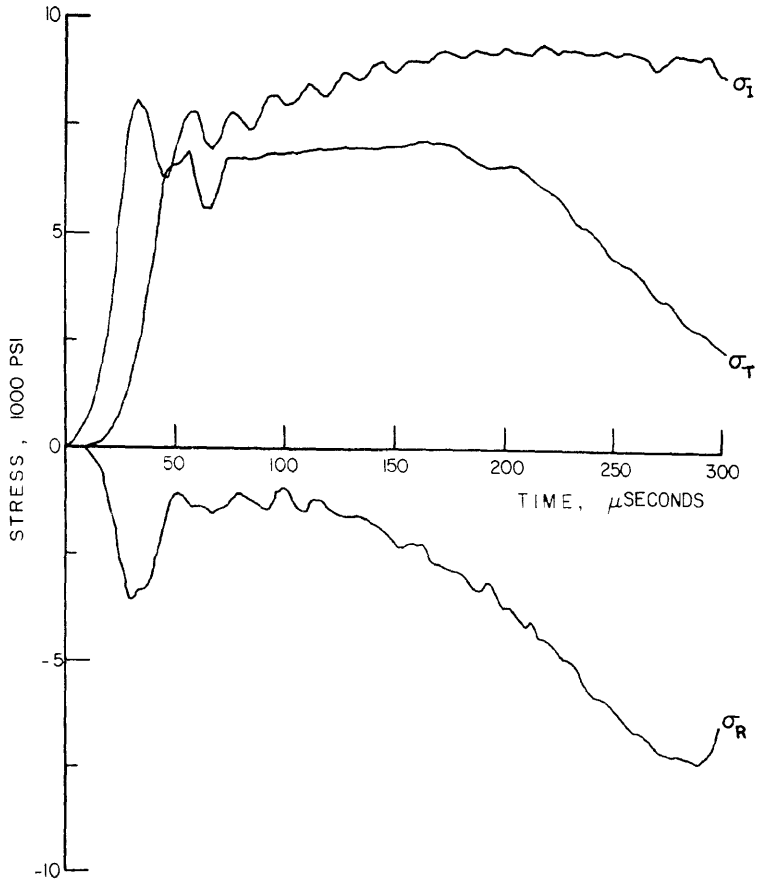

Figure D.5 - Incident, reflected, and transmitted stress pulses for specimen J-1

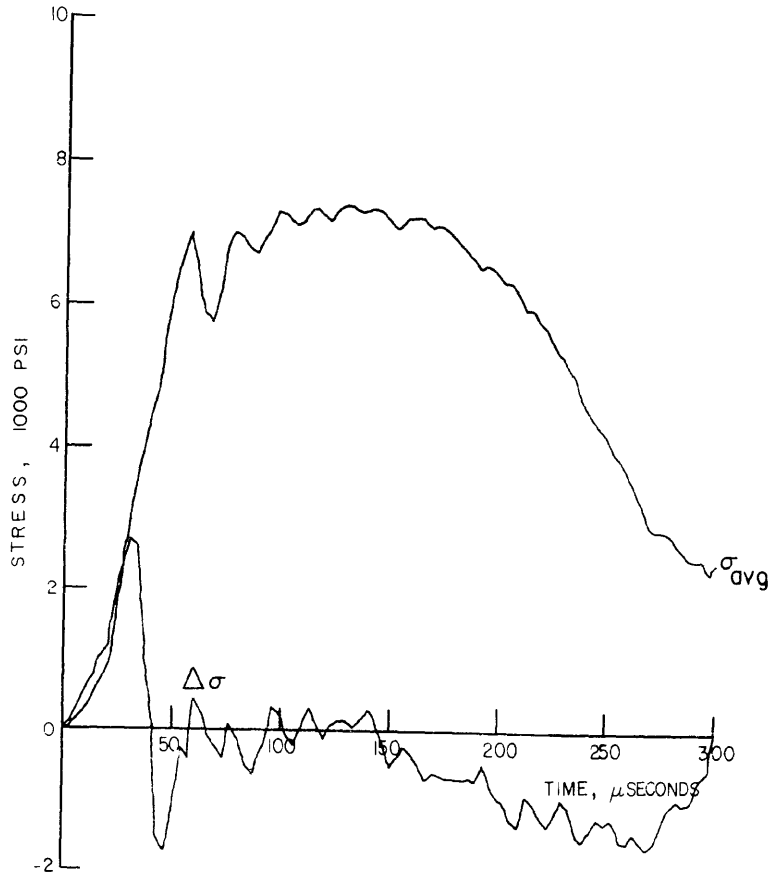

Figure D.6 - Average stress and stress difference vs. time for specimen J-1

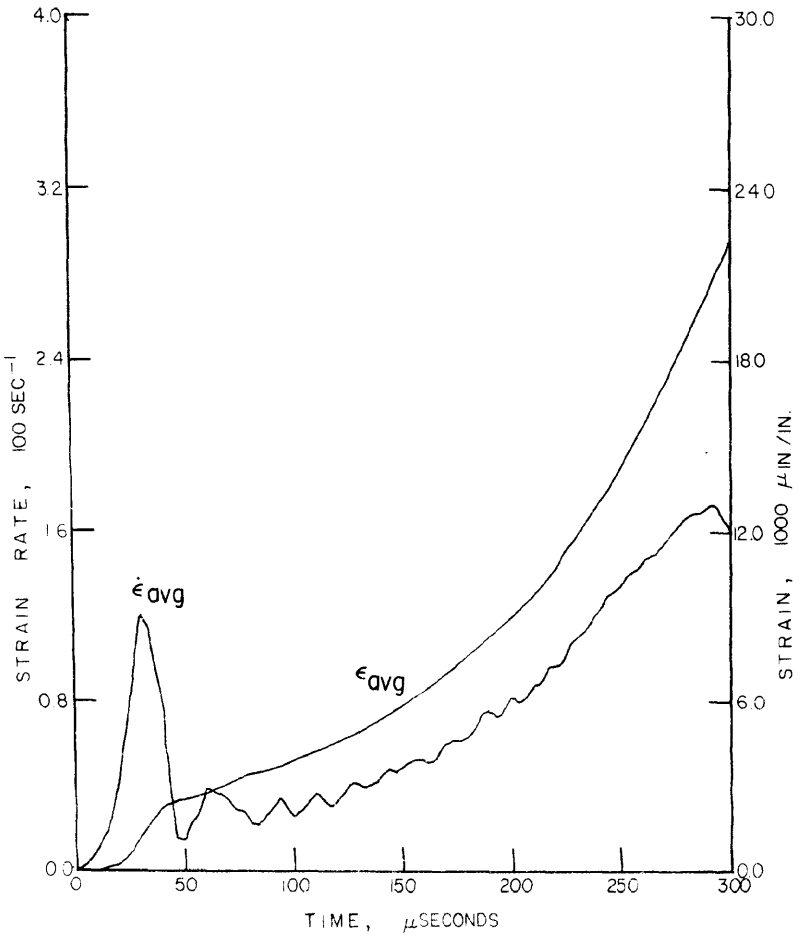

Figure D.7 - Average strain and strain rate vs. time for specimen J-1

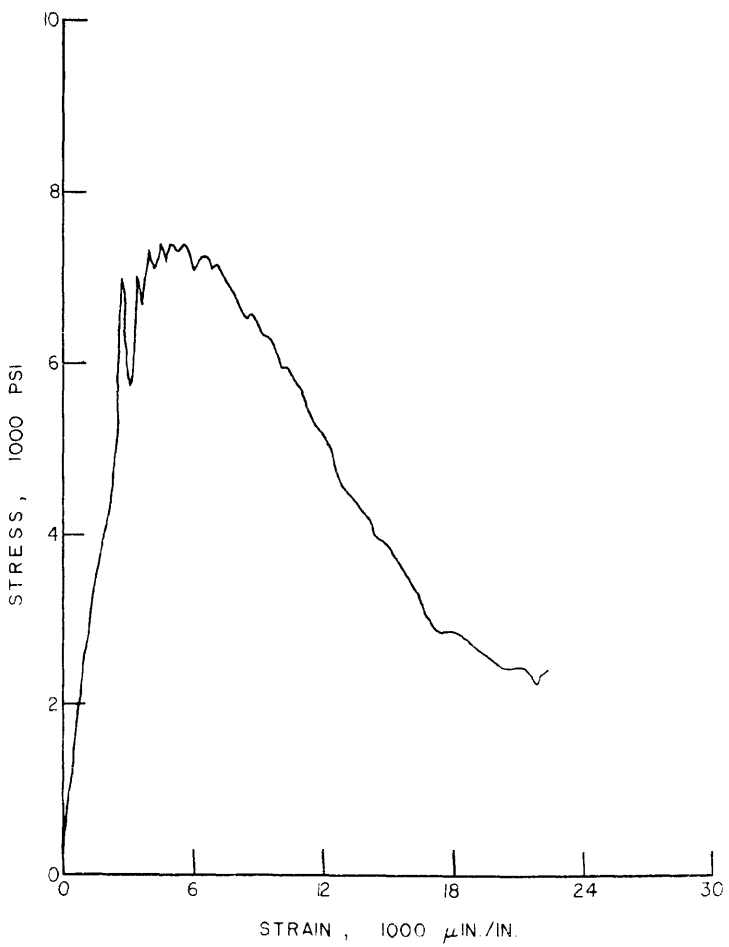

Figure D.8 - Average stress vs. average strain for specimen J-1

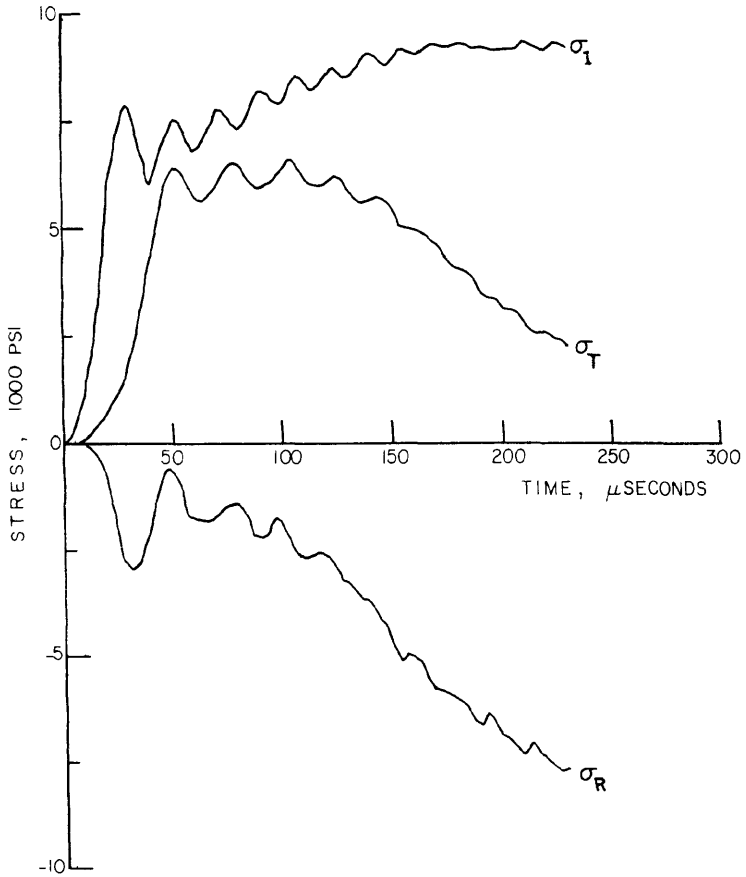

Figure D.9 - Incident, reflected, and transmitted stress pulses for specimen J-1-3

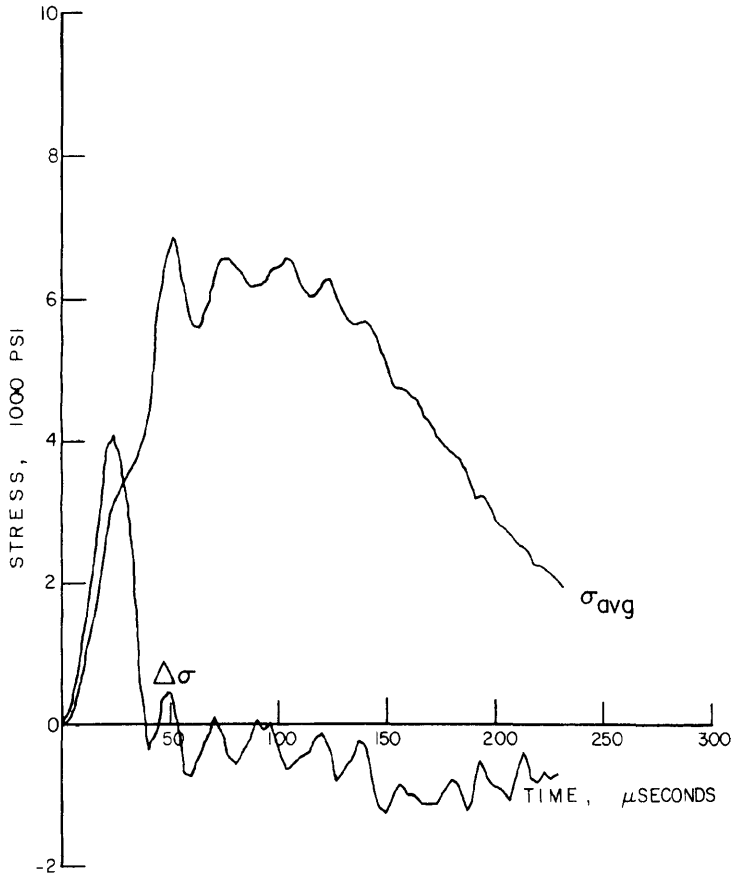

Figure D.10 - Average stress and stress difference vs. time for specimen J-1-3

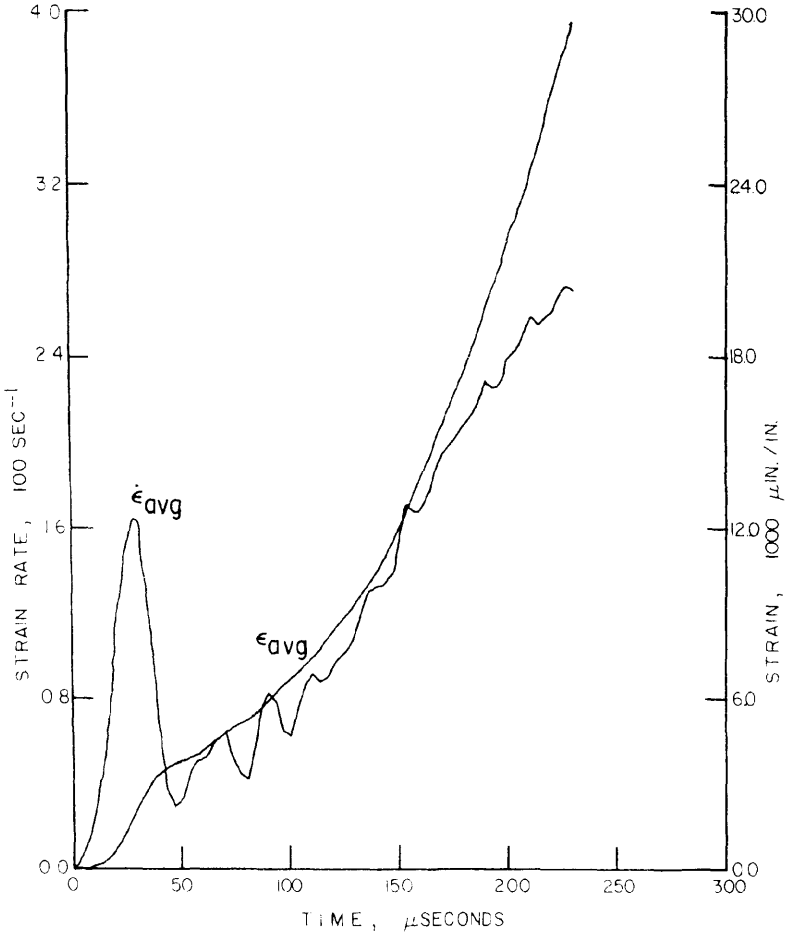

Figure D.11 - Average strain and strain rate vs. time for specimen J-1-3

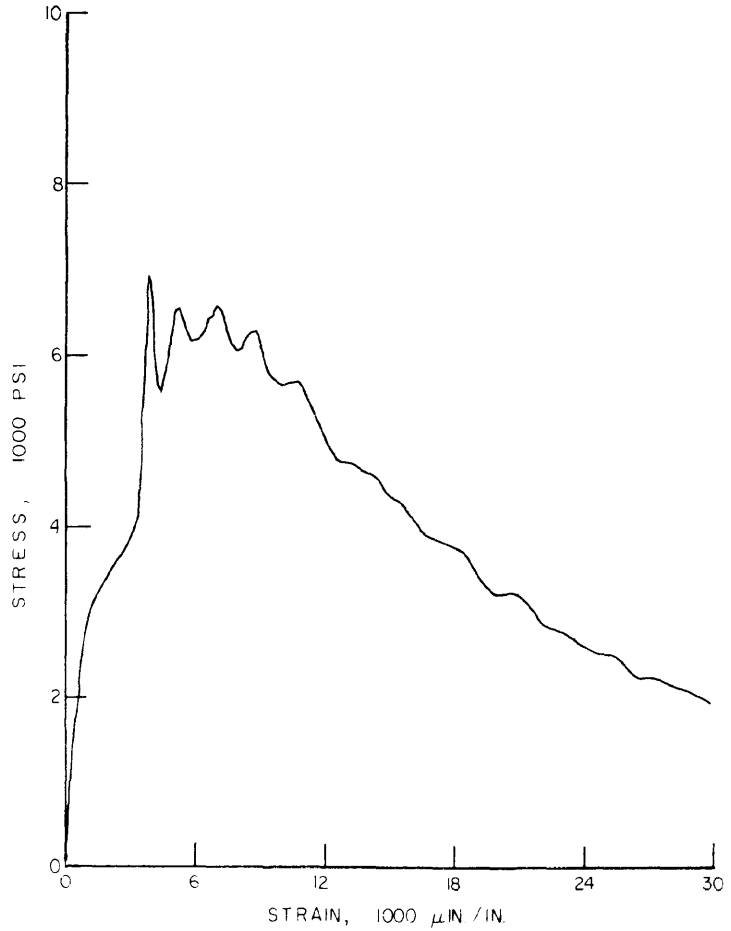

Figure D.12 - Average stress vs. average strain for specimen J-1-3

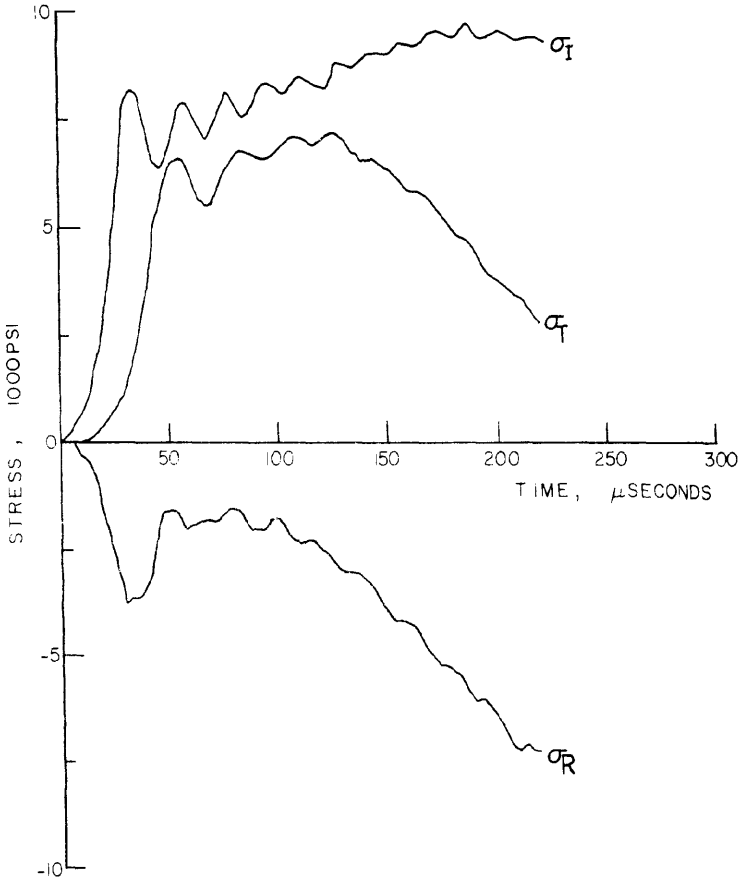

Figure D.13 - Incident, reflected, and transmitted stress pulses for specimen J-1-2

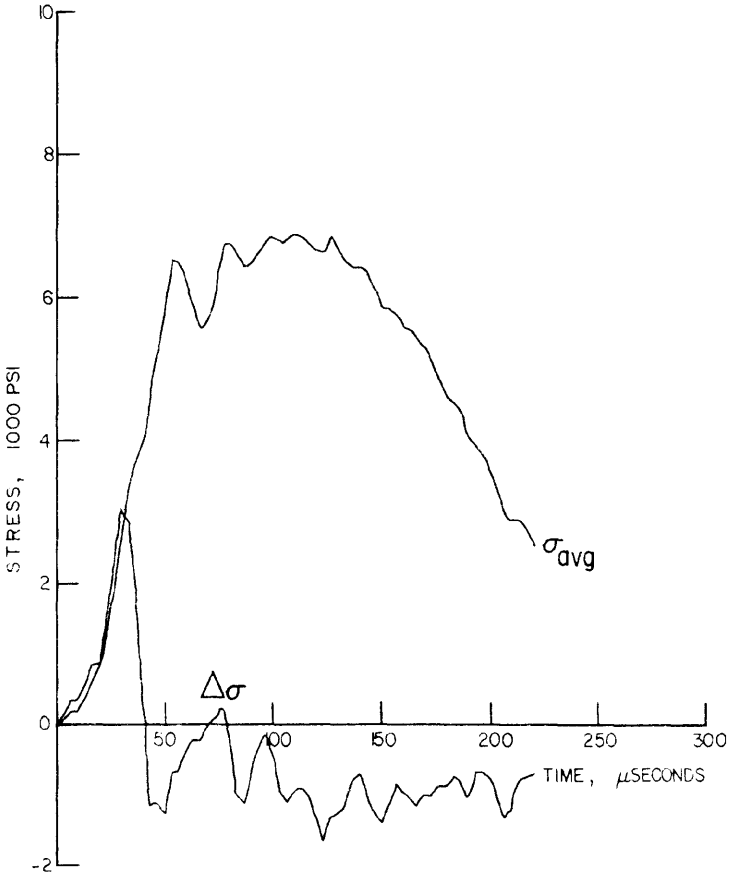

Figure D.14 - Average stress and stress difference vs. time for specimen J-1-2

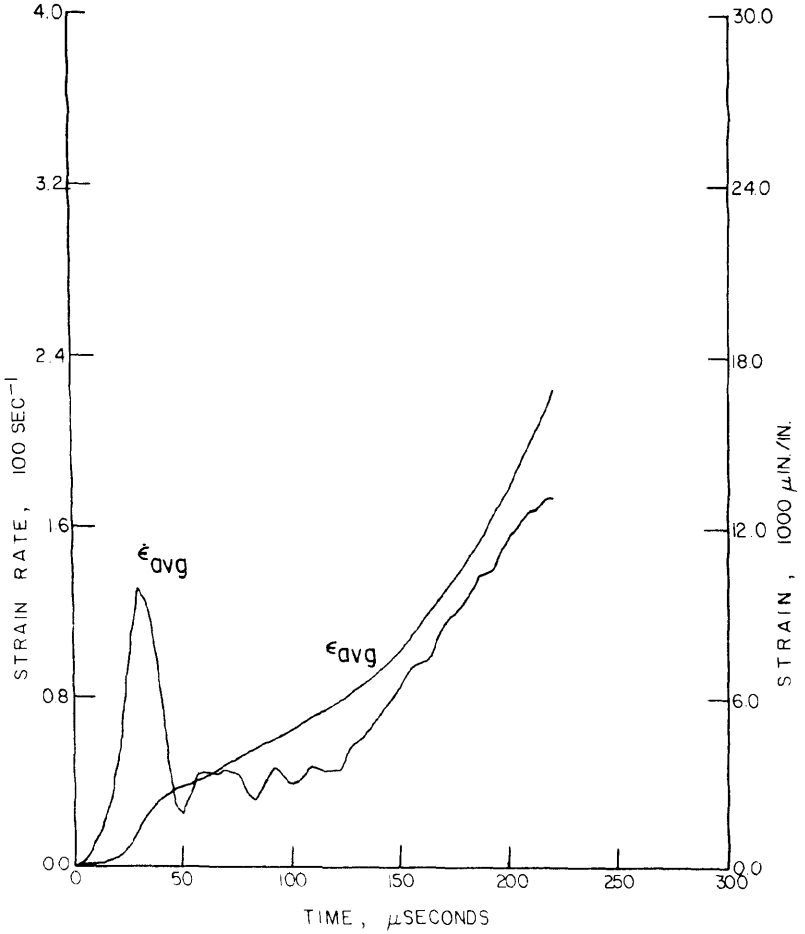

Figure D.15 - Average strain and strain rate vs. time for specimen J-1-2

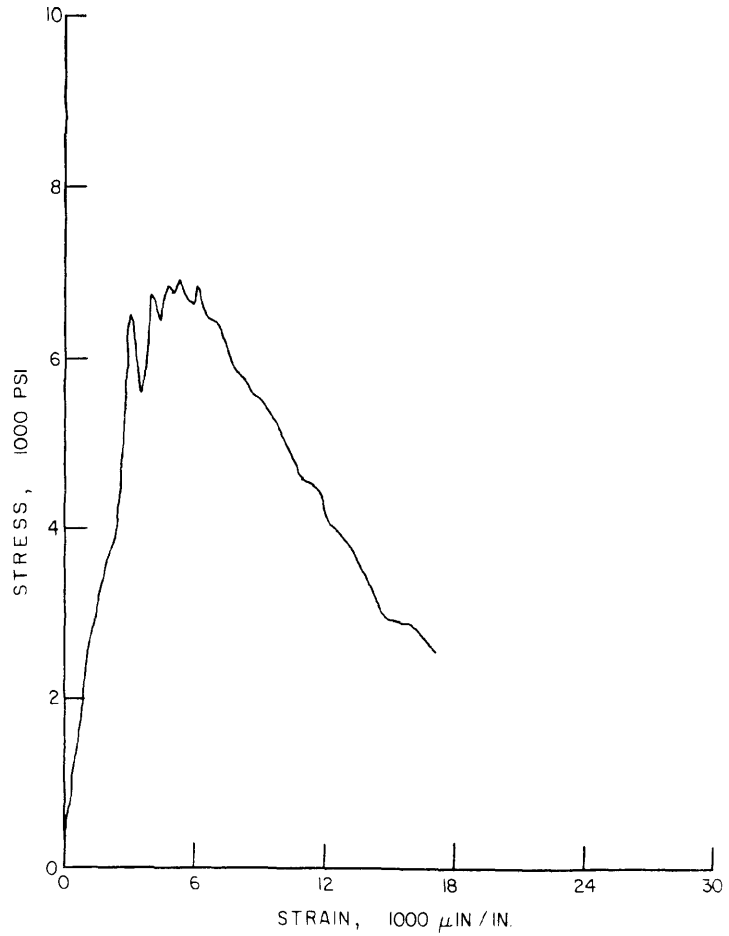

Figure D.16 - Average stress vs. average strain for specimen J-1-2